UNIVERSITÀ
DEGLI STUDI
DI BRESCIA

DOTTORATO DI RICERCA IN INGEGNERIA CIVILE, AMBIENTALE, DELLA COOPERAZIONE INTERNAZIONALE E DI MATEMATICA

XXXV CICLO
ICAR/02

Climate change impact on the cryosphere: from local to global scale

Paolo Colosio

Supervisor: Prof. Roberto Ranzi
Co-Supervisor: Prof. Marco Tedesco

Brescia, Maggio 2023

Dottorato di Ricerca in Ingegneria Civile e Ambientale della Cooperazione Internazionale e di Matematica (DICACIM)
XXXV ciclo
Curriculum: Analisi e gestione dei rischi naturali

Author: Paolo Colosio
Department Civil, Environmental, Architectural Engineering and Mathematics (DICATAM)
University of Brescia
Via Branze, 43 25123 Brescia BS
paolo.colosio@unibs.it

Supervisor: Professor Roberto Ranzi, Ph.D.
University of Brescia

Co-supervisor: Professor Marco Tedesco, Ph.D.
Lamont-Doherty Earth Observatory, Columbia University

Referees: Professor Attilio Castellarin, Ph.D.
University of Bologna

Professor Xavier Fettweis, Ph.D.
University of Liège

Board of Examiners: Main Members
Professor Stefano Ferraris, Ph.D.
Politecnico and University of Torino

Professor Giovanna Grossi, Ph.D.
University of Brescia

Professor Valter Maggi, Ph.D.
University of Milano Bicocca

Substitute Member
Professor Maria Cristina Rulli, Ph.D.
Politecnico di Milano

Submitted to the Referees on 17 March, 2023
Submitted to the Board of Examiners on 4 May, 2023
Printed on 10 May, 2023
Defense date 16 May, 2023

Abstract

The cryosphere, the region of the Earth where water is stored in its solid form, plays a crucial role in regulating Earth's energy balance and contributes to moisture fluxes and freshwater storage and release, providing water resources to many regions of the world. The cryosphere affects and is affected by climate conditions, being a driver and a sentinel of climate change, and playing a role of paramount importance from global to local scale processes. Here, different topics related to the cryosphere are investigated, spanning from the Greenland ice sheet to the Italian alps. A climatology of snow depth and snow water equivalent is carried out using a dataset of snow depth and snow density measurements collected at 299 sites between 1967 and 2020 over a wide portion of the Italian Alps. By performing different statistical analyses, a decrease of 12 cm every decade in snow depth and 37 mm every decade in SWE has been found since 1967. Average snow depth in the period 1994-2020 has been 33% lower than in the period 1967-1993, with stronger effects at low altitudes (reduction of 63% below 1500 m asl).The average SWE in 1994-2020 has been 36% lower than in 1967-1993. These results are confirmed by the increased elevation of the computed null snow depth elevation and the detected change-points at the end of the 1980s. The analysis of the HISTALP dataset confirmed the strong dependency of snow accumulation and melt on air temperature, impacting liquid/solid precipitation separation and timing of melt onset. The influence of snow on ground at local scale has been investigated evaluating the contribution of snowmelt to intense rain-on-snow events in Lombardy. By means of measured temperature, precipitation and snow depth data and the calibration of a snowmelt model, the timeseries of the combination of precipitation and melt has been obtained for the fixed durations 1, 3, 6, 12 and 24 h. The annual maxima analysis revealed that snowmelt increases the quantiles obtained from the selected extreme values distributions of about 2.2%, with stronger impacts for longer durations, up to 10%. At a larger scale, the analysis of surface melting over the Greenland ice sheet is of paramount importance to better estimate the ice sheet contribution to sea level rise. The cross-calibration of five different sensors collecting satellite data over the Greenland ice sheet between 1979 and 2019 has been performed. The comparison with in-situ observation and the output of the regional climate model MAR revealed that a threshold-based melt detection algorithm based on the electromagnetic emission model MEMLS shows the best performances in capturing surface melting evolution. The long-term trends analysis showed an increase of surface melting areal extension of about 3.6-6.9% of the Greenland ice sheet every decade. The melting season has started between 3 and 4 days earlier and between 3 and 7 days later every decade. The total number of melting days has increase by 3-5 days every decade. A statistical downscaling algorithm for the regional climate model MAR has been implemented. The comparison with in-situ observations and satellite measurements

revealed that the downscaled dataset can well capture temperature temporal evolution and spatial distribution. It better captures at local scale the cumulated surface mass balance, exhibiting lower errors when compared with measured surface mass balance with respect to the original modelled output.

Sommario

La criosfera, la porzione della superficie terrestre dove l'acqua è immagazzinata allo stato solido, svolge un ruolo di fondamentale importanza nella regolazione del bilancio energetico terrestre e del ciclo idrologico, fornendo risorse idriche a molte regioni del pianeta. La criosfera, regolando ed allo stesso tempo essendo influenzata dalle condizioni climatiche, è una importante sentinella dei cambiamenti climatici, subendone gli effetti e scaturendone ulteriori a scala globale e locale. In questo studio vengono analizzate diverse tematiche legate alla criosfera, dalle Alpi italiane alla Groenlandia. Viene studiata in primo luogo la climatologia di altezza ed equivalente in acqua del manto nevoso (SWE) tramite l'analisi statistica di altezza e densità della neve raccolte tra il 1967 ed il 2020 in un'ampia regione delle Alpi italiane. Dall'analisi statistica è emerso che l'altezza neve è diminuita di 12 cm e lo SWE di 37 mm per decade dal 1967. L'altezza media della neve si è ridotta del 33% nel periodo 1994-2020 rispetto al periodo 1967-1993, mentre lo SWE del 37%. Gli effetti del cambiamento climatico risultano essere più intensi a basse altitudini, con una riduzione dell'altezza del manto nevoso del 63% al di sotto dei 1500 m. Questi risultati sono ulteriormente confermati dal change-point trovato a fine anni 1980. L'analisi del dataset HISTALP mostra la forte dipendenza dell'evoluzione del manto nevoso dalla temperatura, influenzando lo stato di precipitazione e regolando l'inizio della fusione. Gli effetti del manto nevoso a scala locale sono stati studiati analizzando il contributo della fusione nivale nel caso di eventi di precipitazione intensa con presenza di neve al suolo. L'analisi è stata limitata alle stazioni di Aprica e Pantano d'Avio, in Lombardia, dove sono stati raccolti i dati di temperatura, precipitazione ed altezza neve dal 1996. Con i dati osservati è stato calibrato un modello gradi-giorno tramite il quale è stato possibile ricostruire la serie temporale della somma di precipitazione e fusione nivale per le durate di 1, 3, 6, 12 e 24 ore. L'analisi degli annual maxima ha mostrato che la fusione nivale contribuisce ad un incremento medio dei quantili di circa il 2.2%, aumentando con la durata fino a raggiungere, in un solo caso, il 10%. Ad una più larga scala, lo studio della fusione superficiale della Groenlandia è di fondamentale importanza nella stima del contributo della calotta di ghiaccio all'innalzamento del livello medio degli oceani. Sono stati raccolti ed intercalibrati i dati satellitari a microonde passive raccolti da sensori montati su cinque diversi satelliti tra il 1979 ed il 2019. Il confronto con dati misurati da stazioni meteorologiche e con simulazioni del modello climatico regionale MAR hanno mostrato che un algoritmo basato sul modello di emissione elettromagnetica MEMLS riesce a cogliere l'evoluzione spaziale e temporale della fusione superficiale. L'analisi dei trend di lungo periodo ha mostrato che la superficie di fusione è aumentata tra il 3.6 ed il 6.9% dell'intera area della Groenlandia per decennio durante il periodo di osservazione. Inoltre, la stagione di fusione è iniziata tra i 3 ed i 4 giorni prima e si è conclusa tra i 3 ed i 7 giorni dopo ogni decennio.

Il numero totale medio di giorni di fusione è aumentato di circa 3-5 giorni per decennio. Per l'area della Groenlandia è stato poi implementato un algoritmo di downscaling statistico per il modello MAR. Il confronto con le misure di temperatura delle stazioni meteorologiche e con i dati di temperatura superficiale rilevati dal satellite Lansat-8 mostra come il dataset ad elevata risoluzione riesca meglio a cogliere la distribuzione spaziale della temperatura, senza perdere accuratezza a livello locale. Il confronto con le misure di bilancio di massa superficiale mostra invece un sostanziale miglioramento rispetto all'output originale a bassa risoluzione.

Ringraziamenti

Gli ultimi tre anni sono stati ricchi di avventure. Partendo dall'esperienza dei mesi trascorsi a New York, interrotta dall'emergenza pandemica, passando attraverso le settimane regolate da coprifuoco e quarantene, fino ai più liberi mesi dell'ultimo anno e mezzo, il mio percorso ha incrociato quello di molti colleghi ed amici. Desidero quindi ringraziare le persone che mi hanno accompagnato nel corso di questi ultimi anni di studio, contribuendo, più o meno direttamente o consapevolmente, alla realizzazione di questa tesi.

Un sentito grazie è dovuto al Professor Roberto Ranzi per il sostegno fornitomi nei tre anni passati e per i suoi buoni consigli. Lo ringrazio per avermi dato la preziosa possibità di studiare ed approfondire molteplici tematiche, non limitate ai contenuti di questa tesi, permettendomi di crescere attraverso un percorso culturale e scientifico di ampia visione.

Voglio ringraziare il Professor Marco Tedesco per avermi accolto nuovamente alla Columbia University e per il costante confronto negli anni di dottorato. Ricordo come se fossero passati solo pochi giorni quando, lungo il tragitto di ritorno sulla West Side Highway o durante una corsa a Central Park, discutevamo del mio interesse a proseguire gli studi. Senza i suoi stimoli ed incoraggiamenti, sempre colmi di fiducia ed amicizia, questo percorso non avrebbe probabilmente avuto inizio.

Ringrazio la Professoressa Giovanna Grossi per il sostegno ed il coinvolgimento, soprattutto nei primi mesi. Anche grazie a lei ho potuto intraprendere questo percorso. Esprimo la mia gratitudine al Professor Guido Cervone della Penn State University che ha fornito la sua enorme esperienza nella programmazione ed analisi di dati geospaziali per concludere il lavoro relativo al downscaling del modello climatico regionale MAR. Il Professor Xavier Fettweis dell'Università di Liegi ha reso disponibili, oltre alle simulazioni del modello, le sue accurate ed approfondite revisioni, in particolare ai capitoli relativi alla Groenlandia. All'Ingegnere Giorgio Galeati va un caro ringraziamento per l'aiuto nello studio statistico della neve alpina tramite consigli pragmatici ed oltremodo precisi. Un grazie al Professor Stefano Barontini, per il continuo dialogo culturalmente arricchente ed i mai banali spunti di riflessione, ed al Professor Massimo Tomirotti, che mi ha insegnato, lavorando alla ricostruzione di serie storiche, che per i dati è necessaria cura ed attenzione.

Desidero poi ringraziare i miei compagni di scrivania e di viaggio - Patrick e Raf ed i miei amici Lorenzo e Francesco per i primi mesi a New York, Stella, Francesca, Tewelde, Andrea, Flavio, Maria e Federico ed i colleghi Marco, Arianna, Riccardo, Gabriele, Usman e Babak negli anni a Brescia - con cui ho condiviso fatiche e dubbi ma anche soddisfazioni e tanti momenti di divertimento. Un sincero grazie a tutti i miei amici, insostituibili compagni di avventure. La mia vita è piena di gioia anche grazie a tutti voi.

Devo la mia più profonda gratitudine a Sandra, Beppe, Andrea ed Alberto per aver sempre sostenuto e condiviso le mie scelte in questi anni di studio con tutto l'amore che si possa desiderare e per aver sempre creduto in me. I miei traguardi sono anche i vostri. Un grazie anche a tutti i miei familiari, con un pensiero particolare ai miei nonni - Lina, Berto e Cesara - per avermi sempre fatto sentire il vostro orgoglio. Infine grazie a Roberta, sempre al mio fianco negli ultimi dieci anni, che con pazienza ed insostituibile supporto ha compreso le ragioni alla base della mia scelta di intraprendere questo percorso di studio, generate da una profonda e sincera curiosità, e mi ha sempre spinto a dare il meglio e a non mollare di fronte alle difficoltà.

Brescia, Maggio 2023
Paolo Colosio

Contents

List of Figures

List of Tables

Chapter 1

Introduction

In the beginning the Universe was created. This has made many people very angry and been widely regarded as a bad move.

D. Adams,
The Restaurant at the End of the Universe

The cryosphere is the region of the Earth where water is stored in its solid form, either annually or seasonally. Its components are snow, glaciers, ice sheets, ice shelves, ice caps, freshwater ice, sea ice, icebergs, permafrost, and ground ice. It plays a crucial role in regulating the Earth's climate system through different mechanisms, and it is interconnected with the atmosphere, the hydrosphere, and the biosphere. It regulates Earth's energy balance by reflecting some of the incoming solar radiation due to its high albedo and contributes to moisture fluxes and freshwater storage and release, providing water resources to many regions of the world. The cryosphere affects and is affected by climate conditions, being a driver and a sentinel of climate change, and playing a paramount importance role from global to local scale processes.
According to NOAA's 2021 Annual Climate Report the global temperature has increased on an average rate of 0.08°C every decade since 1880, with a significantly faster rate of 0.18°C per decade after 1981. Such rate is not spatially homogeneous around the globe, with stronger increase in polar regions. This phenomenon is called polar amplification and it is caused by a combination of feedback mechanisms (Serreze and Barry, 2011). As the surface air temperature increases, water vapor brought into the atmosphere through evaporation and transpiration processes increases, as well as the water vapor holding capacity of the atmosphere according to the Clausius-Clapeyron relation. Temperature increases can also affect clouds absorption properties, possibly amplifying or weakening temperature changes. Water vapor content and cloud cover can affect surface temperature due to their greenhouse effect (Bony et al., 2006). Moreover, as ice- and snow-covered areas retreat as a consequence of rising temperatures in the polar regions, larger dark surfaces previously covered by ice and snow are exposed. These darker areas can absorb a larger portion of the incoming solar radiation, leading to further increase in temperatures. Arctic sea ice extent has been dramatically decreasing since the end of the 1970s,

exposing a wider area of dark and energy absorbing ocean (Cavalieri and Parkinson, 2012). The albedo of the Greenland ice sheet has been decreasing in the past decades and is expected to decrease at a faster rate than the actual climate projections (Tedesco et al., 2016), further impacting Polar temperatures. This mechanism is called ice-albedo feedback, firstly theorized by Arrhenius (1896). These feedback mechanisms are expected to accelerate the effects of the warming climate at the Poles, such as ice mass loss from the ice sheet, contributing to sea level rise. Between 2002 and 2016 the Greenland and Antarctica ice sheet have contributed to increase the average sea level of 0.8 mm and 0.4 mm every year and their contribution is expected to increase by the end of the century, threatening low-lying coastal communities and small island states. The changes in the cryosphere are having significant impacts on ecosystems and biodiversity. For example, the loss of sea ice in the Arctic is causing habitat loss for species such as polar bears and seals, while the melting of glaciers and ice sheets is leading to changes in the distribution and abundance of freshwater species (IPCC, 2019).

At lower latitudes, the cryosphere in of great importance in regulating the hydrological cycle. In the Alpine region it affects many aspects of human life (Beniston et al., 2018). The separation of solid and liquid precipitation, together with the timing of the melting season, affects the water resources at regional scale. In fact, snow accumulates at high altitudes in winter, being a natural freshwater reservoir. As the melting season begins, freshwater volumes are released as surface runoff and contributing to water availability for multiple purposes (e.g., agriculture and hydropower generation). Italy's hydropower generation corresponds to more than 40% of the national renewable energy production. Changes in timing of the available water volumes for energy production can affect the hydropower plants, potentially forcing managers in re-considering the current plant operation. The accumulation of snow in winter also guarantees water availability in summer. Consequently, a decreased snow accumulation would lead to drier summer months, as happened in 2022. The summer of 2022 has been the hottest and driest of the last 500 years in Italy, with an intense and long duration drought, causing costs of lost production close to 1 billion euros (agricultural lobby Coldiretti estimate). Snow in the alps can also regulate flood events timing and peak volume. If flood events can be mitigated and delayed by the snowpack capacity to retain rainfall, on the other hand snow can enhance flood intensity by providing additional water volume through snowmelt. Finally, snow is extremely important from a socio-economic prospective. Winter tourism in the Alps is dominated by snow related activities (mainly skiing), a business of about 10 billion euros that provides seasonal jobs and keeps the Alpine human activity, slowing down the ongoing depopulation. Monitoring changes in the cryosphere and understanding its impacts is critical for policymakers, scientists, and communities to make informed decisions for water respurces management, mitigation and adaptation measurements, and guide investments.

This research thesis is aimed to investigate different topics related to the cryosphere, spanning from the Greenland ice sheet to the Italian alps. Each chapter is an independent research paper covering a specific topic. In Chapter 2 and Chapter 3 the research is focused on regional (Chapter 2) and local (Chapter 3) scale aspects of the cryosphere. In Chapter 2, a climatology of snow depth and snow water equivalent is carried out using a dataset of snow depth and snow density measurements collected at 299 sites between 1967 and 2020 over a wide portion

of the Italian Alps. The analysis relies on a combination of classical statistical analyses and tests, aimed in identifying trends, change-points and correlations with climatic indexes and meteorological variables. In Chapter 3 the influence of snow on ground during rain-on-snow events is investigated. A snow water equivalent accumulation and melt model is implemented in order to estimate the contribution of snow melting in rainy days at two stations located in Lombardy. The contribution of snowmelt is estimated statistically in terms of increments of the indensity-duration-frequency curves computed using the annual maxima method taking in consideretion meltwater produced in rain-on-snow days together with precipitation. Chapter 4 and Chapter 5 focus on larger scale processes. In Chapter 4 a climatology of surface melting over the Greenland ice sheet has been carried out through the analysis of enhanced resolution passive microwave satellite observations. Data from five different sensors are cross-calibrated and combined to reconstruct a sufficiently long timeseries for climatological studies. Four different threshold-based melt detection algorithm are implemented, tested using in-situ observations and regional climate model outputs. The melting maps obtained are used to reconstruct the climatology of surface melting of the Greenland ice sheet in terms of temporal duration and spatial extension. In Chapter 3 a statistical downscaling algorithm is implemented over the Greenland ice sheet. The results are discussed through the comparison with in-situ measurements and remotely sensed data.

Chapter 2

Climatology of Snow Depth and Water Equivalent measurements in the Italian Alps (1967 - 2020)

Toutefois, ce vêtement de neige, ce blanc manteau dont parlent les poètes, est percé, déchiré en mille endroits.

É. Reclus,
Histoire d'une montagne

Under submission:

Ranzi, R., Colosio, P. and Galeati, G. (2023). Climatology of Snow Depth and Water Equivalent measurements in the Italian Alps (1967 - 2020). Hydrology and Earth System Sciences.

Abstract

A climatology of SWE based on data collected at 299 gauging sites was performed for the Italian Alps over the 1967 – 2020 period, when the Italian National Electric board conducted routinely and with homogeneous methods snow depth and density measurements. Six hydrological sub-regions were investigated spanning from the eastern Alps to the western Alps at altitudes ranging from 1000 m to 3000 m asl. Measures were conducted at fixed dates at the beginning of each month from 1 February to 1 June and on 15 April. To our knowledge this is the most comprehensive and homogeneous dataset of measured snow depth and density for the Italian Alps. Significant decreasing trends over the years at fixed dates and elevation classes were identified for both snow depth (-0.12 m decade^{-1} on average) and snow water equivalent (-37 mm decade^{-1} on average) in most of the six investigated areas. The analysis of snow density data showed a temporal evolution along the snow accumulation and melt season, but no altitudinal trends were found. A Moving Average and Running Trend Analysis (MARTA triangles),

combined with a Pettitt's test change-point detection, highlighted a decreasing change of snow climatology occurring around the end of the 1980s. Correlation with climatic indexes indicate significant negative values of Pearson correlation coefficient with winter North Atlantic Oscillation (NAO) index and positive values with winter West Mediterranean oscillation (WeMO) index for some areas and elevation classes. Results of this climatology are synthesized in a temporal polynomial model useful for climatological studies and water resources management in mountain areas.

2.1 Introduction

The effects of global climate on the cryosphere at different latitudes have been widely studied in the last decades (Pörtner et al., 2019). The comparison between photos of the past decades with the current ones, together with imagery analysis from satellites, confirms the retreat of glaciers in the Alpine region (Ranzi et al., 1999; Beniston, 2012). Analysis of long term observed snow depth and simulated snow density in 20 gauging sites in the Italian Alps highlights a decrease of snow water equivalent especially after the 1990s (Colombo et al., 2022). Modifications of the Greater Alpine Region climate have been confirmed by the analysis of the HISTALP dataset, with significant trends in temperature, twice as the global average, precipitation and relative humidity (Auer et al., 2007; Brunetti et al., 2009). In fact, the alpine region is an extremely sensitive area to the variations of climate condition, making mountain glaciers sentinels of climate change. Snow is the largest component of the cryosphere in terms of areal extension. Its importance in the Alpine region is related to climatological, hydrological, biological, economic, and social aspects (Beniston et al., 2018). Snow cover regulates the surface energy balance, affecting circulation patterns and atmospheric flow regimes (Ge and Gong, 2009). The hydrological cycle is strongly dependent on the separation between solid and liquid precipitation and the timing of the melting season onset, mainly driven by temperature. Moreover, snow accumulation and melting are a major component of the mass balance of glaciers. Snow monitoring is crucial in order to provide a proper estimate of glaciers mass and energy balance to evaluate glacial response to snow cover variations. The presence of snow is also of paramount importance for ski resorts and for winter tourism in general in the Alpine region, accounting for about 10 billion euro, maintaining seasonal jobs and slowing down the rural depopulation in the valleys (Lehr et al., 2012; Reynard, 2020).The water stored as snow in winter is released as the melting season begins, contributing to the water availability for agriculture and energy production in hydropower plants (HPP). Hence, it is of great interest for HPP managers having an accurate quantification of the snow water equivalent (SWE) and possible variability in a climate change scenario (Schaefli et al., 2007). In view of this, since 1966, ENEL (Italian National Electric Board) conducts systematic observations of snowpack depth and density in the basins subtended by seasonal regulation reservoirs. The ENEL measurement program is similar to other institutional measurement networks (e.g. SNOTEL; Serreze et al., 1999). Before the creation of ENEL, some power companies already took care of periodic measurements of the snowpack consistency on the Alpine and Apennines basins supplying reservoirs within their competence. However, these surveys were carried out unevenly, adopting different instruments and, of course,

with different procedures for processing and interpretating the collected dataset. The ENEL measurement campaigns are scheduled since the early 1960s at fixed dates from the 1st of February to the 1st of June at fixed locations in the catchments of the main Alpine reservoirs. Such extensive and standardized monitoring campaign represents a rich and valuable source of in situ measurements covering a wide portion of the Italian Alps for a 54-years time window spanning the 1967-2020 period. Hydrological models and remote sensing techniques have been widely used to estimate SWE (Taschner et al., 2004; Tedesco et al., 2015) and snow cover (Terzago et al., 2010). However, in situ measurements are required to validate such estimates and it is not trivial to reconstruct a coherent timeseries long enough to be suitable for climatological studies by means of satellite observations. Lejeune et al. (2019) used snow dataset of 57 years from a mountain meteorological station to evaluate snow depth variability between 1960 and 2017, a temporal range sufficiently wide to evaluate climate impacts on snow depth. A similar dataset has been used by López-Moreno (2020) to evaluate long-term trends of snow depth and snow cover in the Pyrenees. Schöner et al. (2019) used an ensemble of 196 stations to study the snow depth and its linkages to climate change over the Swiss-Austrian Alps over the monitoring period 1961-2012. A more comprehensive study of the Northern Hemisphere has been carried out by Pulliainen et al. (2019) using the GlobSnow v3.0 dataset (Takala et al., 2011) for the monitoring period 1980-2018. Valt and Cianfarra (2010) found a reduction of snow cover duration and snowfall between 1950 and 2009, together with breakpoints of the timeseries at the end of the 1980s. Marty et al. (2017) observed a SWE decrease, more pronounced in spring than in winter, over the observation period 1968-2012. Colombo et al. (2022) modelled the SWE from 19 historical snow depth measurements and studied the links of the Standardized SWE Index with teleconnection indexes and temperature anomalies. Marcolini et al. (2017) analysed snow depth series in the Adige basin, finding a reduction of snow cover duration and snow depth over the period 1980-2009, especially at low elevation sites. The dataset we use here covers almost the same period of previous studies, but it is spatially distributed over the Italian Alpine Region and includes snow density measurements to estimate SWE. Such combination of spatial and temporal coverage makes this dataset an extremely precious support to understand snow variability and climate change impacts in the Italian Alps. In this study, we present a detailed long-term trends and variability analysis of snow depth and SWE measurements in a wide portion of the Italian Alps between 1967 and 2020. In Section 4.2, after a description of the study area and the snow depth and density measurement procedure, we present the datasets adopted and describe the statistical methodology used for the climatological analysis. We also present a simple model to estimate the SWE as function of elevation and day of the year based on polynomial regressions of the observed snow depth and snow density. In Section 3.3 we present and discuss the results obtained for snow depth and snow density comparing them with the analysis of meteorological variables and climatic teleconnection indexes.

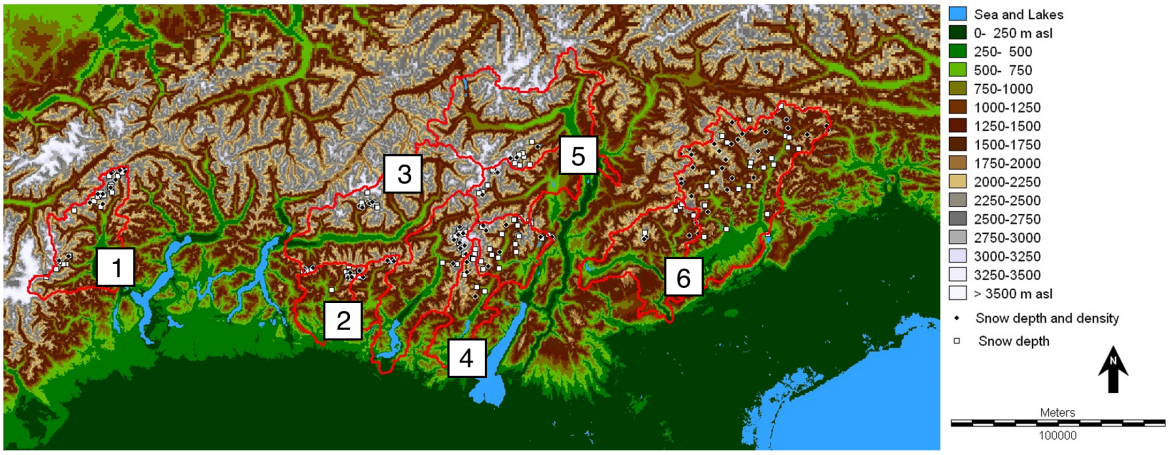

Figure 2.1: Map of the research area. The individual basins are grouped in the six macro basins by number: (1) Toce, (2) Serio-Brembo, (3) Adda, (4) Oglio-Chiese-Sarca, (5) Adige and (6) Piave-Brenta. Locations of snow depth and density (black dots) and snow depth (white squares) are also reported.

2.2 Datasets and Methods

2.2.1 The study area and basins aggregation

In this study we focus our analysis on the following basins of the Alpine Region: Cordevole and Piave, in the Veneto Region, Cismon, Brenta, Noce, Sarca, Chiese, Valsura, in the Trentino-Alto Adige Region, Mallero, Adda, Bitto, Serio, Brembo, Oglio, in the Lombardia Region and Toce in the Piemonte Region. We aggregate the individual basins in six groups (Figure 2.1) according to the hydrographic criteria, merging tributaries to the main river branch (e.g. Cordevole aggregated to Piave), and the geomorphoclimatic criteria, aggregating basins with similar annual average precipitation, temperature and geographical orientation (e.g. Piave and Brenta or Oglio, Chiese and Sarca). Toce basin's slopes are mainly east oriented, and its climate is affected by the influence of Lake Maggiore. As it is the only basin where data are available in the Piemonte Region, we decided not to aggregate it with other basins (we denote the group simply as Toce). Since Serio and Brembo are the tributaries of the lower Adda, downstream Lake Como, and their slope is mainly oriented southward, facing Po River valley, they can be grouped in a unique macro-basin denoted as Serio-Brembo. Bitto and Mallero slopes are respectively North and South facing and both basins are tributaries of the upper Adda, oriented westward, upstream the Lake Como. Consequently, we aggregate Bitto, Mallero and Adda basins into one group (denoted as Adda). Oglio, Chiese and Sarca basins are fed by meltwater of the Adamello glacier; accordingly, we considered a unique macro basin called Oglio-Chiese-Sarca. We denote as Adige the macro-basin including its tributaries Noce and Valsura. Finally, we aggregate Piave, Brenta, Cismon and Cordevole in another group (denoted Piave-Brenta), most influenced by the Adriatic Sea.

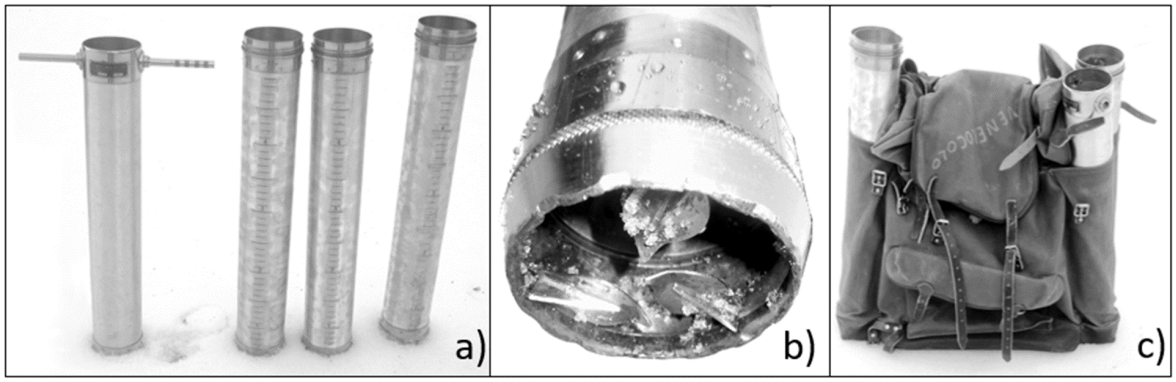

Figure 2.2: Photo of (a) CN2 type snow sampler and (b) detail of the cutting knife with the three internal fins and (c) the complete kit in its transporting bag.

2.2.2 Snow depth, snow density and snow water equivalent

We use a dataset of snow depth and snow density measurements collected between 1967 and 2020. The locations of the 299 measurement stations, reported in Figure 2.1, are fixed with minor displacements over the monitoring period. For each measurement station multiple measurements of snow depth were taken and then averaged. The choice of such locations is based on accessibility in every moment of the winter under normal meteorological conditions and representativeness of natural snow deposition, avoiding areas where avalanche snow might be collected or places where other forcings might change the snowpack height. The measurement dates are fixed in time on 1 February, 1 March, 1 April, 15 April, 1 May and 1 June, providing strong consistency for the timeseries analysis. Overall, 44'198 snow depth and 14'060 snow density measurements were collected and processed.
The tools adopted for height and density measurements of the snowpack have been designed by the Hydrographic Office of the Water Authority of Venice. One of the tools is a snow weighter CN2 type (Figure 2.2a), derived from the CN1 type, tested by the Snow Commission of the Glaciological committee, through small technical changes suggested by ENEL in order to make the use of it easier and faster. The CN2 type snow weighter is made of four tubular elements in duraluminium, each 50 cm long and with internal diameter of 7.2 cm. Screwable brass caps are attached to the ends of the four tubes, allowing to join two or more elements. On the side of each tube there are measurement notches from 0 to 50 cm in order to measure the exact height of the snow. The checking of this height is completed with a graduated rod, made of three pluggable elements in rust-proof alloy. Other accessories that complete the snow weighting tools set are: two snow cutting knifes (Figure 2.2b) applicable to the bottom of each of the duraluminium tubes, dynamometers for the weighting, a shovel for the digging of the trenches, nylon bags with rings to attach the dynamometers to, hammer and wrenches for the screwing of the tubes (Figure 2.2c). Only in recent years the probes used in some sites were substituted with Teflon probes with similar characteristics.

The measurement procedure of snow depth and density in case of snowpack height lower than 2 m starts with a first check of the snow depth with a graduated rod in order to pre-

pare the instrumentation with the proper number of tubular elements. Then, the instrument is thrust into the snowpack applying a constant pressure and continuous rotational movement until ground level, reading the snow depth measurement on the external notches. Finally, the instrumentation is extracted from the snowpack, depositing the collected sample in a nylon bag to be weighted. In case of snowpack deeper than 2 m, multiple extractions are necessary. A snow pit must be dig up to ground level, paying attention to maintain vertical the front wall. Then, an aluminum plate is inserted horizontally, a first sample is taken from the snowpack surface until the plate is reached and the partial depth measurement is recorded. The procedure is then repeated until the ground level is reached. The snow density is finally computed dividing the weight by the known volume of the sample. In case of snow depth measurement only, a simple graduated rod is adopted.

Each snow depth and snow density measurement is recorded together with the name of the drainage basin, average slope, orientation with respect to the North and elevation. We aggregated data in the six macro-basins described in the previous section in four elevation bands of equal range of 500 m (1000-1500, 1500-2000, 2000-2500 and 2500-3000 m a.s.l.). We performed a preliminary data quality check in order to remove possible erroneous data due to human mistake in the data recording. In case of snow depth, it might happen that a zero is recorded instead of a missing value. Specifically, we checked all the zero snow depth records by comparing them with the closest measurement points. If the snow depth measurements in the locations nearby the equivocal point are larger than a fixed threshold (set at 0.7 m) we consider that zero as a missing value. In the specific case of equivocal measurements in date 15 April, we also checked the previous and following date of measurement of that point. If in that location the snow depth on 1 April and 1 May is larger than 0.7 m we consider the equivocal zero as a missing value. In case of snow density measurements, we removed density values larger than a fixed threshold of 0.75 g cm^{-3}, considered far larger than typical snow density values (Allard, 1957; Marbouty, 1980).

We used the snow depth and snow density measurements that have passed quality check to estimate the SWE (mm) as

$$SWE = h_s \frac{\rho_s}{\rho_w} \tag{2.1}$$

Where h_s (mm) is the snow depth and ρ_s (kg m^{-3}) the snow density and ρ_w (kg m^{-3}) is the liquid water density simply estimated as 1000 kg m^{-3}. Since there is not a snow density measurement for each snow depth record, we assigned to ρ_s the measured snow density only if present. In case of missing snow density value in correspondence to the considered snow depth measurement, we assigned to ρ_s a mean value computed as the average of the other available snow density values measured in the corresponding date, macro-basin and elevation class. In case there are no density measurements in the corresponding geomorphic class, we consider the SWE data for the specific date, macro-basin and elevation class as missing. Finally, we obtained a timeseries ranging from 1967 to 2020 of average value snow depth and snow density for each macro-basin, elevation class and measurement date.

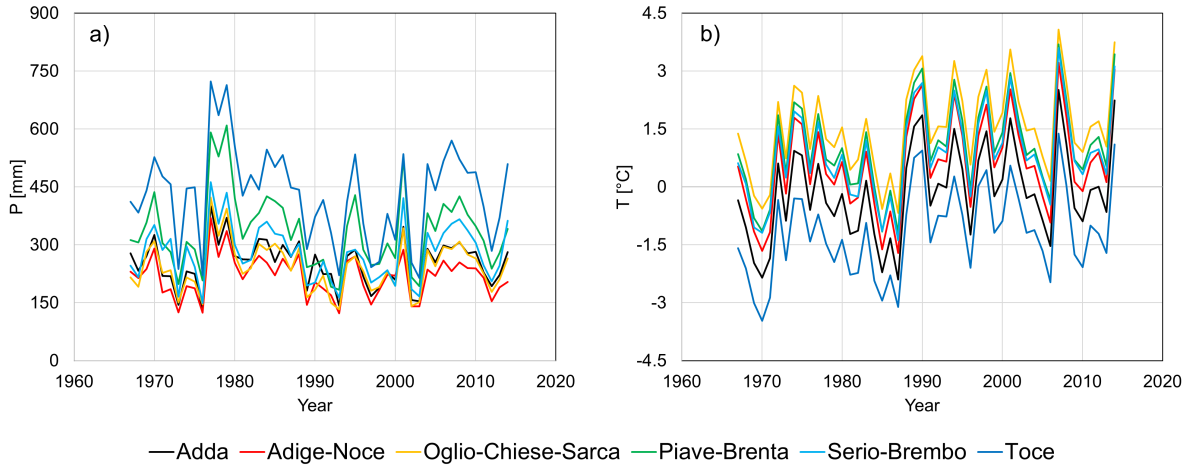

Figure 2.3: Timeseries of (a) cumulated precipitation and (b) air temperature averaged over the period DJFM from the HISTALP dataset, spatially averaged over the six macro-basins areas.

2.2.3 Temperature and precipitation data

Precipitation and temperature are the main meteorological variables regulating accumulation and melting of snow, with air temperature mainly governing the separation of solid and liquid precipitation and driving snowmelt. To evaluate the effects of precipitation and temperature variability on snow depth and SWE in the considered macro-basins, we consider the HISTALP dataset (Auer et al., 2007; Chimani et al., 2011). HISTALP is a multi-century-long (1780-2015) database of monthly homogenized records of temperature, pressure, precipitation, sunshine, and cloudiness for the Alps. Here, we consider the gridded precipitation and 2 m above ground level air temperature data, provided at 0.08° spatial resolution. Specifically, we considered the average temperature of December, January, February and March over the period 1967-2015. Since 1967, the number of the meteorological stations adopted to create the database and the distance between them have not changed (Auer et al., 2007), making the timeseries sufficiently reliable for the long-term variability and trends analysis. We extract from the gridded dataset the average temperature over each macro-basin reported in Figure 1. Accordingly, we consider the cumulated precipitation of December, January, February and March. The extracted timeseries are reported in Figure 2.3.

2.2.4 North Atlantic Oscillation and Western Mediterranean Oscilation indexes

Following the approach proposed by Ranzi et al. (2021), we evaluate the link of SWE with large scale circulation variability. Specifically, we consider the North Atlantic Oscilation (NAO) index and the Western Mediterranean Oscillation index (WeMO). NAO is a global circulation pattern index defined as the normalized surface sea-level pressure difference over the North Atlantic Ocean between the Subtropical (Azores) high and Subpolar (Iceland) low. It influences the European climate during winter (Osborn, 2011) and it presents a negative correlation with precipitation in the Italian Alps (Steirou et al., 2017; Zampieri et al., 2017; Brugnara and

Maugeri, 2019). WeMO index is a regional teleconnection pattern, spatially limited to the western Mediterrean basin (Martin-Vide and Lopez-Bustins, 2006). It is defined by the difference of monthly sea-level pressure between the Padua and San Fernando (Cádiz) stations. Here, we consider average DJFM NAO and WeMO indexes to address the links with spring snow depth measured in the considered Alpine basins.

2.2.5 Statistical and climatological analysis

In order to investigate possible variability and tendencies of snow depth and SWE during the monitored period we adopt three main methods of statistical analysis. At first, we compute the trend over the complete period 1967 – 2020 by means of a least-square linear regression. In order to test the statistical significance (p-value<0.05) of such trends we adopted the Mann – Kendall (MK) non-parametric test (Mann, 1945; Kendall, 1975) and the parametric Student's t test on the slope of the regression line, testing the null hypothesis H_0 of no trend against the alternative hypothesis H_1 of linear trend (Rosso and Kottegoda, 2008). Such trend analysis provides only one piece of information, even if important, related to the general tendency of the studied timeseries. The second analysis consists in a moving average and running trend analysis (MARTA from this point on), similarly to that reported in Brunetti et al. (2009) and Ranzi et al. (2021). MARTA consists in computing running trend and a moving average for all the possible sub-periods longer than 10 years, reporting the results in a chart where the central year of the sub-period is reported on the horizontal axis and its length on the vertical one. In the chart of the running trends, computed by least-square linear regression, slopes are represented by the color of the pixel. We represent on the plot each trend. However, statistically significant trends according to the MK (p-value<0.05) are represented by thicker pixels. In the chart of the moving averages, instead, all the sub-period averages are reported. MARTA is an effective exploratory data analysis and visualization tool, able to capture and highlight periods of values higher or lower than the long term mean in the timeseries. Here, we extend such approach taken from Brunetti et al. (2009) including a change detection analysis by means of the application of the Pettitt's test (Pettitt, 1979). Pettitt's test is a non-parametric technique to solve the change-point problem (i.e., identifying if and when the probability distribution of a stochastic variable has changed), testing the null hypothesis H_0 of no change. We graphically represent the change-point, if present, in the moving averages chart, indicating the year detected with the statistical test. As third analysis, in order to evaluate the global behavior of snow depth and SWE in each basin, we compute the difference between the averages of the two halves of the monitoring period 1967 – 1993 and 1994 – 2020. We test the statistical significance of such differences by means of the non-parametric Mann – Whitney U test (Mann and Whitney, 1947). In this case we test the null hypothesis that the probability of the considered variable between 1967 and 1993 being larger than between 1994 and 2020 is equal to the probability of the considered variable in the latter period being larger than the former.

Finally, we study the relationship and dependencies of snow depth and SWE with variability and changes in climate. We perform the same MARTA analysis to the temperature and precipitation timeseries presented above. Moreover, to evaluate the possible links between snow depth and the teleconnection indexes we evaluated the Pearson's correlation between the snow depth on 1

April and 15 April and the winter (DJFM) NAO and WeMO indexes.

2.2.6 Snow Water Equivalent model

To compute the SWE it is necessary to have a measurement of both snow depth and snow density (Allard, 1957). Empirical regressions of snow density over day of the year in the Italian Alps have been studied by several authors (e.g., Avanzi et al., 2015; Guyennon et al., 2019). Accordingly, we evaluated the average temporal evolution of snow density during the monitoring period updating with our new dataset the parameters of the model proposed by Guyennon et al. (2019), who found that the temporal evolution of snow density is well described by a quadratic polynomial function of the day of the year as

$$\rho_s(DOY) = n_0 + n_1(DOY + 61) + n_2(DOY + 61)^2 \tag{2.2}$$

Where ρ_s is the snow density, DOY is the day of the year. Snow depth on the ground increases during the accumulation season and start decreasing after the melt onset. Concurrently, positive correlation between snow depth or SWE and elevation in the Alps are reported by many authors (Bavera and De Michele, 2009; Durand et al., 2009; Lehning et al., 2011; Grunewald et al., 2014). Accordingly, we propose a snow depth model linearly dependent on elevation and with time dependent coefficients. For each macro-basin and measurement date we estimate the best fitting linear model of average observed snow depth as a function of elevation as

$$h_s(H, DOY) = m(DOY)[H - H_0(DOY)] \tag{2.3}$$

Where h_s is the snow depth, H is the elevation above sea level, m the slope and H_0 the elevation of null snow depth in the regression (snow line elevation). In such way, we reconstruct the elevation dependency of snow depth at different moments of the accumulation and melting seasons. Hence, the temporal dependency is contained in the coefficients m and H_0,, computed for each available measurement date. In order to obtain a continuous estimate of snow depth as function of both elevation (H) and time (DOY), we fit the computed m and H_0 using a third-order polynomial curve as

$$m(DOY) = a_0 + a_1(DOY) + a_2(DOY)^2 + a_3(DOY)^3 \tag{2.4}$$

$$H_0(DOY) = b_0 + b_1(DOY) + b_2(DOY)^2 + b_3(DOY)^3 \tag{2.5}$$

Where a_0, a_1, a_2, a_3, b_0, b_1, b_2 and b_3 are obtained by a least-square best fitting procedure. By substituting Equation 3.4 and in Equation and then Equation and in Equation , we obtained a simple model to estimate the SWE as function of both elevation and time. The parameters of the proposed model are calibrated for the two periods mentioned above (1967-1993 and 1994-2020) and for each macro-basin. Because of the scarcity of measurements above 2500 m asl, it is not easy to determine whether a maximum threshold is reached at higher altitudes. However, considering that at higher altitudes the major slopes tend to trigger avalanches and the blowing winds tend to prevent snow deposition, we assume, based also on the available observations,

that our altitudinal trends can be extrapolated up to 2500 m asl and a plateau value can be assumed above such altitude. Of course, such threshold is dependent on the topography of the considered basin and a larger number of high-elevation measurements is needed to provide a better estimate of the elevation of the plateau.

2.3 Results and discussion

2.3.1 Snow depth

We computed the temporal trends of snow depth for each macro-basin, elevation class and date of measurement. In Figure 2.4 we report the timeseries of snow depth for the Toce and Oglio-Chiese-Sarca macro-basins on 1 April and 1 May, together with the equation of the linear model used to estimate the temporal trend. For each case, the snow depth timeseries shows a decreasing trend, with a slightly steeper regression line in case of Oglio-Chiese-Sarca region. The results for each macro-basin, elevation class and date of measurement are reported in Table 2.1. The 57% of the cases exhibits a 95% statistically significant decreasing trend according to the MK or Student's t test, in accordance with the results found by Matiu et al. (2021). We found that absolute value of the long-term trend slopes increase moving from winter (i.e., 1 February and 1 March measurements) to spring (1 and 15 April and 1 May). These are common results across all macro-basins. For the Serio-Brembo macro-basin we obtained the strongest decreasing trend in the elevation class 2000-2500 in the date of 15 April, with a decrease of snow depth of about 0.3 m every decade. The computed trends are coherent with the ones obtained by Schöner et al. (2019) who computed a decrease up to 0.12 m every decade in the southern regions of the Swiss and Austrian Alps for the monitoring period 1961-2012.

We report in Figure 2.5 the MARTA triangles for the same macro-basins of Figure 2.4. Such graphical representation of the running averages and trends highlights the temporal variability of the timeseries analyzed. In the centered moving averages plot is reported the change-point detected by the Pettitt's test. In case of Toce, we found a change-point in 1985 for the snow depth measured on 1 April while for the Oglio-Chiese-Sarca case we obtained a statistically significant change-point for both 1 April and 1 May timeseries in 1988 and 1989, respectively. Table 2.2 contains the statistically significant change-point years detected by the Pettitt's test. The 50% of the cases exhibits a statistically significant change-point according to the Pettitt's test. The change-points obtained range from 1980 to 1992, with 1989 being the mode and 1988 the median. Specifically, the most occurring results are 1986 (frequency f=19%), 1987 (f=19%), 1988 (f=25%) and 1989 (f=26%). Such late 1980s has first been found by Marty (2007) for the Alpine snow and later confirmed by Reid et al. (2015) at global scale.

Then, we evaluated the difference in average snow depth for each macro-basin, elevation class and date of measurement. Figure 2.6 shows the average snow depth computed over the monitoring periods 1967-1993 (red circles) and 1994-2020 (black circles). If the difference between the averages of the two samples is statistically significant according to the Mann-Whitney U test, the circles are filled. To improve readability of the plot, an upward or downward blue arrow is reported if an increasing or a decreasing statistically significant trend is present (Table 2.1), respectively. In case of the Toce basin, at the lower altitudes, a statistically significant

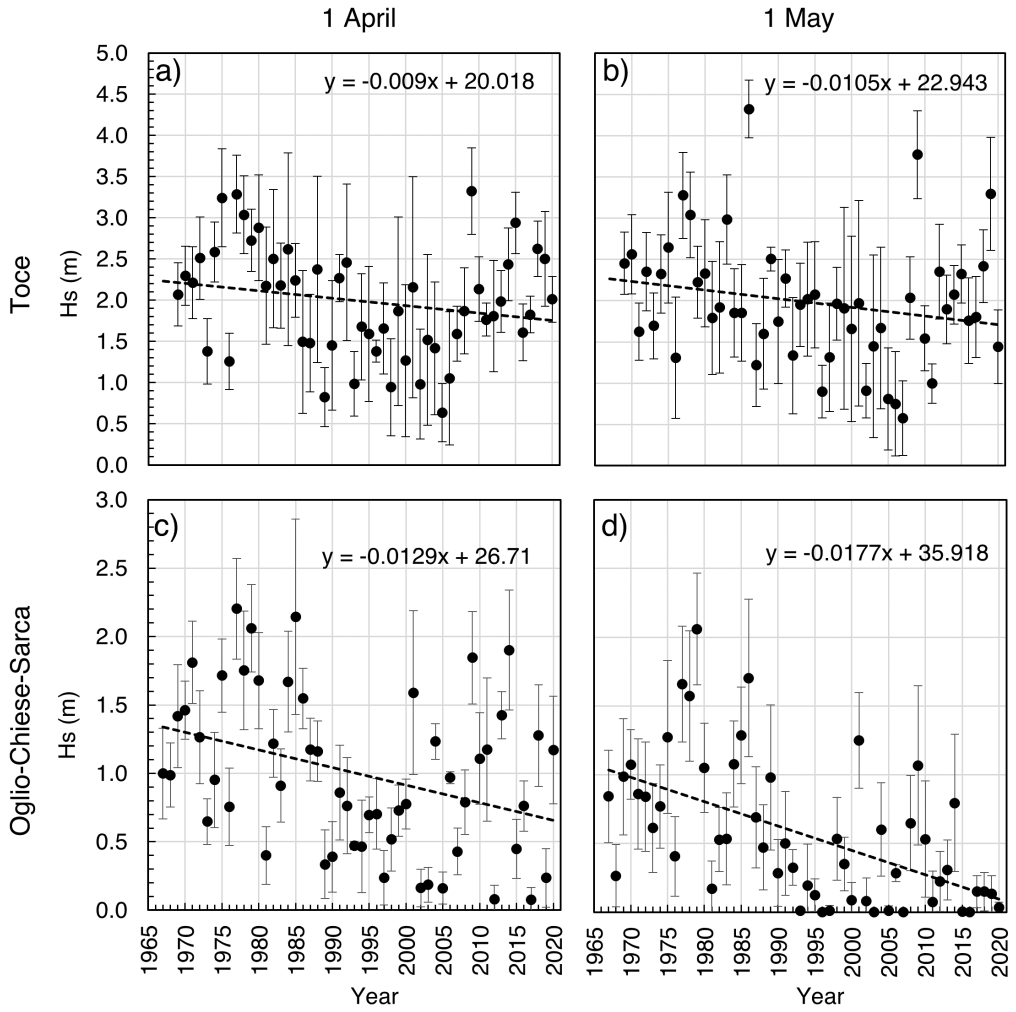

Figure 2.4: Time series average of snow depth (black dots) in Toce (a, b) and Oglio-Chiese-Sarca (c, d) macro-basins on 1 April (a, c) and 1 May (b, d). Error bars indicate the standard deviation over the specific macro-basin and dashed lines the least-square interpolation line.

difference has been found only in April, together with a statistically significant decreasing trend, with an average decrease of 0.32 m. However, in the elevation class 1500-2000 the difference in snow depth in the two periods is statistically significant from 1 March to 1 June, with a decrease of 0.37 m; in the elevation class 2000-2500 the average difference between the two periods is 0.38 m, statistically significant from 1 April. The Serio-Brembo and Oglio-Chiese-Sarca macro basins exhibits the strongest differences between the two periods, statistically significant for the 90% of the cases. At the lowest altitudes the difference between the two periods is similar, with an average decrease of 0.28 m (1000-1500) and 0.39 m (1500-2000) for Oglio-Chiese-Sarca and of 0.26 m (1000-1500) and 0.41 m (1500-2000) for Serio-Brembo. In the elevation class 2000-2500 the difference between the two periods in Serio-Brembo macro-basin (0.78 m) is more than twice larger than the one obtained for Oglio-Chiese-Sarca (0.33 m). Measurements of snow depth in the elevation class 2500-3000 show a statistically significant difference of 0.54 m on average starting from 1 April in the Oglio-Chiese-Sarca macro-basin. We found a similar behavior in Adda basin for the elevation classes 1500-2000 and 2000-2500, with a statistically significant difference of 0.39 m and 0.4 m, respectively. The Adige basin exhibits fewer statistically signif-

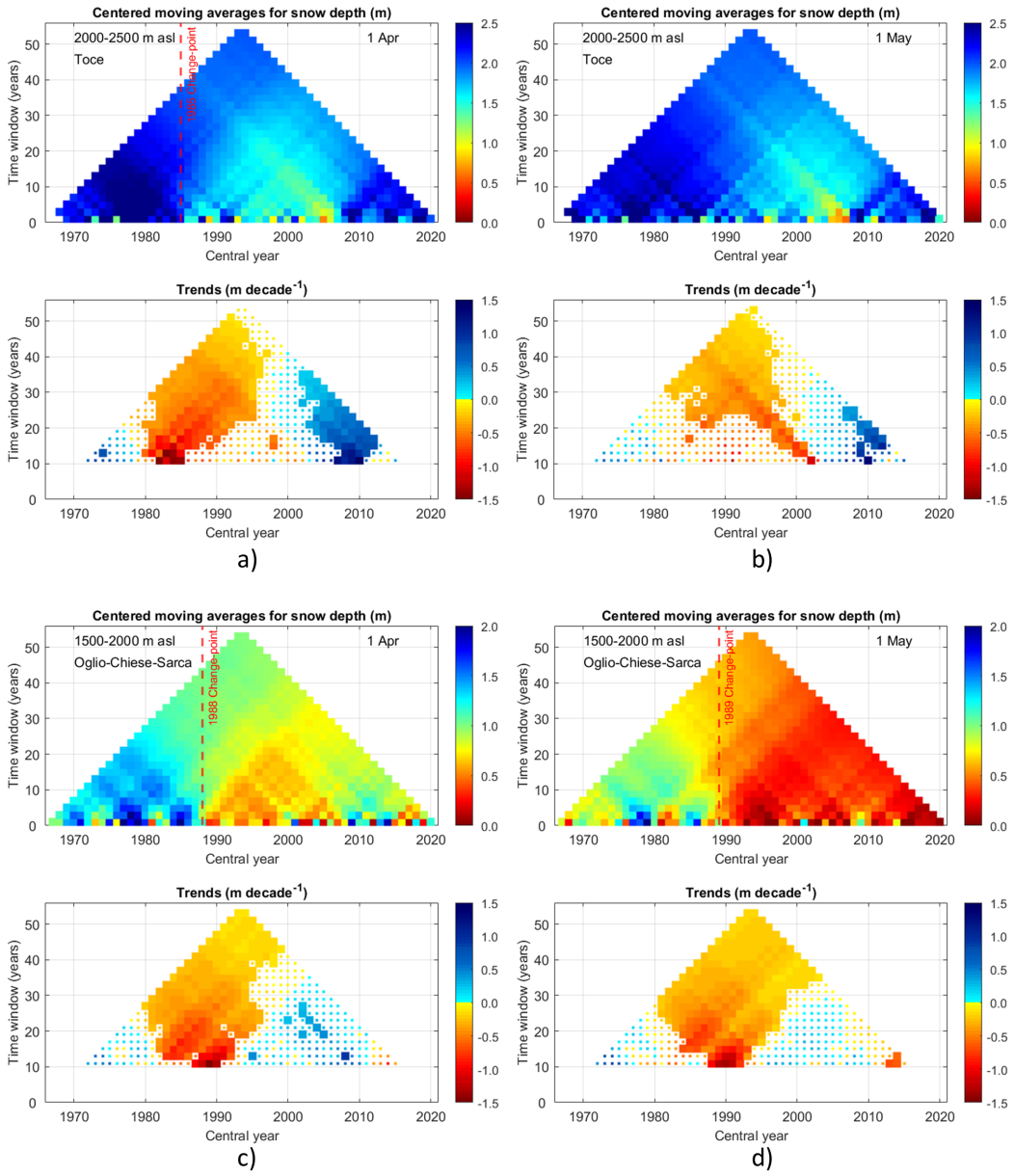

Figure 2.5: Moving Average and Running Trend Analysis (MARTA triangles) of snow depth on 1 April (a, c) and 1 May (b, d) in the altitudinal class 1500-2000 m asl for the Toce and 2000-2500 m asl for the Oglio – Chiese – Sarca macro-basins. In the top part of each panel the statistically significant change point detected by the Pettitt's test (5% significance) is reported as dashed line while in the bottom part the statistically significant trends with 5% significance level of the Mann-Kendall test are reported as thicker pixels.

EC	Date	Temporal trend (1967-2019) of snow depth (m decade^{-1})					
		Macro-basin					
		Toce	S-B	O–C–S	Adda	Adige	P–B
1000 – 1500	1 Feb	-	-0.08	-0.07	ND	-	-0.04*
	1 Mach	-	-0.07	-0.09	ND	-	-
	1 Apr	-0.12	-0.10	-0.10	ND	-	-0.07
	15 Apr	-0.10	-0.05	-0.10	ND	-	-0.07
	1 May	-0.06*	ND	-0.06	ND	-	-0.04
	1 June	-	-	-	ND	-	-
1500 – 2000	1 Feb	-	-	-	-	-	-
	1 Mach	-0.09	-0.10*	-0.09	-	-	-
	1 Apr	-0.14	-0.18	-0.13	-	-	-
	15 Apr	-0.17	-0.21	-0.15	-0.13	-	-0.12
	1 May	-0.16	-0.18	-0.18	-0.13	-0.07	-0.13
	1 June	-0.06	-0.08	-0.04	-0.06	-0.02*	-0.03*
2000 – 2500	1 Feb	-	-0.18	-	-	-	-0.05*
	1 Mach	-	-0.24	-0.09*	-0.08*	-	-
	1 Apr	-	-0.27	-0.11	-	-	-
	15 Apr	-	-0.31	-0.13	-0.13*	-	-0.10
	1 May	-	-0.29	-0.16	-0.16	-0.07*	-0.09
	1 June	-0.18	-0.24	-0.08	-0.11	-0.04	-
2500 – 3000	1 Feb	ND	ND	-	ND	-	ND
	1 Mach	ND	ND	-	ND	-	ND
	1 Apr	ND	ND	-0.12*	ND	-	ND
	15 Apr	ND	ND	-0.19	ND	-	ND
	1 May	ND	ND	-0.19	ND	-	ND
	1 June	ND	ND	-0.19	ND	-0.17	ND

Table 2.1: Trends of snow depth (1967 – 2019) for each macro-basin, elevation class (EC) and date. Statistically significant results according to Mann – Kendall and Student's t tests only are reported. If only one test is passed the trend is marked with an asterisk while cases in which there is not enough data are flagged as ND (no data).

icant differences, mainly in the two central elevation classes, with an average decrease of 0.21 m (1500-2000) and 0.19 m (2000-2500). In the Piave-Brenta basin the difference in snow depth between the two periods results statistically significant in 89% of the cases at the three lowest elevation classes, with a decrease of 0.21 m (1000-1500) and 0.29 m (1500-2000 and 2000-2500). These results are coherent with the decrease computed by Lejeune et al. (2019) for a mid-altitude (1325 m asl) mountain site in France (Col de Porte). They estimated a decrease of 0.39 m in snow depth between the 1969-1990 and 1991-2017 periods. The results obtained show different trends for the considered regions. In view of this, Matiu et al. (2021) pointed out the difficulties in generalizing the results to the whole Alpine area

Finally, we evaluated the elevation dependency of snow depth in each macro-basin for each measurement date. In Table 2.3 we report the values of m and H_0 least-square regression coefficients fitting average snow depth vs altitude in Equation . Since the results of the Mann – Whitney U test suggest that there is, in general, a statistically significant difference between the first and second halves of the observation period, we present the results for both 1967 – 1993

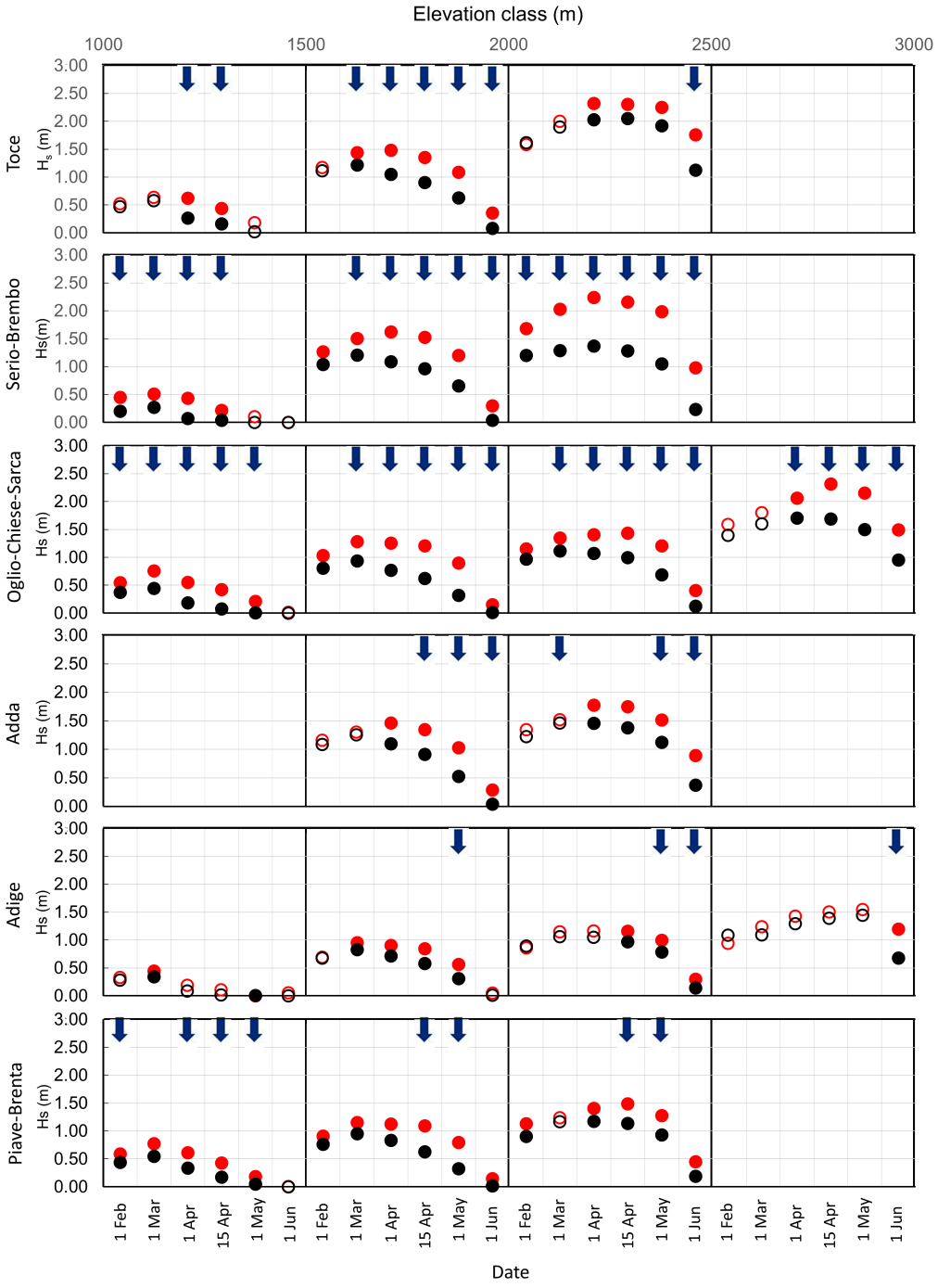

Figure 2.6: Average snow depth (H_s) in the 1967-1993 (red circles) and in 1994-2020 (black circles) periods are plotted for each elevation class in the six observation campaigns dates (1 Feb, 1 Mar, 1 Apr, 15 Apr, 1 May, 1 Jun). Statistically significant ($p \geq 0.01$, Mann-Kendall test) trends of the entire 1967-2020 period are sketched as upward (downward) blue arrow for increasing (decreasing) trends. Circles are filled if the difference of H_s between the two periods is statistically significant ($p \geq 0.01$, Mann-Whitney U test).

EC	Date	Change point (year)					
		Macro-basin					
		Toce	**S-B**	**O–C–S**	**Adda**	**Adige**	**P–B**
1000 – 1500	**1 Feb**	-	1987	1988	ND	-	-
	1 Mach	-	-	1989	ND	-	-
	1 Apr	-	-	1988	ND	-	1988
	15 Apr	-	-	1986	ND	-	1988
	1 May	-	ND	1989	ND	-	1989
	1 June	-	-	-	ND	-	-
1500 – 2000	**1 Feb**	-	-	-	-	-	-
	1 Mach	1987	-	1989	-	-	1989
	1 Apr	1988	1988	1988	1988	-	1988
	15 Apr	1989	1988	1988	1988	-	1988
	1 May	1986	1986	1989	1986	-	1989
	1 June	1987	1989	1992	1987	-	-
2000 – 2500	**1 Feb**	-	1986	-	-	-	-
	1 Mach	-	1989	1989	1980	-	-
	1 Apr	1985	1987	1987	1985	-	1988
	15 Apr	-	1987	1989	1986	-	1987
	1 May	-	1989	1992	1986	-	1989
	1 June	1986	1987	1987	1987	-	-
2500 – 3000	**1 Feb**	ND	ND	-	ND	-	ND
	1 Mach	ND	ND	-	ND	-	ND
	1 Apr	ND	ND	1986	ND	-	ND
	15 Apr	ND	ND	1989	ND	-	ND
	1 May	ND	ND	1990	ND	-	ND
	1 June	ND	ND	1986	ND	1986	ND

Table 2.2: Years of change-point detected by Pettitt's test in snow depth timeseries for each macro-basin, elevation class (EC) and date. Otatistically significant results only are reported while cases in which there is not enough data are flagged as ND (no data).

and 1994 – 2020 sub-periods. Together with the coefficients obtained from the linear regression analysis, we report the R^2 values for each case as an indicator of goodness of the fitting function. The Oglio-Chiese-Sarca, Serio-Brembo and Piave-Brenta macro-basins show higher values of R^2 and a common behavior of m and H_0. In fact, in these basins, m increases after February (accumulation) showing a peak value in spring, reinforced by the earlier onset of the melting season at lower elevations, and then decreases as melting develops at higher elevations. In fact, during the accumulation period the principal factor affecting m is the change from rain to snow with elevation while during the melt period it is more affected by the variation in melt with elevation (Allard, 1957). On the other hand, H_0 exhibits an almost stable or decreasing behavior during the accumulation phase, strongly increasing as the melting season starts. We also observe that H_0 exhibits higher values in the second half of the monitoring period, indicating that the elevation of null snow depth has moved towards higher altitudes, accordingly to the hypothesis of decreasing snow depth. Such results confirm the tendency modelled by Giorgi et al. (1997) who studied the elevation dependency of surface climate change impacting snow depth over the Alpine region. The results obtained for Adige, Adda and Toce basins show less reliable results according to the lower values of R^2 obtained and the physically meaningless negative values of

H_0, mainly due to the lower number of snow depth measurements.

Basin	Date	1967 - 1993			1994 - 2020		
		m [m/km]	H0 [m]	R2	m [m/km]	H0 [m]	R2
Toce	1 Feb	0.95	593	0.007	1.023	718	0.343
	1 Mach	1.24	650	0.011	1.23	742	0.408
	1 Apr	1.74	941	0.04	1.72	1113	0.509
	15 Apr	1.97	1092	0.068	1.93	1241	0.570
	1 May	2.24	1276	0.121	2.19	1427	0.621
	1 June	2.19	1483	0.262	1.57	1571	0.589
Serio Brembo	1 Feb	1.37	909	0.710	0.91	776	0.616
	1 Mach	1.72	957	0.680	0.83	495	0.310
	1 Apr	1.94	1027	0.582	0.94	712	0.430
	15 Apr	2.12	1128	0.743	1.37	1204	0.644
	1 May	2.13	1260	0.708	1.63	1458	0.280
	1 June	1.23	1522	0.466	1.51	1801	0.403
Oglio Chiese Sarca	1 Feb	0.67	375	0.817	0.69	703	0.725
	1 Mach	0.66	26	0.623	0.79	697	0.696
	1 Apr	0.98	638	0.781	1.07	1145	0.745
	15 Apr	1.22	899	0.784	1.15	1269	0.788
	1 May	1.25	1115	0.791	1.04	1425	0.704
	1 June	0.9	1491	0.515	0.68	1643	0.410
Adda	1 Feb	0.27	-2617	0.013	0.78	1.57	0.235
	1 Mach	0.07	-17704	4.00E-04	0.52	-770.71	0.069
	1 Apr	0.03	-59185	3.00E-05	0.78	288.63	0.111
	15 Apr	0.61	-517	0.017	1.18	1003.38	0.215
	1 May	0.65	-25	0.017	1.73	1504.91	0.379
	1 June	1.66	1638	0.133	1.72	1884	0.676
Adige	1 Feb	0.34	-209	0.663	0.54	570	0.465
	1 Mach	0.43	-341	0.633	0.43	-12	0.668
	1 Apr	0.75	643	0.776	0.78	933	0.589
	15 Apr	0.89	886	0.800	0.98	1197	0.907
	1 May	1.16	1298	0.855	1.16	1442	0.862
	1 June	1.09	1692	0.745	0.49	1634	0.530
Piave Brenta	1 Feb	0.51	92	0.528	0.53	385	0.630
	1 Mach	0.67	101	0.567	0.70	424	0.603
	1 Apr	0.94	646	0.814	0.90	840	0.649
	15 Apr	1.24	953	0.850	1.48	1109	0.742
	1 May	1.16	1144	0.859	0.95	1292	0.709
	1 June	0.53	1333	0.373	0.43	1462	0.408

Table 2.3: Linear regression coefficients (m and H0) and R^2 of the least-square linear fitting of average snow depth and elevation for the two sub-periods 1967-1993 and 1994-2020.

2.3.2 Snow density

In order to investigate possible variability and tendencies of snow depth and SWE, we evaluated snow density data variations with elevation and in time. In Figure 2.7 we show the snow density plotted as a function of the elevation, for the six considered measurement dates, in the Piave-Brenta macro basin. We found that, within each elevation class, snow density does

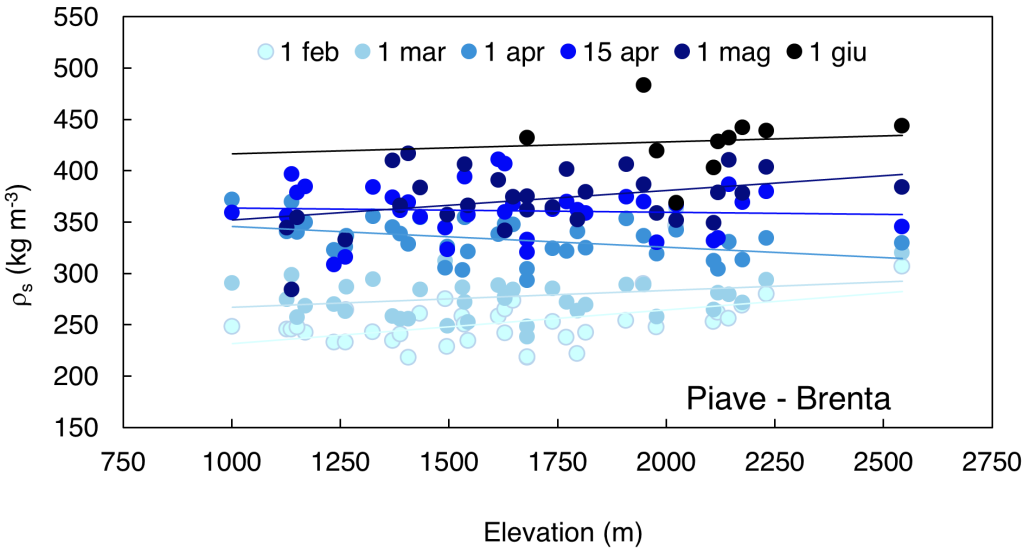

Figure 2.7: Snow density (ρ) dependence on elevation for the macro-basin Piave-Brenta. Average snow density for each measurement date is represented with different color intensity with changing date of the year.

not substantially vary with elevation for a specific measurement date. On the other hand, we found that snow density increases with measuring date. Such behavior is common among all the macro-basins studied. In Figure 2.8 we report the average snow density computed over the monitoring period. From a least-square fitting of Equation we obtained new values for the polynomial coefficients, better modelling the data here presented (R^2=0.998) and compared with the model from Guyennon et al. (2019). Specifically, we obtained n_0=277, $n_1 10^{-1}$=-3.6 and $n_2 10^{-3}$=5.1. Such seasonal increase of snow density is related to different processes such as compaction, increase of liquid water in the snowpack due to melting as the temperature increases.

2.3.3 Snow water equivalent

For the available SWE estimates, we computed the temporal trends for each macro-basin, elevation class and date of measurement. In Table 2.4 we report the temporal trends computed over the monitoring period 1967-2020. Obviously, the general behavior is in accordance with the one found in case of snow depth. Among the considered timeseries, we obtained statistically significant trends in 44% of the cases according to the MK or Student's t test, mainly in the Oglio-Chiese-Sarca macro-basin. In this macro-basin, the computed trends increase in terms of absolute value moving from winter to spring in the two lower elevation classes, reaching the maximum between 15 April (-36 mm every decade for 1000-1500) and 1 May (-67 mm every decade for 1500-2000); in the two higher elevation classes we found statistically significant trends for the measurement dates of 15 April, 1 May and 1 June, suggesting that the spring snow has been more strongly affected in the past decades, reaching the maximum absolute value in May (-48 mm every decade for 2000-2500 and -67 mm every decade for 2500-3000). In Table 2.5 we report the results of the change-point analysis performed by means of the Pettitt's test.

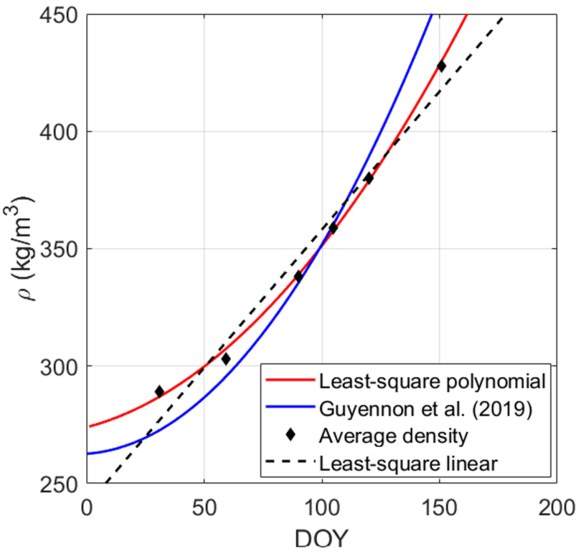

Figure 2.8: Temporal variability of snow density (ρ). Average snow density for each measurement date is represented as black diamond. We also report in red the computed polynomial model, in blue the one proposed in Guyennon et al. (2019) and a linear model as black dashed line.

The change-points obtained range from 1986 to 1991, with 1988 being both mode and median. Specifically, the most occurring change-point years are 1989 (f=17%), 1986 (f=27%) and 1988 (f=46%). The Pettitt's test confirms on a sound statistical basis the findings of other studies, such as Marty et al. (2017), based on SWE measurements, and Colombo et al. (2022), based on snow depth measurements and SWE modelling. Valt and Cianfarra (2009) obtained similar results, finding breakpoints between 1984 and 1994. Also in this case, the Oglio-Chiese-Sarca macro-basin exhibits statistically significant results for the largest cases of elevation classes and measurement dates. For this specific macro-basin, we found the statistically significant change points mainly April and May, in agreement with the results obtained for the long-term trends. As for the case of snow depth, we evaluated the difference in average SWE for each macro-basin, elevation class and date of measurement. In Figure 2.9 we report the average SWE computed over the monitoring periods 1967-1993 (red circles) and 1994-2020 (black circles). The Oglio-Chiese-Sarca macro-basins presents statistically significant results in most cases. We found that the largest statistically significant differences in SWE between the two periods is in Spring, for the measurement dates of 1 April and 15 April for the 1000-1500 elevation class and 15 April and 1 May for the other cases. The average difference between the two periods is 85 mm for the elevation class 1000-1500, 135 mm for 1500-2000, 104 mm for 2000-2500 and 226 mm for 2500-3000. The Piave-Brenta macro-basin shows similar results, with statistically significant differences in 89% of the cases. We found the largest statistically significant differences on 1 April and 15 April for the 1000-1500 elevation class, with an average difference of 59 mm, on 15 April and 1 May for the 1500-2000 elevation class, with an average difference of 82 mm, and 1 May and 1 June for 2000-2500 elevation class, with an average difference of 78 mm. For the Adige basin we found statistically significant differences mainly in the 1500-2000 elevation class, with an average difference of 70 mm. For the Toce and Serio-Brembo macro-basins the

EC	Date	Temporal trend (1967-2019) of SWE (mm decade^{-1})					
		Macro-basin					
		Toce	S-B	O–C–S	Adda	Adige	P–B
1000 – 1500	1 Feb	ND	ND	-11*	ND	-	-
	1 Mach	ND	ND	-22	ND	-	-
	1 Apr	ND	ND	-34	ND	ND	-
	15 Apr	ND	ND	-36	ND	ND	-22
	1 May	ND	ND	-21	ND	ND	-14
	1 June	ND	ND	-2*	ND	ND	-
1500 – 2000	1 Feb	-	-	-24	-	-	-
	1 Mach	ND	ND	-27*	-	-	-
	1 Apr	-121	-55*	-43	-	-	-
	15 Apr	ND	-	-59	-	-	-37
	1 May	-85*	-69	-67	-	-	-47
	1 June	-24*	-22*	-21	-	ND	-15*
2000 – 2500	1 Feb	-	-78	-	-	ND	-19*
	1 Mach	ND	ND	-	-	ND	-
	1 Apr	-281	-113	-	-	ND	-
	15 Apr	ND	-191	-38	-	ND	-
	1 May	-	-125	-48	-	ND	-23*
	1 June	ND	-92	-30	-	-	-
2500 – 3000	1 Feb	ND	ND	-	ND	-	ND
	1 Mach	ND	ND	-	ND	-	ND
	1 Apr	ND	ND	-	ND	-	ND
	15 Apr	ND	ND	-61	ND	-	ND
	1 May	ND	ND	-67	ND	-	ND
	1 June	ND	ND	-58*	ND	-55	ND

Table 2.4: Trends of snow water equivalent (SWE, 1967–2019) for each macro-basin, elevation class (EC) and date. Statistically significant results according to Mann–Kendall and Student's t tests only are reported. If only one test is passed the trend is marked with an asterisk while cases in which there is not enough data are flagged as ND (no data).

estimate of SWE appears less robust than in the other basins, mainly because of the fewer available measurements of snow density, resulting in more scattered timeseries in Figure 2.9. The Adda basin exhibits statistically significant differences in the 1500-2000 and 2000-2500 elevation classes, with an average difference of 141 mm and 104 mm, respectively. Similarly, Marty et al. (2017) observed a stronger decrease of SWE at higher altitudes. Moreover, they also found larger decreases for April SWE than for February SWE, in agreement with our results.

2.3.4 Climate variability

In order to evaluate possible links between climate variability and changes occurred during the monitoring period and the amount and persistence of snow in the considered macro-basins, we performed the MARTA analysis to temperature and precipitation data. Specifically, we considered the average DJFM precipitation and temperature obtained from the HISTALP dataset. We report the results of the precipitation analysis in Figure 2.10 and the temperature analysis in Figure 2.11. For all the considered macro-basins, DJFM precipitation exhibits a slight non-

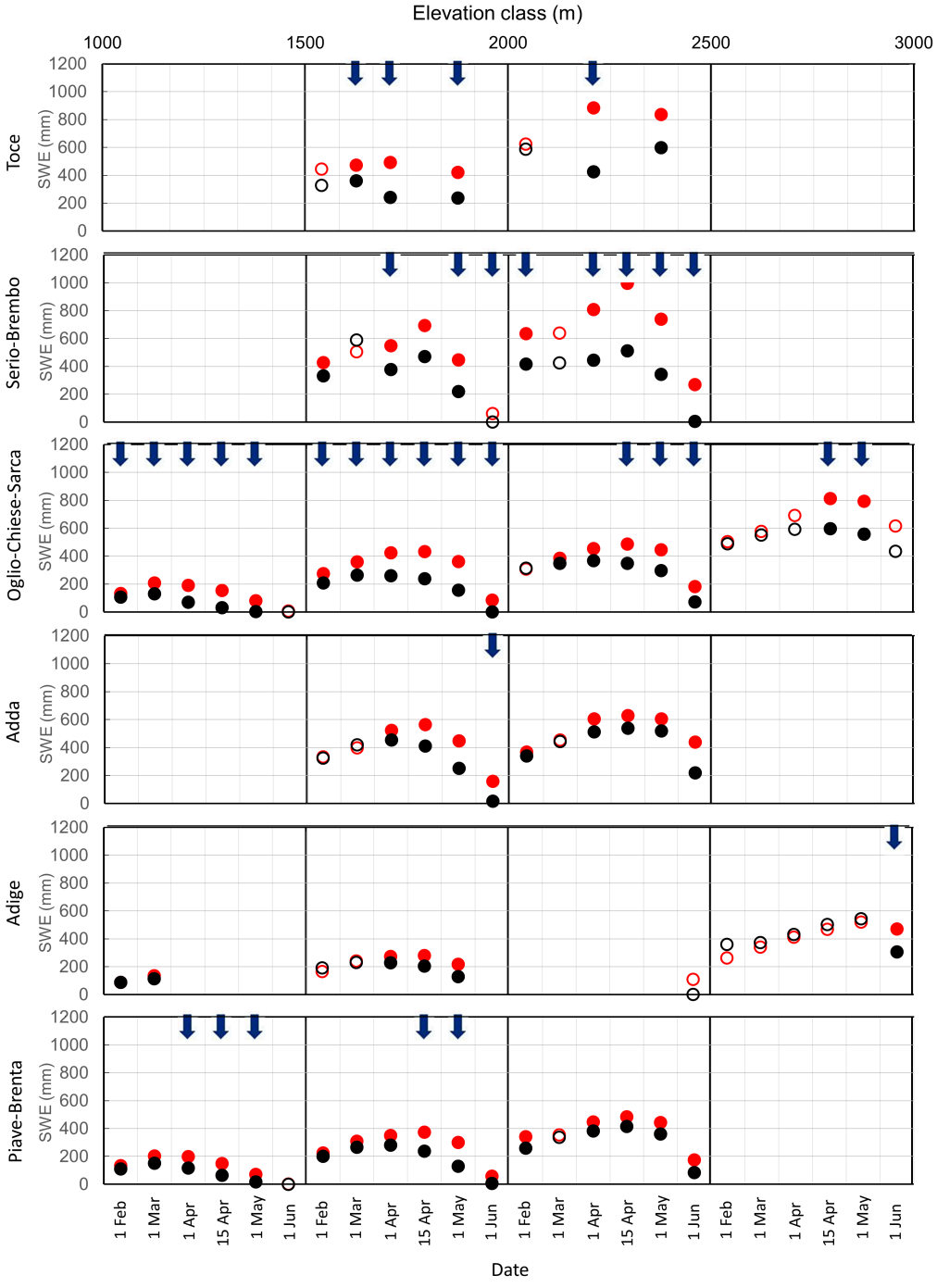

Figure 2.9: Average snow water equivalent (SWE) in the 1967-1993 (red circles) and in 1994-2020 (black circles) periods are plotted for each elevation class in the six observation campaigns dates (1 Feb, 1 Mar, 1 Apr, 15 Apr, 1 May, 1 Jun). Statistically significant ($p \geq 0.01$, Mann-Kendall test) trends of the entire 1967-2020 period are sketched as upward (downward) blue arrow for increasing (decreasing) trends. Circles are filled if the difference of SWE between the two periods is statistically significant ($p \geq 0.01$, Mann-Whitney test).

EC	Date	Change point (year)					
		Macro-basin					
		Toce	S-B	O–C–S	Adda	Adige	P–B
1000 – 1500	**1 Feb**	ND	ND	-	ND	-	-
	1 Mach	ND	ND	-	ND	-	-
	1 Apr	ND	ND	1988	ND	ND	1986
	15 Apr	ND	ND	1988	ND	ND	1988
	1 May	ND	ND	1989	ND	ND	1988
	1 June	ND	ND	-	ND	ND	-
1500 – 2000	**1 Feb**	-	-	-	-	-	-
	1 Mach	ND	ND	1988	-	-	-
	1 Apr	-	-	1988	-	-	1988
	15 Apr	ND	-	1988	-	-	1988
	1 May	-	1991	1989	-	-	1989
	1 June	-	-	-	-	ND	-
2000 – 2500	**1 Feb**	-	1986	-	-	ND	-
	1 Mach	ND	ND	-	-	ND	-
	1 Apr	-	1988	1987	-	ND	1988
	15 Apr	ND	-	1988	-	ND	-
	1 May	-	1990	1989	-	ND	1987
	1 June	ND	-	1986	-	-	-
2500 – 3000	**1 Feb**	ND	ND	-	ND	-	ND
	1 Mach	ND	ND	-	ND	-	ND
	1 Apr	ND	ND	1986	ND	-	ND
	15 Apr	ND	ND	1986	ND	-	ND
	1 May	ND	ND	1986	ND	-	ND
	1 June	ND	ND	1986	ND	-	ND

Table 2.5: Years of change-point detected by Pettitt's test in SWE timeseries for each macro-basin, elevation class (EC) and date. Statistically significant results only are reported while cases in which there is not enough data are flagged as ND (no data).

significant decrease over the monitoring period and no statistically significant change-point is detected according to the Pettitt's test (Figure 2.10). By looking at the sub-periods between 10 and 20 years, it is possible to notice three areas of statistically significant trends, showing an increase before 1980, a decrease around 1990 and another increase around 2000, confirming a non-uniform tendency over the complete monitoring period. We also performed the same statistical analysis to the HISTALP mean monthly temperature averaged over all the basins (not shown here), to evaluate possible differences in climate variability between accumulation and melting seasons. Temperature increases significantly in both the accumulation (from January to March) and, even more significantly, the melting period (April and May), consistently with results reported by many authors as Auer et al. (2007) and Brunetti et al. (2009). These results explain the decrease in snow depth and SWE on 1 April and the accelerated melt on 15 April – 1 June period. Both winter (DJFM) and spring (April and May) temperatures exhibit a marked increase after 1987, where a change-point is detected by the Pettitt's test. This result is consistent with the change-point detected in the snow depth and SWE timeseries, suggesting a strong impact of temperature increase, especially in spring, on snowmelt. The combined effect of precipitation and temperature variability is consistent with the observed stationarity of

winter (February and March) snow depth and SWE, the significant decrease of the maximum SWE observed in April and the accelerated melt in May. Marty et al. (2017) found similar result, linking the strong low elevation SWE decreases to temperature increases and decreasing snow/rain ratio. These results confirm the impact of temperature rise on snow, affecting consequently the hydrological cycle and water availability.
Finally, we evaluated the correlation between snow depth on 1 and 15 April and the DJFM NAO and WeMO indexes. In Figure 2.12 we report the matrixes of statistically significant Pearson's correlations, where the rows represent the six macro-basins and the columns the four elevation classes. We obtain a negative statistically significant Pearson's correlation between winter NAO and spring snow depth ranging between -0.30 and -0.55 for 1 April and between -0.29 and -0.49 for 15 April. These results are coherent with previous studies of several authors as Steirou et al. (2017) who found linkages between NAO and precipitation in Europe; Colombo et al. (2022) found a negative correlation between NAO and SWE indexes. The WeMO index exhibits an opposite link with snow depth, with positive statistically significant correlation ranging between 0.27 and 0.37 for 1 April and between 0.27 and 0.40 for 15 April, in agreement with the positive correlation between winter WeMO and precipitation (0.38) obtained by Ranzi et al. (2021).

2.3.5 Snow water equivalent model

Here we show the results obtained from the SWE regression model presented in Section 4.2, applied to the case of Oglio-Chiese-Sarca macro-basin. In Figure 2.13 we show the values of m (a) and H_0 (b) obtained from the linear regression analysis of average snow depth measurements for the monitoring period 1994-2020 (black diamonds) obtained from Table 2.3. We selected the Oglio-Chiese-Sarca macro basin as it shows the highest R^2 values (Table 2.3) and the second half of the monitoring period as more representative of the current nivological situation. The best fitting of Equation and are plotted as dotted black lines and the coefficients a_0, a_1, a_2, a_3, b_0, b_1, b_2 and b_3 are reported as well, together with R^2 values. The fitting curves well describe the observed behavior presented in Section 3.3.1, showing high values of R^2 (0.97 for m and 0.99 for H_0). Such fitting must be considered valid only within the considered time period as it might introduce strong uncertainty due to the low number of points adopted for the fitting procedure. However, the curve obtained provides an analytical function to estimate the temporal evolution of the linear regression coefficients m and H_0. Hence, the following equation can be written to model the SWE as function of time and elevation.

$$SWE(H, DOY) = m(DOY)[H - H_0(DOY)]\frac{\rho_s(DOY)}{\rho_w} \tag{2.6}$$

The coefficients n_0, n_1, n_2, to define the second-order polynomial function of ρ_s are reported in Section 3.3.2. With the estimates of m, H_0 and ρ_s obtained from the long-term snow depth and snow density observations it is possible to estimate the SWE in the DOY-H space as shown in Figure 2.14. From the contour plot, we observe that the DOY of maximum SWE for fixed elevation (DOY of the local minimum of the SWE isolines) linearly shifts in time, confirming the behavior observed in the previous sections. However, for elevations higher than 2500 m asl, we consider the model less reliable as the number of snow depth measurements is lower at

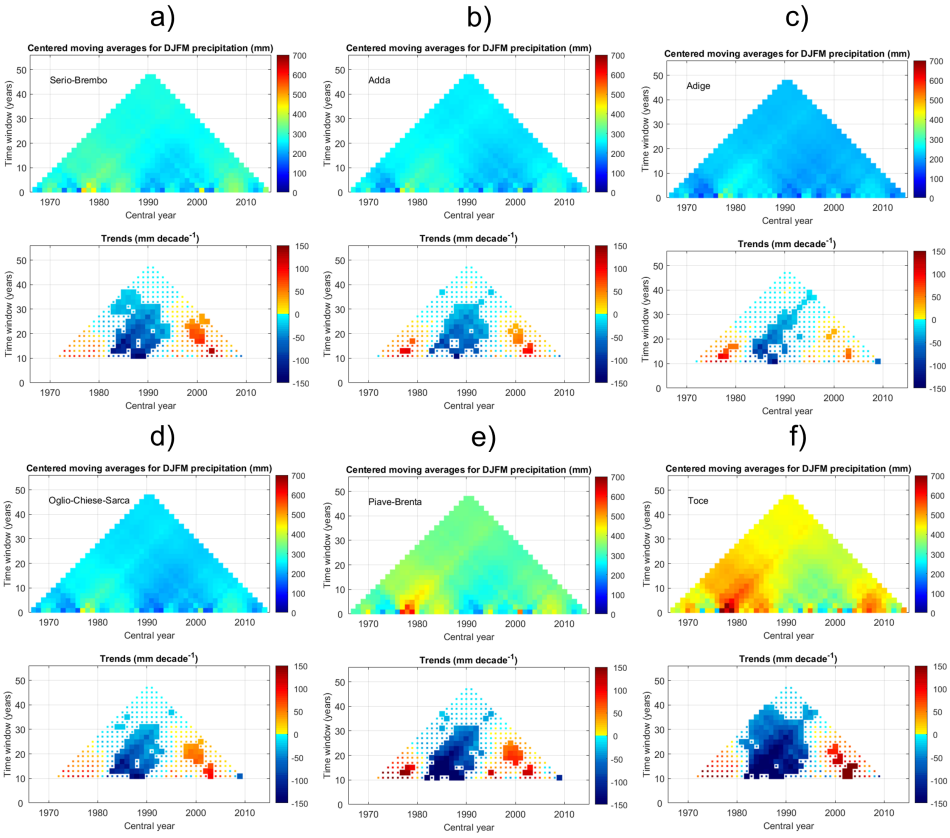

Figure 2.10: MARTA triangles of total winter (DJFM) precipitation for the six macro-basins from the HISTALP dataset. In the bottom part the statistically significant trends with 5% significance level of the Mann – Kendall test are reported as thicker pixels.

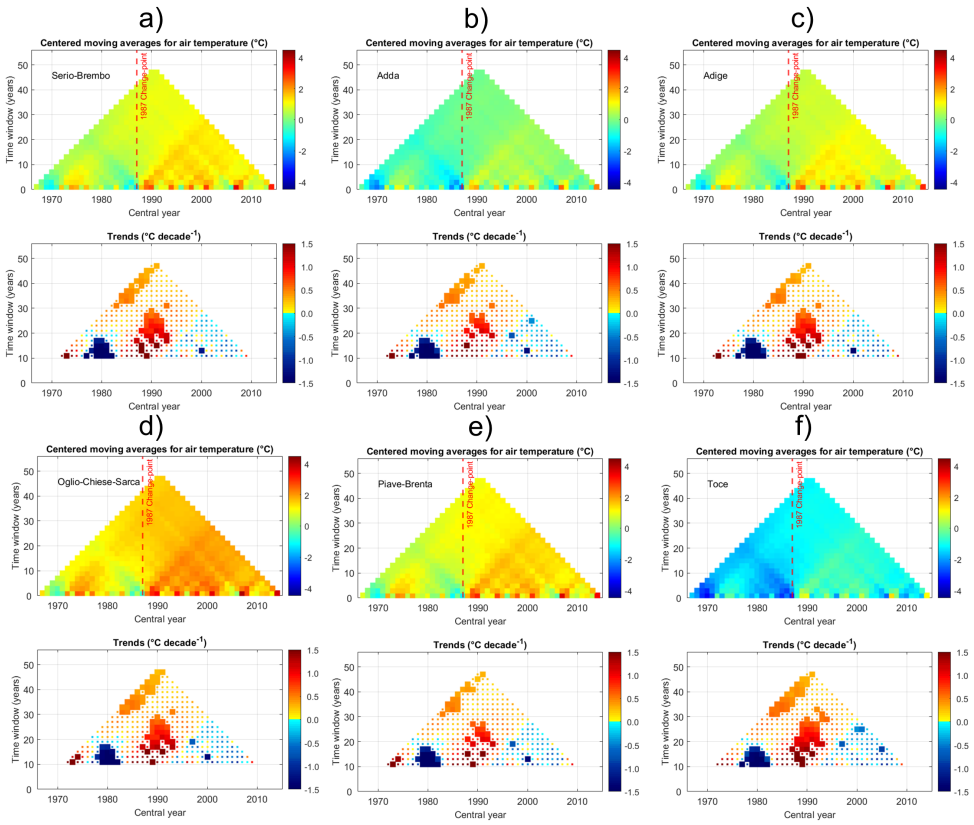

Figure 2.11: MARTA triangles of average winter (DJFM) temperature for the six macro-basins from the HISTALP dataset. In the top part of each panel the statistically significant change point detected by the Pettitt's test is reported as dashed line while in the bottom part the statistically significant trends with 5% significance level of the Mann – Kendall test are reported as thicker pixels.

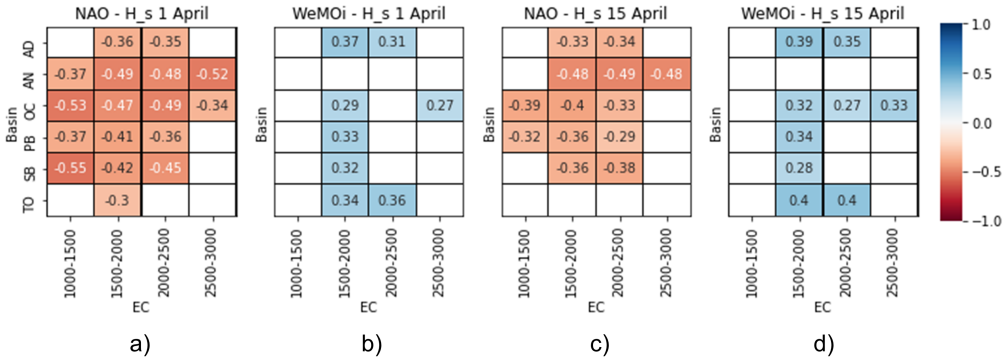

Figure 2.12: Statistically significant (p≥0.05) Pearson's correlation between winter average teleconnection indexes NAO (a and c) and WeMO (b and d) and the snow depth measured on 1 April (a and b) and 15 April (c and d) for the Toce (TO), Serio-Brembo (SB), Piave-Brenta (PB) Oglio-Chiese-Sarca (OC), Adige (AN) and Adda (AD) and for the four elevation classes (EC).

such elevation and above a certain point snow depth might reach a plateau or even decrease (Grünewald et al., 2014).

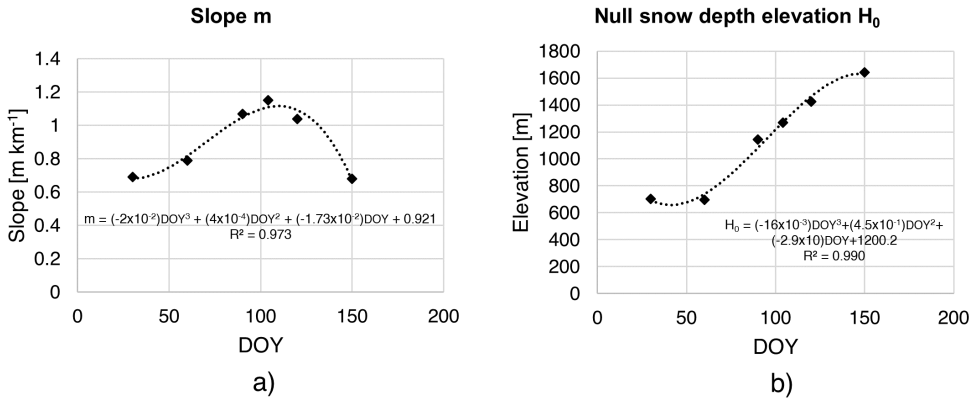

Figure 2.13: Slope m (a) and null snow depth elevation H_0 (b) as function of the day of the year (black diamonds). Dotted black line represents the third-order polynomial fitting curve (Equation and).

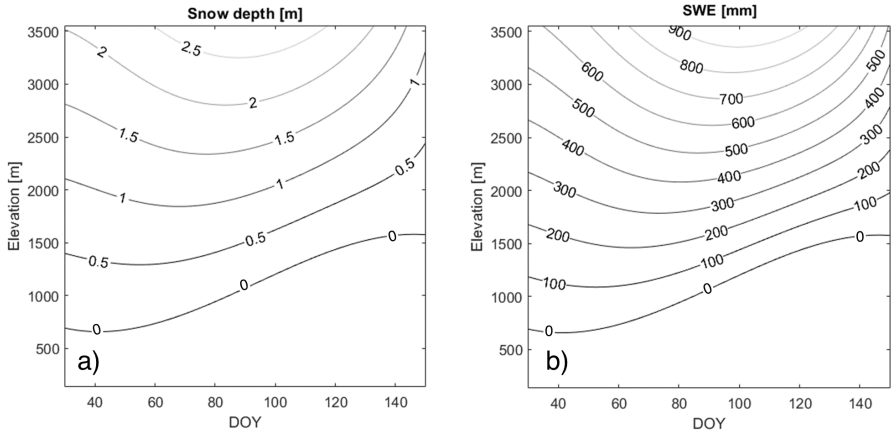

Figure 2.14: Contour plot of snow depth and snow water equivalent (SWE) in the time-elevation (DOY-H) space for the 1994-2020 period.

2.4 Conclusions

We studied changes and variability of snow depth and SWE in six macro-basins of the Italian Alps over the monitoring period 1967-2020 based on measurements collected on 1 February, 1 March, 1 April, 15 April, 1 May and 1 June. Our results show the effects of the temperature increase of the past century on snow accumulation in the Italian Alps. We found statistically significant decreasing trends in both snow depth (-0.12 m decade^{-1} on average in the Oglio-Chiese-Sarca basin) and SWE (-37 mm decade^{-1} on average in the Oglio-Chiese-Sarca basin) over the years and a statistically significant decrease of snow depth and SWE between the two halves of the monitoring period (1967-1993 and 1994-2020). Specifically, we found that, on average, snow depth decreased of 33% on 1 April, exhibiting stronger differences between the

two periods at lower altitudes (63% in the 1000-1500 m elevation class) and smaller difference towards higher elevations (29% at 1500-2000 m, 22% at 2000-2500 m and 18% at 2500-3000 m). In case of SWE we found an decrease of 36% with respect to the 1967-1993 period, higher at low elevations (52% at 1000-1500 m) and substantially lower at higher altitudes (between 28% and 29%). These results have been also confirmed by the higher values of snow line elevation H_0 we obtained. The computed trends and differences exhibit a strong change in spring (1 April and 15 April mainly) snow depth and SWE, suggesting that spring snowmelt is highly impacted by global warming. Such behavior can have strong effects on the hydrological regime of the considered catchments, possibly modifying magnitude and timing of flood events and affecting water availability in the summer.

We found that around 1988, on average, there has been a change-point, with snow depth and SWE being lower in the following decades. This appears to be a common result for all the macro-basins and elevations. To reject the hypothesis of possible errors in the snow depth and SWE timeseries due to measurement methodology variations or other factors affecting the timeseries reliability, we performed the same change-point detection analysis on measured temperature data from HISTALP dataset, resulting in a change-point in the same period. This result confirms the robustness of our findings and highlights the strong effects of temperature on snow amount and persistency, both in terms of rain-snow separation and melt onset. The analysis of precipitation and temperature data also confirms the weaker variation during the accumulation season (1 February and 1 March) in contrast with the strong decrease in snow depth and SWE during the melting season. The correlation analysis of NAO and WeMO climatological indexes with snow depth on 1 April showed similar correlations obtained in other studies. In fact, we found negative Pearson's correlation coefficient in case of NAO index and positive in case of WeMO index. Further investigations might highlight the impacts of the observed changes in climatological and nivological conditions on hydropower energy production.

The elevation and time dependency analysis of snow depth and snow density measurements allowed us developing a simple SWE model as a function of time and elevation. In fact, as shown in Figure 2.8, snow density changes significantly only with the day of the year, being almost constant with altitude. On the other hand, snow depth linearly increases with elevation and, of course, increases along the accumulation season and start decreasing as the melting season begins. From such analysis we obtained the parameters for a simple SWE model that can be applied to estimate the SWE evolution between February and July as function of the elevation and day of the year. Such model can be used to estimate SWE for local applications in the considered macro basins.

Chapter 3

Rain-On-Snow: the contribution of snowmelt to intense flood events in Lombardy

There is great vigour in the waters that come down from the snows of the Misty Mountains.

J.R.R. Tolkien,
The fellowship of the ring

Abstract

The contribution of snow on ground in the formation of floods has been investigated. We calibrated a snow water equivalent (SWE) accumulation and melting model to estimate a degree-day factor based on observed precipitation, temperature and snow depth, later used to quantify snowmelt in rain-on-snow days. We analyzed 27 years of precipitation observations collected at the meteorilogical stations of Aprica and Pantano d'Avio through the annual maxima (AM) method, obtaining the IDF curves of precipitation only (P) and combined precipitation and melting (P+M) for the two locations. We found an average increase in the quantiles of 2.2% when considering meltwater contribution, larger for longer durations, up to 10% for d=24 h with an average of 3.2% for Aprica and 4.1% for Pantano d'Avio. Future developments will include the analysis of longer durations (1,2,3,4,5 days), as meltwater contribution is expected to increase.

3.1 Introduction

Snow plays a role of paramount importance in the Alpine region, being a natural freshwater reservoir. On the one hand, snowmelt runoff is a major component of the hydrological cycle, regulating water availability for water supply systems. On the other hand, it can contribute to increase flood volumes in case of intense rainfall events. Rain-on-snow (ROS) events occur when

snow present on the ground is melting in conjunction with a rainfall event, possibly causing landslides, high streamflows (Berris and Harr, 1987) and avalanches (Conway and Raymond, 1993; Heywood, 1988). These events are characterized by a complex generation mechanism, mainly driven by air temperature, precipitation phase (i.e., solid or liquid) and, obviously, presence of snow on the ground (Il Jeong, 2017). Snow on ground can actually play a double role. From one point of view, it can slow down the formation of floods, retaining the rainfall volumes and delaying the occurance of peak flows. In fact, snow can be considered as a porous media and water can flow throug it according to a Darcian flow (Colbeck, 1972; Colbeck and Anderson, 1982). The water reteined by the snowpach can reach 6% of the snow depth. On the other hand, it can enhance the flood event by releasing additional runoff from melting and, consequently, contributing with additional water to the peak flow volume.
Climatological analysis of ROS present difficulties related to the combination of the mechanism generating ROS events. Trends are found of both signs, mainly because warmer temperatures result in both an increase of the ratio of rain to snow events and a decrease and disappearing of snow cover (Cohen et al., 2015). Snow cover in the Italian Alps has been decreasing since 1967 and precipitation data do not exhibit statistically significant trends over the same period, suggesting a decrease of possible ROS events. On the other hand, temperature has been increasing since 1967 and at an even faster rate since the end of the 1980. Such increase in air temperature could increase the number of rainy days in a year.
In a climate change scenario, intense flood events are however expected to increase in frequency. The estimate of flood peak flow for a given return period is in general carried out by taking into account a rainfall event with the same return period. Extreme rainfall statistical analysis is carried out through extreme value theory in order to obtain an estimate of the amount of precipitation for given return period. The Intensity-Duration-Frequency curves provide a model to evaluate the precipitation depth as a function of the duration and the return period. The methodology mostly adopted to build such model is the analysis of the annual maxima (AM), which considers a sample composed by the largest observation for every year of the available measured precipitation series.
Here, we investigate the contribution of snowmelt during rain-on-snow events. We calibrate a simple snow water equivalent (SWE) accumulation and melt model, later used to estimate the additional contribution of snowmelt to intense precipitation at the Aprica and Pantano stations. Then, through the AM method, we estimate the impact of snowmelt on the IDF curves.
In the next sections we present the dataset adopted, the SWE model, the statistical approach here considered and we present the results obtained.

3.2 Datasets and Methods

3.2.1 Meteorological data

Lombardy meteorological stations network is managed at regional level by ARPA Lombardia, the regional Environment Protection Agency. The monitoring stations provide measurements at sub-hourly time scale of different meteorological variables such as precipitation, temperature, relative humidity, total radiation, wind speed and direction, and in some cases, snow depth.

Here, we use precipitation [mm], temperature [°C] and snow depth [cm] observations measured at Aprica (46.154 N, 10.147 E) and Pantano d'Avio (46.167 N, 10.474 E). Aprica is located Alpine pass between Valtellina and Valcamonica at an altitude of 1180 m asl; Pantano d'Avio (simply Pantano from here on) is placed nearby an artificial lake in Valcamonica at an altitude of 2390 m asl. The selection of these two stations has been mainly driven by the long temporal coverage. In fact, in both sites, we considered 27 years of continuous observations, from 1996 to 2022. For both meteorological stations we considered daily precipitation, temperature, and snow depth measurements to calibrate the snow accumulation and melt model based on the degree-day factor method, classify rain-on-snow days and obtain a daily average estimate of meltwater production. Then, we used the sub-hourly precipitation measurements to obtain intense precipitation events at different durations. Specifically, we focus our attention to sub-daily events, considering the 1 hour, 3 hours, 6 hours, 12 hours and 24 hours durations. The temporal resolution at which the data are provided changes along the considered monitoring period, being 30 minutes from 1996 to 1999 and 10 minutes after 2000. The dataset can be found and freely downloaded from the ARPA Lombardia meteorological data web portal (https://www.arpalombardia.it/Pages/Meteorologia/Richiesta-dati-misurati.aspx.).

3.2.2 Precipitation data correction

In order to estimate the meltwater production concurrently with intense precipitation events, a simple snow water equivalent (SWE) model has been implemented. Obviously, snow accumulation is governed by the intensity of snowfall events. However, Grossi et al. (2017) found that in the two considered monitoring sites, precipitation measurements by rain gauges are generally affected by a systematic underestimation, usually stronger in case of snowfall events. In view of this, we corrected the daily precipitation data by applying a temperature-based correction procedure proposed by Grossi et al. (2017). The corrected precipitation P_c is computed as

$$P_c = (1 + \alpha_s C_s)P \tag{3.1}$$

$$\alpha_s = \begin{cases} 1, & \text{if } T_m < T_l \\ (T_h - T_m)/(T_h - T_l), & \text{if } T_m < T_l < T_l \\ 0, & \text{if } T_m > T_h \end{cases} \tag{3.2}$$

Where P is the measured precipitation, C_s is a correction factor scaled by means of the coefficient α_s, limited between 0 and 1 (Figure 3.1), which is a linear function of the daily average temperature and depends on the minimum threshold value for liquid precipitation T_h and the maximum threshold value for solid precipitation T_l. The values of T_l and T_h were obtained by a statistical analysis of snowfall, rainfall and mixed events and fixed at T_l=0°C and T_h=2°C, a symmetric neighborhood of the center of the mixed events distribution T_s=1°C. The correction factor C_s is calibrated for the specific meteorological station. Specifically, we considered C_s=0.6 for Aprica and C_s=1.05 for Pantano. We note that the higher correction coefficient obtained by Grossi et al. (2017) for Pantano indicates that winter precipitation is

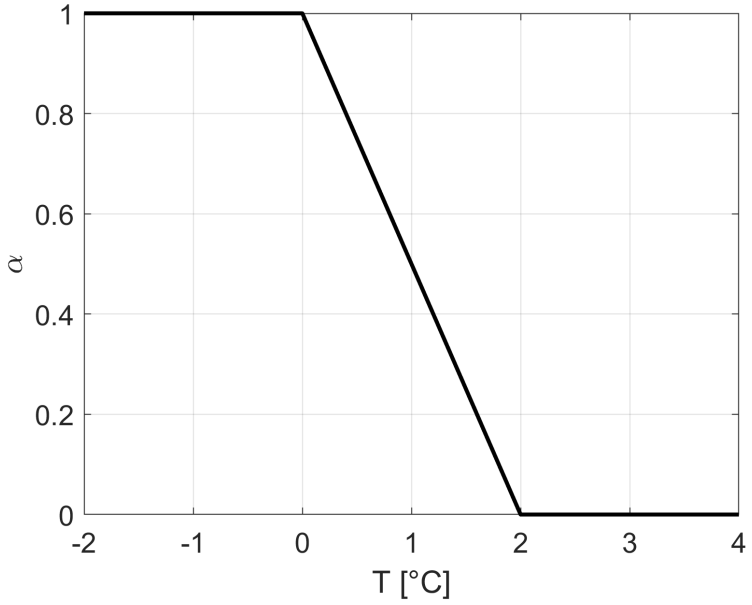

Figure 3.1: Temperature dependent coefficient α_s.

more strongly underestimated than in case of Aprica. In fact, for this specific site they found a 34% underestimation of the mean yearly precipitation. We apply this correction procedure to have a better estimate of the precipitation volume contributing to snow accumulation, without affecting liquid precipitation events.

3.2.3 Snow water equivalent and snow melt model

We used the corrected precipitation data to run a simple SWE model that takes as input, together with precipitation, daily temperature data. The SWE on ground for a certain day i (SWE_i [mm]) can be computed as

$$SWE_i = SWE_{i-1} + A_i - M_i \tag{3.3}$$

Where SWE_{i-1} [mm] is the SWE of the previous day, A_i [mm] and M_i [mm] are, respectively, accumulation and melting occurring on the i-th day. The corrected precipitation contributes completely to snow accumulation when daily average temperature is below the maximum threshold value for solid precipitation T_l=0°C, increasing SWE on ground, and melting is null. As the average temperature overcomes the threshold value of 0°C, snowmelt starts, and M takes positive values. As an alternative to a more accurate calculation of snowmelt based on energy balance (Anderson, 1968, 1976), a simplified estimate can be provided by the degree-day method (Rosa, 1956; Martinec 1960), considering air temperature only. Here we model snowmelt by means of a degree-day approach corrected with respect to the classical formulation based on temperature only in order to consider the contribution of liquid precipitation. Specifically, we computed melting as

$$M = \frac{PT}{80} + k_s T \tag{3.4}$$

Where T is the daily average temperature (°C), P is precipitation (mm) and k_s (mm °C d-1) is

the degree-day factor. The number 80 (°C) is the ratio between the latent heat of melting (333.5 J g-1) and the specific heat of water (4.186 J g-1 °C-1), rounded to the nearest whole number. Typical values of k_s range from 1.6 to 6, varying with snow density, wind speed and elevation, and a value of 2.74 if often used when other information is lacking (NRCS, 2009). Here, we calibrate this parameter through the comparison with SWE estimates obtained from the daily snow depth measurements at the considered sites. This approach takes into consideration both precipitation and temperature contribution to snowmelt. In this regard, in case the daily average temperature is between the threshold values of T_l=0°C and T_h=2°C, we consider that a portion $\alpha_s P$ of such precipitation would contribute to accumulation and the complementary portion $(1-\alpha_s)P$ to snowmelt, where α_s is the same parameter previously presented. Such separation must be taken into account since we run the model with the daily precipitation timeseries corrected with the temperature-based procedure. In this case, we assume that the portion of solid precipitation linearly decreases from 1 to 0 as the average temperature goes from 0°C to 2°C. Finally, when the measured air temperature is larger than T_h=2°C, accumulation is null and all the precipitation contributes to snowmelt. Obviously, the admissible values of M for the i-th day are limited between zero and the sum SWE of the previous day and, if present, the accumulation of the current day.

3.2.4 Snow density models

In order to calibrate the snowmelt degree-day factor model, we compared the modelled SWE with in situ estimates derived from daily snow depth measurements. The SWE (mm) can be estimated as

$$SWE = \frac{HS\rho_s}{\rho_w}10 \tag{3.5}$$

Where HS (cm) is the measured snow depth, ρ_s (kg m^{-3}) is the snow density and ρ_w (kg m^{-3}) is the liquid water density, estimated as 1000 kg m^{-3}. Since there are no continuous snow density measurements at the considered sites we obtain an estimate from empirical relations, in order to estimate the SWE at daily temporal scale. Many authors proposed different formulations to estimate snow density along accumulation and melting season. Here, we consider four different formulations of snow density as function of the day of the year. Specifically, we considered the linear function proposed by Pistocchi (2016), who estimated snow density as

$$\rho_s(DOY) = m_0 + m_1(DOY + 61) \tag{3.6}$$

Where DOY is the day of the year and the parameters m_0 = 200 kg m^{-3} and m1=1 were calibrated by the authors considering 2009-2011 winters in Bolzano. We also considered a quadratic formulation proposed by Guyennon et al. (2019) and recalibrated in chapter 2, estimating the snow density as

$$\rho_s(DOY) = n_0 + n_1(DOY + 61) + n_2(DOY + 61)^2 \tag{3.7}$$

Where the parameters (n_0,n_1,n_2) are equal to (288.9, 0.93, 0.0082) for Guyennon et al. (2019) and
(277, 0.36, 0.0051) from chapter 2.

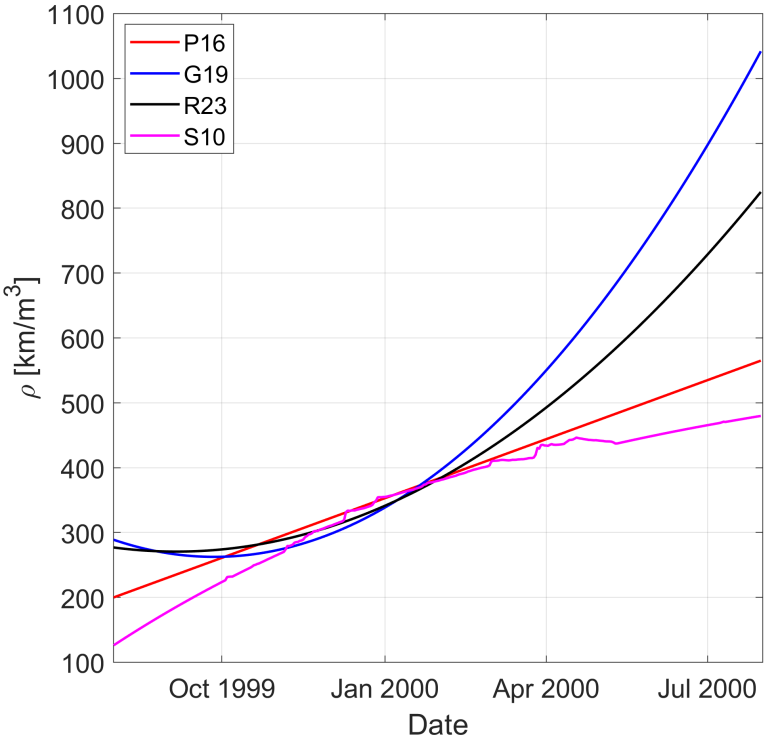

Figure 3.2: Snow density empirical relationships.

Finally, in view of the availability of daily snow depth measurements, we considered an empirical relation that estimates snow density as a function of the DOY and HS (Strum et al., 2010) as

$$\rho_s(Y, DOY) = \rho_0 + (\rho_{MAX} - \rho_0)(1 - e^{k_0 HS(Y,DOY)+k_1 DOY}) \tag{3.8}$$

Where ρ_0=223.7 kg m^{-3} is the base snow density, ρ_{MAX}=597.5 kg m^{-3} is the maximum snow density, HS is the snow depth, Y is the specific year when HS is measured and the two parameters (k_0,k_1) are equal to (-0.0012, -0.0038). Such formulation provides a year-by-year estimate of snow density as it is a function of snow depth measurements. In Figure 3.2 we show the selected snow density formulations.

3.2.5 Statistical analysis

In the frequency analysis of hydrological quantities, annual maxima (AM) approach is the most often adopted. The main reasons are its ease of application and the difficulty in obtaining original timeseries for the oldest measurement stations, for which the information is generally limited to annual maxima. Such approach is theoretically correct and widely used. The first analysis is the proper choice of a probabilistic distribution able to model the annual maxima sample. Here, we consider and compare three cumulative distribution functions (CDF) generally adopted for extreme value analysis: the Gumbel distribution (EV1), the Generalized Extreme Value distribution (GEV) and the log-normal distribution (L-N).

EV1 distribution

The Gumbel (or EV1) belongs to the family of the Extreme Value distributions. The EV1 distribution of a random variable x takes the form

$$P(x) = e^{-e^{-\frac{x-u}{\alpha}}} \tag{3.9}$$

where α is the scale parameter and u the location parameter. The two parameters can be estimated through the mean $\mu(x)$ and the standard deviation $\sigma(x)$ as

$$\begin{aligned} \alpha &= \frac{\sigma(x)}{1.2825}, \\ u &= \mu(x) - 0.450\sigma(x) \end{aligned} \tag{3.10}$$

obtained from the definition of the theoretical moments of the distribution. For the EV1 distribution the skewness is constant ($\gamma \sim 1.14$).

The Generalized Extreme Value distribution

The GEV distribution is a general formulation of the Extreme Value distributions (Jenkinson 1955, 1969). Its CDF $P(x)$ is defined as

$$P(x) = e^{-[1-\frac{x-u}{\alpha}]^{\frac{1}{k}}} \tag{3.11}$$

where α is the scale parameter, u the location parameter and k the shape parameter. The parameter k determines the type of extreme value distribution. For $k < 0$ the GEV represent a Frechet distribution (EV2), for $k < 0$ the Weibull distribution (EV3) and in case of $k = 0$ the Gumbel distribution, previously described. The mean, the variance and the skewness of the GEV are expressed as

$$\begin{aligned} \mu(x) &= u + \frac{\alpha}{k}[1 - \Gamma(1+k)], \quad k > -1 \\ \sigma^2(x) &= (\frac{\alpha}{k})^2[\Gamma(1+2k) - \Gamma^2(1+k)], \quad k > -\frac{1}{2} \\ \gamma &= sign(k)\frac{-\Gamma(1+3k) + 3\Gamma(1+k)\Gamma(1+2k) - 2\Gamma^3 1 + k}{[\Gamma(1+2k) - \Gamma^2(1+k)]^{\frac{3}{2}}}, \quad k > -\frac{1}{3} \end{aligned} \tag{3.12}$$

It can be noticed that the skewness does not depend on α and u, being a function of the parameter k only which can be estimated by estimating γ. Then, it is possible to estimate α and u as

$$\alpha = \sqrt{\frac{k^2\sigma^2}{\Gamma(1+2k) - \Gamma^2(1+k)}} \tag{3.13}$$

The Log-Normal distribution

The log-normal (L-N) distribution is also frequently used in extreme value analysis. It is a two-parameters distribution describing the distribution of the natural logarithm of the variable

x as a normal distribution. The probability density function of the L-N is expressed as

$$p(x) = \frac{1}{x\sqrt{2\pi}\alpha} e^{-\frac{1}{2}[\frac{\ln x - u}{\alpha}]^2} \tag{3.14}$$

where the two parameters are the mean and the standard deviation of the natural logarithm of the variable x estimated as

$$\begin{aligned} \alpha &= \sqrt{\ln(1 + \frac{\sigma^2(x)}{\mu^2(x)})}, \\ u &= \ln \mu(x) - \frac{1}{2} \ln(1 + + \frac{\sigma^2(x)}{\mu^2(x)}) \end{aligned} \tag{3.15}$$

Parameters estimate: L-moments

The parameters of the selected probability distribution can be estimated following different approaches. Here, we use the methods of moments and the L-moments method.
The method of moments widely adopted due to its simplicity. It consists in setting the population moments of the selected probability distribution $P(x)$ with the sample moments and solving the population moment expression for the parameter of interest, as described previously for the EV1 and the L-N. For unbiased estimates of the moments, the sample moments are multiplied by a correction factor (1 for the mean, $\frac{N}{N-1}$ for the variance and $\frac{N^2}{(N-1)(N-2)}$ for the third-order moment). As higher order moments are characterized by higher variance, distributions with parameters depending on lower order moments are more suitable, expecially when the numerosity of the sample is limited.
A more robust methodology to estimate the probability distribution parameters is the use of the L-moments (Hosking, 1990). Being $\{x_1, ..., x_n\}$ and $\{x_{1:n}, ..., x_{n:n}\}$ the ordered sample, the L-moments (and their ratios) are defined as

$$\begin{aligned} L_1 &= E(x), \\ L_2 &= 2w_2 - L_1, \\ L_3 &= 6w_3 - 6w_2 + L_1, \\ L_4 &= 20w_4 - 30w_3 + 12w_2 - L_1, \\ t_3 &= \frac{L_3}{L_3}, \\ t_4 &= \frac{L_4}{L_3} \end{aligned} \tag{3.16}$$

where L_1 is the sample mean, L_2 is a dispersion measurement of the sample, t_3 is the L-skewness and t_4 the L-kurtosis. The parameters w_2, w_3 and w_4 are the estimates of the Probability

Weighted Moments (PWM) and are computed as

$$
\begin{aligned}
w_2 &= \frac{1}{n(n-1)} \sum_{i=2}^{n} (i-1) x_{i:n}, \\
w_3 &= \frac{1}{n(n-1)(n-2)} \sum_{i=3}^{n} (i-1)(i-2) x_{i:n}, \\
w_4 &= \frac{1}{n(n-1)(n-2)(n-3)} \sum_{i=4}^{n} (i-1)(i-2)(i-3) x_{i:n}
\end{aligned}
\tag{3.17}
$$

The L-moments are linear combination of the PWM and can be used to estimate the parameters of the GEV distribution. The location (u), scale (α) and shape (k) parameters of the GEV can be estimated as

$$
\begin{aligned}
k &\sim 7.8590c + 2.9554c^2, \\
c &= \frac{2w_2 - L_1}{3w_3 - L_1} - 0.63093, \\
\alpha &= k \frac{L_2}{\Gamma(1+k)(1-2^{-k}}, \\
u &= L_1 - \frac{\alpha}{k}[1 - \Gamma(1+k)]
\end{aligned}
\tag{3.18}
$$

Here, we estimate the EV1 and L-N distributions parameters according to the method of moments and the GEV parameters according to the L-moments method.

3.2.6 Intensity-Duration-Frequency curves

The Intensity-Duration-Frequency (IDF) curves provide a relationship between precipitation intensity h and its duration d, for a given return period T. Different relationships have been proposed (e.g., Sherman, 1931; Chow, 1962), but the most commonly adopted relationship in Italy is a power low in the form

$$h(d, T) = a(T) d^{n(T)} \tag{3.19}$$

where $a(T)$ and $n(T)$ are the two coefficients varying with the return period. The parameters can be easily computed by least-square fitting the linear relationship, obtained by applying the logarithm to the IDF formulation, defined as

$$Y = n(T)X + Q \tag{3.20}$$

where $Y = \log h(d, T)$,$Q = \log a(T)$ and $X = \log d$. In general, the IDF curves are computed for the return periods of 2, 5, 10, 20, 50, 100, 200, 500 and 1000 years. The data points to be fitted by the linear relationship are the quantiles obtained from the considered probabilistic function expressed in terms of return period $T(x)$

$$T(x) = \frac{1}{1 - P(x)} \tag{3.21}$$

For the calculation of the quantiles we estimated the location (u) and scale (α) parameters we adopted the method of moments for the EV1 and L-N and the L-moments for the GEV

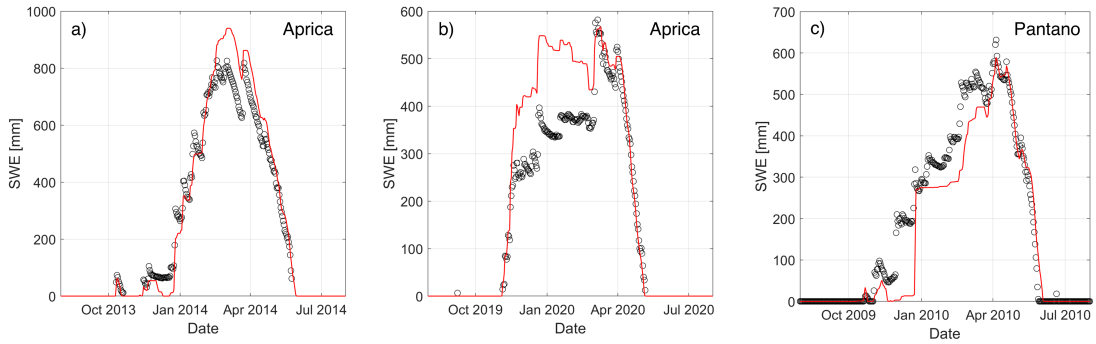

Figure 3.3: Modelled (red) and estimated (black circles) SWE for Aprica (a,b) and Pantano (c) stations in three different hydrological years.

distribution. For the shape parameter k of the GEV we considered an average value of the k values computed for each duration with the L-moments. Here, we compute the IDF curves for Aprica and Pantano locations considering two cases: the measured precipitation (P) and the considered sites (i.e., the classical IDF analysis) and the combined contribution of precipitation and melting (P+M).

3.3 Results and discussion

3.3.1 Calibration of degree-days melting model

After correcting both Aprica and Pantano daily precipitation records according to methodology proposed by Grossi et al. (2017), we implemented a simple accumulation/melt model based on the degree-day melting factor to estimate the SWE on ground. Such model is necessary to calibrate a proper degree-day factor (k_s) to estimate the melting contribution to floods in conjunction with heavy rain events. By minimizing the RMSE between modelled and estimated SWE, we obtained a value of k_s=3.05 mm °C d^{-1}.
In Figure 3.3 we report the modelled (red) and estimated from HS and ρ_s (black cirlces) SWE in three different years for Aprica (a and b) and Pantano (c). Here we considered an average SWE estimated from HS and the proposed ρ_s formulations (estimated SWE from this point). The modelled SWE at the Aprica site for the hydrological year 2013-2014 can fairly describe the estimated SWE on ground variability througout the accumulation and melting season, showing a slow overestimation of the maximum SWE value (Figure 3.3a). For the year 2019-2020 however the model shows a stronger overestimation of the SWE on ground in accumulation (Figure 3.3b). However, the maximum value of SWE is well estimated, as well as the melting season. On the contrary, in the case of Pantano for the hydrological year 2009-2010 (Figure 3.3c), the model seems to underestimate the accumulation of SWE on ground in some periods, capturing the maximum value and the decreasing lamb of the SWE curve for the melting season. Since we are interested in estimating the additional contribution of melting in rainy days, we are more interested in finding a calibrated k_s that allows the model to fit the melting season and properly captures the rate of SWE decrease than accumulation. In view of this, we consider the obtained k_s properly calibrated for our purpose.

3.3.2 Rain-on-snow extreme events and corrected IDF curves

Once the k_s parameter is estimated, it is possible to estimate the additional contribution of snowmelt to liquid precipitation during rain-on-snow events. We used the sub-hourly precipitation data to reconstruct the precipitation timeseries for the durations of 1 h, 3h, 6h, 12h and 24 h (P). Then, we computed the melting contribution solving Equation 3.4 using the reconstructed P for each duration, daily average air temperature and estimated SWE (from HS and ρ_s). Since the second term of Equation 3.4 ($k_s T$) is expressed in mm d^{-1}, we multiply for a reduction coefficient equal to $d/24$ to consider the melting occurring within the considered duration. The estimated melt (M) is then added to the precipitation (P), obtaining the timeseries of conjunct contribution of precipitation and melting (P+M) at both Aprica and Pantano stations.
Figure 3.4 and Figure 3.5 show the extracted maximum precipitation and combined precipitation and melting for each year of observation at the Aprica and Pantano stations. It is possible to notice that, of course, not every value of the series has been affected by the additional melt. The maximum value of P+M for a certain year can be the same of P if rain-on-snow events do not occur for that year or if the occurring rain-on-snow events show lower intensity than a rainfall event. On the other hand, the AM of P+M can be higher than than the AM of P in two cases: 1) the AM of P occurs when snow is present on the ground (i.e., is a ROS event) triggering melting or 2) the AM of P is not a ROS event and another event in the same year, characterized by lower intensity than the AM of P, is a ROS event and, combined with the induced melting, produces a value of P+M higher than the AM of P.

We computed the parameters of the selected probability distributions for each duration, for both P and P+M AM series and for both Aprica and Pantano locations (Table 3.1). With the estimated parameters we computed the quantiles for the return periods $T = 5, 10, 20, 50, 100, 200$ years for both P and P+M and evaluated the increment provided by the melting contribution computing the percentage change (i.e., the ratio between the difference of the P+M and P quantiles and the P quantile). The quantiles computed for Aprica and Pantano are reported in Table 3.2 and Table 3.3. For the Aprica station, we obtained from the quantiles estimated with the GEV distribution an average percentage change of 2.8%, ranging from 0.3% (obtained for a return period T=5 and duration d=1 h) to 10.1%. Similarly, the quantiles obtained using the EV1 distribution exhibit an average percentage increment of 2.1%, ranging from 0.5% and 3.8%. With the L-N distribution the percentage change is smaller, with an average increment of 1.4% and two cases (T=100, 200 years and d=24 h) with a decrease of 0.3% and 0.8%. In general, we found that the contribution of melting increases with the duration and the return period for the GEV and EV1 cases. We found the same behavior in case of L-N distribution, with the exeption of the 24 h quantiles. For the Pantano station, we found that the quantiles of the GEV distribution increased on average of 3% when considering melting, with a decrease of 0.5%, only for the return period of 200 years and duration of 6 hours, and a maximum percentage increase of 9.1%. In case of the EV1 quantiles, the average percentage change is 2.6%, ranging between 1.1% and 5%. For the L-N distribution, the percentage change ranges between -1.4% and 4%, with an average of 1.4%. Also in this case, the meltwater contribution increases with the duration with maximum differences in case of d=24 h. This fact suggests that longer durations (i.e., 1, 2, 3, 4

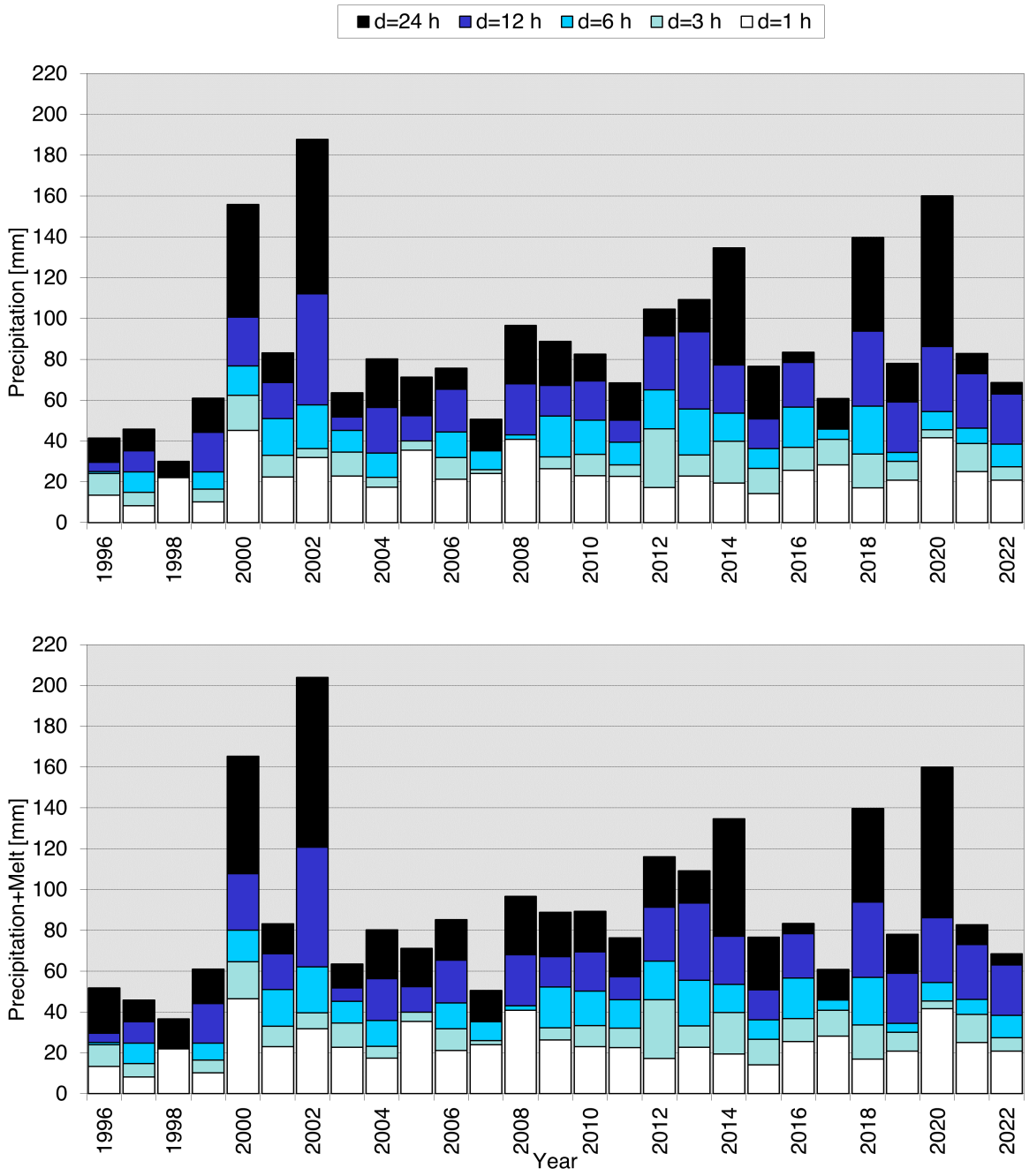

Figure 3.4: Timeseries of the annual maxima of P and P+M for the Aprica station

and 5 days) might present a stronger increase in the quantiles considering melting contribution. For the 24 h duration the average percentage change is of 3.2% for Aprica and 4.1% for Pantano when considering all the selected probability distributions. Without considering the L-N results, which exhibited counterintuitive results, the average percentage increase is 4.5% for Aprica and 5.4% for Pantano. Ranzi (2014, unpublished) found that the contribution of snowmelt to the 48 h duration during the catastrophic event occurred in Adige basin in 1966 (3 and 4 November) ranged between 10% and 20%.

Finally, we computed the parameters a and n of the IDF curves by linear regression of the logarithmic transformation of the quantiles and the durations (Table 3.4) for P and P+M, for

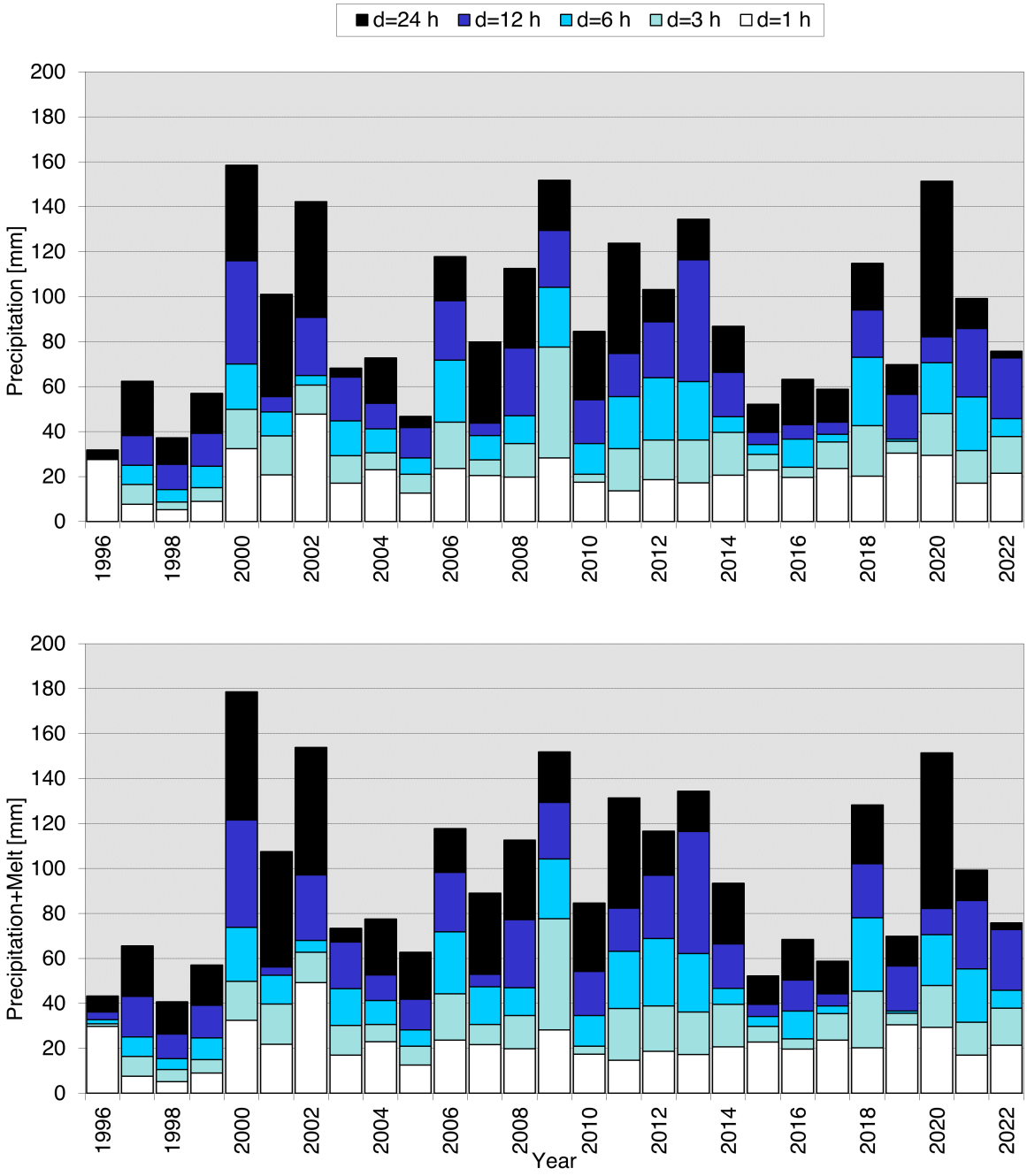

Figure 3.5: Timeseries of the annual maxima of P and P+M for the Pantano station

all the return periods at Aprica and Pantano stations. In Figure 3.6 the IDF obtained from the EV1 are reported as example for both Aprica (a,c) and Pantano (b,d) stations. From the figure it is possible to see the increment in terms of intensity for given duration and frequency (or return period).

3.4 Conclusions and future developments

Snowmelt can enhance flood peak volumes when ROS events occur. We investigated the importance of snow on the ground during intense rainfall events at two locations in Lombardy,

		EV1		LN		GEV		
Station	**d [h]**	**u**	α	**u**	α	**k**	α	**u**
Aprica P	1	19.63	7.02	3.10	0.37	0.01	7.22	19.62
	3	28.75	7.71	3.46	0.29	0.19	9.17	29.41
	6	38.85	10.25	3.76	0.29	0.27	13.20	40.02
	12	54.31	17.59	4.11	0.34	0.22	22.20	55.64
	24	71.03	29.71	4.39	0.41	-0.10	26.96	69.63
Aprica P+M	1	19.65	7.11	3.10	0.37	0.01	7.23	19.61
	3	29.04	7.89	3.47	0.29	0.19	9.26	29.76
	6	39.27	10.57	3.77	0.29	0.25	13.36	40.38
	12	54.71	18.42	4.12	0.35	0.16	22.23	55.65
	24	73.24	30.91	4.43	0.42	-0.15	26.02	71.40
Pantano P	1	17.15	6.65	2.97	0.39	0.12	7.33	17.58
	3	28.12	11.02	3.46	0.39	0.07	11.75	28.51
	6	39.45	15.37	3.80	0.39	0.06	16.90	39.59
	12	54.64	22.04	4.13	0.40	0.06	24.65	54.42
	24	74.54	28.56	4.44	0.39	0.12	34.04	75.12
Pantano P+M	1	17.32	6.81	2.98	0.40	0.12	7.43	17.75
	3	29.00	11.04	3.49	0.39	0.09	11.94	29.47
	6	40.91	15.73	3.84	0.39	0.08	17.72	41.13
	12	57.20	22.14	4.17	0.39	0.03	24.22	56.72
	24	79.15	29.42	4.49	0.38	0.07	33.54	79.03

Table 3.1: Parameters of the selected probability distributions.

Aprica and Pantano d'Avio. We reconstructed the precipitation timeseries at the two locations by correcting the precipitation measurements throughout a temperature based approach aimed in minimizing the measurement error during winter. We used the corrected precipitation data at daily temporal resolution to run a SWE accumulation and melt model based on the degree-day factor. We calibrated the model comparing the outputs with the SWE estimated through snow depth measurements and snow density estimated by four different empirical formulation. We obtained a calibrated k_s equal to 3.05 mm °C d^{-1} and used it to estimate snowmelt in case of ROS events. We reconstructed, from the sub-hourly precipitation measuremens, the cumulated precipitation timeseries (P) for the durations of 1, 3, 6, 12 and 24 hours and computed the associated snowmelt (M) in case of ROS events, obtaining the conjunct timeseries of rainfall and snowmelt (P+M). We applied the annual maxima approach for the extreme value statistical analysis using the GEV, the EV1 and the Log-normal distribution. We found that, on average, snowmelt contributes for about 2.2%. Its influence is larger for longer durations, suggesting the importance of studying also precipitation series cumulated for more than 24 h. For the largest duration (24 h), the average increment to the rainfall volume provided by snowmelt reaches larger percentages, up to 10%, with an average increment of 3.2% at the Aprica station and 4.1% at Pantano. Finally, we provided the IDF curves for the two stations considering both cases of precipitation measurements only and the combination of precipitation and snowmelt. Future developments of this research will include the extension of the statistical analysis to longer durations (e.g., 1, 2, 3, 4, 5 days) and the implementation of an energy balance model for a more accurate estimate of the snowmelt contribution.

		P					P+M				
	T/D	**1**	**3**	**6**	**12**	**24**	**1**	**3**	**6**	**12**	**24**
GEV	**5**	30.3	41.3	56.3	84.1	113.3	30.4	41.8	57.1	85.2	115.3
	10	35.6	46.1	62.2	95.2	137.8	35.8	46.6	63.3	97.5	141.4
	20	40.6	50.1	66.9	104.3	163.1	40.9	50.7	68.3	107.9	169.5
	50	47.0	54.5	71.8	114.1	198.7	47.5	55.1	73.6	119.7	210.8
	100	51.7	57.3	74.7	120.3	227.7	52.5	57.9	76.8	127.5	245.9
	200	56.4	59.8	77.1	125.6	258.7	57.4	60.4	79.5	134.4	284.9
EV1	**5**	30.2	40.3	54.2	80.7	115.6	30.3	40.9	55.1	82.3	119.6
	10	35.4	46.1	61.9	93.9	137.9	35.7	46.8	63.1	96.2	142.8
	20	40.5	51.7	69.3	106.5	159.3	40.8	52.5	70.7	109.4	165.1
	50	47.0	58.9	78.9	122.9	186.9	47.4	59.8	80.5	126.6	193.9
	100	51.9	64.2	86.0	135.2	207.7	52.4	65.3	87.9	139.5	215.5
	200	56.8	69.6	93.1	147.4	228.4	57.3	70.8	95.2	152.3	237.0
LN	**5**	30.7	41.3	55.8	83.7	115.5	30.8	41.8	56.7	85.1	118.1
	10	36.5	47.3	64.0	99.3	139.1	36.7	48.0	65.2	101.3	141.1
	20	42.1	53.0	71.8	114.5	162.2	42.4	53.8	73.2	117.0	163.5
	50	49.5	60.2	81.6	134.2	192.8	49.8	61.1	83.4	137.5	193.0
	100	55.1	65.5	88.9	149.3	216.3	55.5	66.5	90.9	153.2	215.5
	200	60.8	70.8	96.2	164.5	240.3	61.2	71.9	98.5	169.1	238.5

Table 3.2: Quantiles of the selected probability distributions for Aprica.

		P					P+m				
	T/D	**1**	**3**	**6**	**12**	**24**	**1**	**3**	**6**	**12**	**24**
GEV	**5**	27.6	45.2	63.7	89.9	121.7	28.0	46.2	66.1	92.2	126.7
	10	32.0	52.9	75.0	106.6	142.0	32.4	53.8	77.5	109.4	148.6
	20	35.8	59.8	85.2	121.9	159.8	36.4	60.5	87.7	125.4	168.6
	50	40.2	68.3	97.8	140.9	180.5	41.0	68.7	100.1	145.7	192.9
	100	43.2	74.3	106.8	154.5	194.6	44.1	74.3	108.7	160.5	210.1
	200	46.0	80.0	115.3	167.5	207.5	47.0	79.6	116.9	174.9	226.4
EV1	**5**	27.1	44.7	62.5	87.7	117.4	27.5	45.5	64.5	90.4	123.3
	10	32.1	52.9	74.0	104.2	138.8	32.7	53.8	76.3	107.0	145.4
	20	36.9	60.9	85.1	120.1	159.4	37.6	61.8	87.6	123.0	166.5
	50	43.1	71.1	99.4	140.7	186.0	43.9	72.1	102.3	143.6	193.9
	100	47.7	78.8	110.2	156.0	205.9	48.7	79.8	113.3	159.1	214.5
	200	52.4	86.5	120.8	171.4	225.8	53.4	87.4	124.2	174.5	235.0
LN	**5**	28.2	46.0	63.8	89.1	120.4	28.6	46.7	65.9	91.6	125.3
	10	34.5	55.9	77.1	108.0	145.7	35.1	56.4	79.6	110.1	149.7
	20	40.8	65.7	90.1	126.6	170.6	41.5	65.9	93.0	128.2	173.5
	50	49.2	78.8	107.4	151.4	203.6	50.1	78.4	110.7	152.0	204.9
	100	55.7	89.0	120.7	170.6	229.2	56.8	88.1	124.4	170.3	228.8
	200	62.4	99.4	134.4	190.3	255.3	63.7	98.1	138.4	189.0	253.2

Table 3.3: Quantiles of the selected probability distributions for Pantano.

		Aprica P		Aprica P+M		Pantano P		Pantano P+M	
CDF	**T [y]**	**a**	**n**	**a**	**n**	**a**	**n**	**a**	**n**
GEV	**5**	28.10	0.426	28.24	0.431	27.39	0.472	27.79	0.479
	10	31.81	0.435	31.97	0.442	31.85	0.476	32.23	0.485
	20	35.01	0.443	35.15	0.453	35.84	0.479	36.16	0.490
	50	38.68	0.453	38.78	0.470	40.62	0.482	40.78	0.497
	100	41.12	0.461	41.16	0.483	43.93	0.484	43.93	0.502
	200	43.32	0.469	43.27	0.496	47.01	0.486	46.84	0.508
EV1	**5**	27.45	0.430	27.56	0.438	27.08	0.465	27.41	0.475
	10	31.67	0.434	31.83	0.443	32.08	0.466	32.48	0.474
	20	35.71	0.438	35.93	0.447	36.88	0.466	37.35	0.473
	50	40.94	0.441	41.23	0.450	43.09	0.466	43.65	0.472
	100	44.86	0.443	45.20	0.452	47.74	0.466	48.37	0.472
	200	48.77	0.445	49.16	0.454	52.38	0.466	53.08	0.472
L-N	**5**	28.17	0.427	28.31	0.432	28.07	0.460	28.42	0.468
	10	32.75	0.433	33.01	0.437	34.27	0.456	34.72	0.461
	20	37.09	0.438	37.47	0.440	40.40	0.454	40.97	0.455
	50	42.67	0.444	43.22	0.444	48.63	0.451	49.35	0.448
	100	46.84	0.447	47.54	0.447	55.03	0.449	55.86	0.444
	200	51.02	0.451	51.87	0.449	61.62	0.447	62.58	0.440

Table 3.4: Parameters of IDF curves for Aprica and Pantano stations obtained from the regression of the quantiles computed through the GEV, EV1 and L-N distributions.

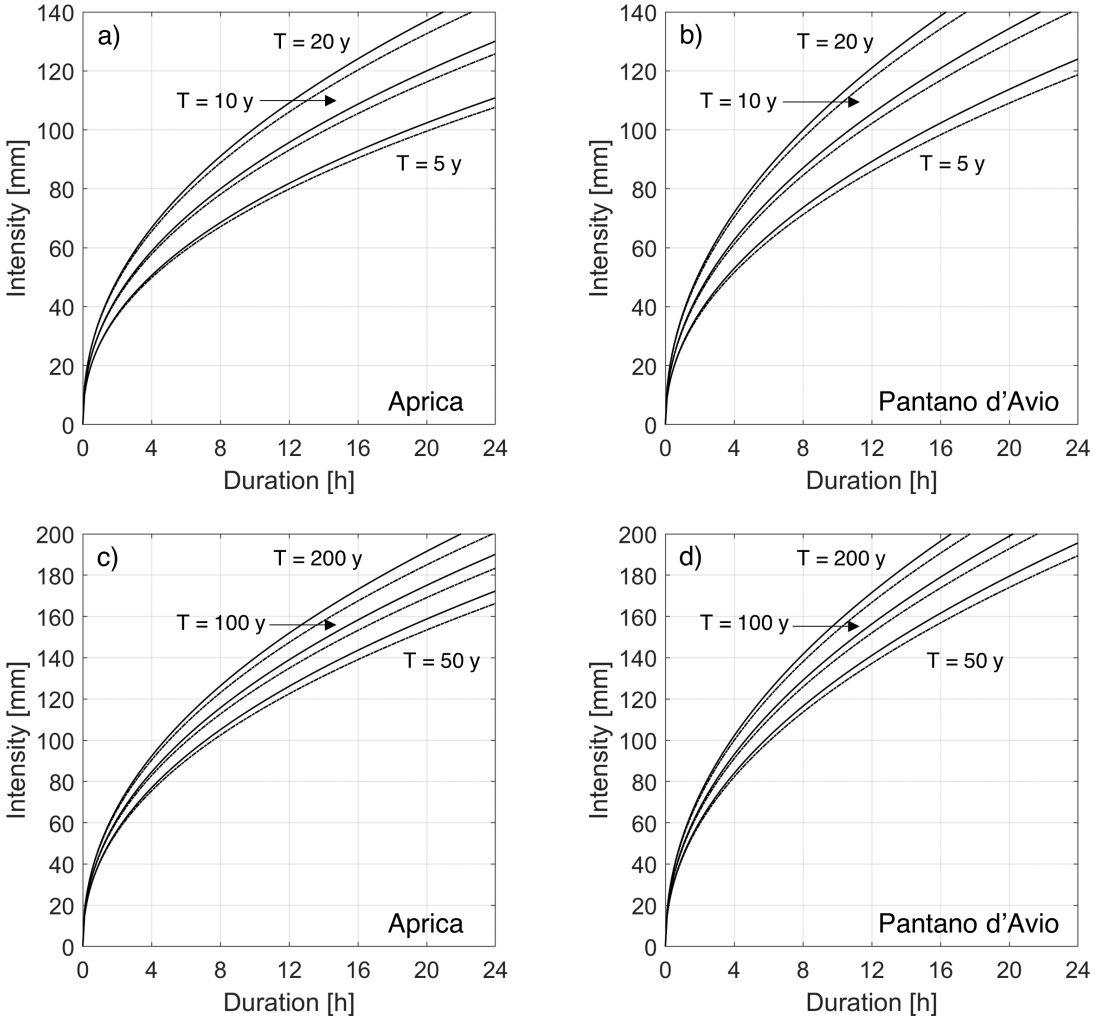

Figure 3.6: IDF curves obtained from the quantiles of the EV1 distribution of the annual maxima of P and P+M for the Aprica and Pantano d'Avio meteorological stations.

Chapter 4

Surface melting over the Greenland ice sheet derived from enhanced resolution passive microwave brightness temperatures (1979–2019)

Ultra Yslandiam per miliaria
fere M est insula dicta
Gronlandia ubi nascuntur
falcones albi et ursi albi.

G. Fiamma,
Cronica universalis

Published:

Colosio, P., Tedesco, M., Ranzi, R., and Fettweis, X. (2021). Surface melting over the Greenland ice sheet derived from enhanced resolution passive microwave brightness temperatures (1979–2019). The Cryosphere, 15(6), 2623-2646.

Abstract

Surface melting is a major component of the Greenland ice sheet surface mass balance, affecting sea level rise through direct runoff and the modulation of ice dynamics and hydrological processes, supraglacially, englacially and subglacially. Passive microwave (PMW) brightness temperature observations are of paramount importance in studying the spatial and temporal evolution of surface melting due to their long temporal coverage (1979-to date) and high temporal resolution (daily). However, a major limitation of PMW datasets has been the relatively coarse spatial resolution, being historically of the order of tens of kilometres. Here, we use a newly released PMW dataset (37 GHz, horizontal polarization) made available through the NASA Making Earth System Data Records for Use in Research Environments (MeASUREs)

program to study the spatiotemporal evolution of surface melting over the Greenland ice sheet at an enhanced spatial resolution of 3.125 km. We assess the outputs of different detection algorithms through data collected by Automatic Weather Stations (AWS) and the outputs of the MAR regional climate model. We found that sporadic melting is well captured using a dynamic algorithm based on the outputs of Microwave Emission Model of Layered Snowpack (MEMLS) model while a fixed threshold of 245K is capable of detecting persistent melt. Our results indicate that, during the reference period 1979 – 2019 (1988 – 2019), surface melting over the ice sheet increased in terms of both duration, up to 4.5 (2.9) days per decade, and extension, up to 6.9% (3.6%) of the entire ice sheet surface extent per decade, according to the MEMLS algorithm. Furthermore, the melting season has started up to 4.0 (2.5) days earlier and ended 7.0 (3.9) days later per decade. We also explored the information content of the enhanced resolution dataset with respect to the one at 25 km and MAR outputs through a semi-variogram approach. We found that the enhanced product is more sensitive to local scale processes, hence confirming the potential of this new enhanced product for monitoring surface melting over Greenland at a higher spatial resolution than the historical products and monitor its impact on sea level rise. This offers the opportunity to improve our understanding of the processes driving melting, to validate modelled melt extent at high resolution and potentially to assimilate this data in climate models.

4.1 Introduction

The Greenland ice sheet is the largest ice mass in the Northern Hemisphere with a glaciated surface area of about 1,800,000 km^2, a thickness up to 3 km, and a stored water volume of about 2,900,000 km^3, enough to rise the mean sea level by about 7.2 m (Aschwanden et al., 2019). In this regard, estimating mass losses from Greenland is crucial for better understanding climate system variability and the contribution of Greenland to current and future sea level rise. According to data from the Gravity Recovery and Climate Experiment (GRACE) satellite mission, which records changes in Earth's gravitational field, Greenland lost mass at an average rate of 278±11 Gt y^{-1} between 2002 and 2016 (IPCC, 2019), contributing to a sea level rise of 7.9 mm per decade. The contribution of the Greenland ice sheet to sea level rise was also accelerating at a rate of 21.9±1 Gt y^{-2} over the period 1992—2010 (Rignot et al., 2011) thus indicating that monitoring the Greenland ice sheet together with the Antarctic ice sheet is crucial to assess the impact of global warming on sea level rise and the global water balance (Kargel et al., 2005; 2014; Le Meur et al., 2018). Mass can be lost through surface (e.g., runoff) and dynamic (e.g., calving) processes with total mass loss roughly split in half between the two (Flowers, 2018). Among the processes influencing the surface mass balance, i.e. difference between accumulation (Frezzotti et al., 2007) and ablation, surface melting plays a crucial role, affecting direct loss through export of surface meltwater to the surrounding oceans and though the feedbacks between supraglacial, englacial and subglacial processes and their influence on ice dynamics (e.g., Fettweis et al., 2005, 2011, 2017; van den Broeke et al., 2016; Alexander et al. 2016). Passive microwave (PMW) brightness temperatures (T_b) are a crucial tool for studying the evolution of surface melting over the Greenland and Antarctica ice sheets (i.e., Jezek et al.,

1993; Steffen et al., 1993; Abdalati et al., 1995; Tedesco et al., 2009; Tedesco, 2009; Fettweis et al., 2011). The PMW-based algorithms are based on the fact that the emission of a layer of dry snow in the microwave region is dominated by volume scattering (e.g., Macelloni et al., 2001); as snow melts, the presence of liquid water within the snowpack increases the imaginary part of the electromagnetic permittivity by several orders of magnitude with respect to dry snow conditions, with the ultimate effect of considerably increasing T_b (Ulaby et al., 1986; Hallikainen et al., 1987) as shown by in situ measurement campaigns (see for instance Cagnati et al., 2004). Because of the large difference between dry and wet snow emissivity, even relatively small amounts of liquid water have a dramatic effect on the T_b values (e.g., Tedesco, 2009), making PMW data extremely suitable for mapping the extent and duration of melting at large spatial scales and high temporal resolution (in view of their insensitivity to atmospheric conditions at the low frequencies of the microwave spectrum). Consequently, PMW data have been widely adopted in melt detection studies and different remote sensing techniques have been proposed in the literature (e.g., Steffen et al., 1993; Abdalati and Steffen, 1995; Joshi et al., 2001; Liu et al., 2005; Aschraft and Long, 2006; Macelloni et al., 2007; Tedesco et al., 2007; Kouki et al., 2019; Tedesco and Fettweis, 2020). The capability of PMW sensors to collect useful data during both day and night and in all-weather conditions allows surface melt mapping at a high temporal resolution (at least twice a day over most of the Earth). PMW T_b records are also among the longest available remote sensing continuous timeseries and an irreplaceable tool in climatological and hydrological studies, complementing in-situ long-term observations where they are absent or too coarse. The trade-off associated with the high temporal resolution of PMW data is the relative coarse spatial resolution (historically on the order of tens of km). This can represent a limiting factor when studying surface melting as a substantial portion of meltwater production and runoff occurs along the margins of the ice sheet, with some of these areas being relatively narrow (of the order of a few tens of kilometers or smaller, depending on the geographic position and time of the year). The use of a product with a finer spatial resolution would allow a more effective mapping of surface melting and would also allow a better comparison between in-situ measured quantities and satellite-derived estimates, reducing uncertainties in the satellite products and allowing for potential improvements to retrieval algorithms. Lastly, finer spatial resolution tools could be helpful, should they be proven effective, in improving mapping of meltwater over ice shelves in Antarctica and improve our understanding of the processes leading to ice shelf collapse or disintegration (e.g. van den Broeke, 2005; Tedesco, 2009). In this paper, we report our results of a study in which surface melting over Greenland is estimated making use of a recently released product developed within the framework of a NASA Making Earth System Data Records for Use in Research Environments (MeASUREs) project (https://nsidc.org/data/nsidc-0630). The product contains daily maps of PMW T_b generated at an enhanced spatial resolution of a few kilometers (depending on frequency, as explained below) between 1979 and 2019. The historical gridding techniques for PMW sensors (Armstrong et al., 1994, updated yearly; Knowles et al., 2000; Knowles et al., 2006) were based on a "drop in the bucket" approach, in which the gridded value was obtained by averaging the T_b data falling within the area defined by a specific pixel. In the case of the enhanced spatial resolution product, the reconstruction algorithm adopted to build the T_b maps makes use of the so-called effective measurement response function (Long

et al., 1998), determined by the antenna gain pattern, which is unique for each sensor and sensor channel. This pattern is used in conjunction with the scan geometry and the integration period, allowing for "weighting" of measurements within a certain area. The approach used to generate the enhanced resolution product, a radiometer version of the Scatterometer Image Reconstruction algorithm, also addresses another issue in the historical PMW dataset, which is the need for meeting the requirements of modern Earth system Data Records or Climate Data Records, most notably in the areas of inter-sensor calibration and consistent processing methods. More details are reported in Section 2.1. We divide the results of our study into two main parts: in the first part, we report the results of the cross-calibration of different PMW sensors over the Greenland ice sheet to assure a consistent and calibrated T_b time series. Specifically, we use the newly developed spatially enhanced PMW product at Ka band (37 GHz), horizontal polarization in view of its sensitivity to the presence of liquid water within the snowpack (Ulaby et al., 1986; Macelloni et al., 2005). We prefer this frequency to the $\sim$ 19 GHz, generally used in the literature as it is less sensitive to liquid water clouds (Fettweis et al., 2011; Mote, 2007), because the T_b at Ka band are distributed at the highest spatial resolution of 3.125 km (Brodzik et al., 2018). The atmospheric effect on 37 GHz T_b is higher than in case 19 GHz at low values of T_b. However, when considering higher values of T_b, the difference of the atmospheric effect between 37 GHz and 19 GHz T_b decreases (Tedesco and Wang, 2009). We, then, focus on assessing whether the noise introduced by the gridding algorithm might limit the application of the enhanced dataset to mapping surface meltwater. Then, we focus our attention on testing and assessing existing approaches to deriving melt from PMW data and propose an update on a recently proposed algorithm in which meltwater is detected when T_b exceeds a threshold computed using the outputs of an electromagnetic model (Tedesco, 2009). We compare results from these algorithms with estimates of surface melting obtained from data collected by automatic weather stations (AWS) in terms of melting timing and with the outputs of the regional climate model Modèle Atmosphérique Régional (MAR; Fettweis et al., 2017) in terms of melting timing and extent. Lastly, we focus on the analysis of melting patterns and trends over study period and investigate the information content in the enhanced resolution dataset through a semi-variogram analysis.

4.2 Datasets and Methods

4.2.1 Enhanced resolution passive microwave data

We use Ka band (37 GHz), horizontal polarization T_b data produced within the framework of a NASA MeASUREs project and distributed at the spatial resolution of 3.125 km (Brodzik et al., 2018) over the Northern hemisphere. Specifically, we use data collected by the Scanning Multichannel Microwave Radiometer (SMMR) SMMR-Nimbus 7, the special sensor microwave/imager (SSM/I) SSM/I-F08, SSMI/-F11, SSM/I-F13 and the special sensor microwave imager/-sounder SSMI/S-F17 (Table 4.1) because of its higher orbit stability (http://www.remss.com/support/crossing-times/). Currently, the product time series begins in 1979 and ends in 2019. Data are provided twice a day, as morning and evening passes. Beginning and ending acquisition times for the morning and evening passes are contained within the product's metadata, together with other

information. More information can be found at https://nsidc.org/data/nsidc-0630/versions/1. Historical gridding techniques for PMW spaceborne datasets (Armstrong et al., 1994, updated yearly; Knowles et al., 2000; Knowles et al., 2006) are relatively simplistic and were produced on grids (Brodzik and Knowles, 2002; Brodzik et al., 2012) that are not easily accommodated in modern software packages. Specifically, the coarse resolution gridding methodology is based on a simple "drop-in-the-bucket" average, i.e. all the measurements within a given time falling into a specific pixel are averaged. In the reconstruction algorithm used for the enhanced T_b, the so-called effective measurement response function, determined by the antenna gain pattern and being unique for each sensor and sensor channel, is used in conjunction with the scan geometry and the integration period. The gridding approach uses the Backus-Gilbert technique (Backus and Gilbert, 1967; 1968), a general method for inverting integral equations, which has been applied for solving sampled signal reconstruction problems (Caccin et al., 1992; Stogryn, 1978; Poe, 1990) for spatially interpolating and smoothing data to match the resolution between different channels (Robinson et al., 1992), and improving the spatial resolution of surface T_b fields (Farrar and Smith, 1992; Long and Daum, 1998). More information about the product can be found at https://nsidc.org/data/nsidc-0630. An example of T_b maps at 37 GHz, horizontal polarization, in the case of both the coarse and enhanced resolution products over Greenland on 16 July 2001 is reported in Figure 4.1. The higher detail captured by the enhanced spatial resolution is clearly visible, especially along the ice sheet edges, where melting generally occurs at the beginning of the season and lasts for the remaining part of the summer. Figure 4.2 shows an example of time series of both coarse and enhanced PMW T_b (again at 37GHz, horizontal polarization) for the pixel containing the Swiss Camp station. From the figure we observe that the two timeseries are highly consistent with each other, with a mean difference of 0.895 K and standard deviation of 4.89 K, indicating that the potential noise introduced by the enhancement process is not a major issue. Yet, differences do exist, as in the case of 3 April 2012 (DOY 93), when the enhanced product suggests the presence of melting while the coarse product does not. This is likely due to the different spatial resolution between the two products, as we discuss in the following sections and shows the added value of using the 37 GHz frequency in detecting small scale features of the melting process. To compare our results with precedent PMW surface melting products, we perform our calculations also to the widely used PMW dataset by Mote (2014). The dataset consists in a daily melt maps product obtained from 37 GHz T_b from SMMR, SSM/I and SSMI/S available on a 25 km grid. This comparison enables us to see the advantages in using the enhanced resolution product with respect to a coarser resolution surface melt product. The dataset is generated using a dynamically changing threshold (Mote, 2007) obtained simulating the T_b change for every grid cell, each year, through a microwave emission model (Mote, 2014). The dataset covers the temporal window 1979 – 2012 and is available at the NSIDC website (https://nsidc.org/data/NSIDC-0533/versions/1).

4.2.2 Greenland air temperature data

In order to assess the results obtained from PMW data, we use in-situ data collected by AWS distributed over the Greenland Ice sheet. In the absence of direct observations of melting, we use air temperature (3 m above the surface) to extrapolate instances when liquid water is

	SMMR	SSM/I(F08)	SSM/I(F11)	SSM/I(F13)	SSMI/S(F17)
Platform	NIMBUS-7	DMSP-F08	DMSP-F11	DMSP-F13	DMSP-F17
Temporal coverage	26/10/1978-20/08/1987	09/07/1987-30/12/1991	03/12/1991-30/09/1995	03/05/1995-01/04/2009	04/11/2006-operating
Frequency (GHz)	37	37	37	37	37
Instantaneous Field of View (IFOV) [km^2]	27*18	37*28	37*28	37*28	37*28
Incidence Angle	50.2°	53.1°	53.1°	53.1°	53.1°
Swath width [km]	780	1400	1400	1400	1700
Data acquisition	Alternate days	Daily	Daily	Daily	Daily
Asc. Equator Crossing Time	24:00	18:17	18:25	17:43	18:33
Desc. Equator Crossing Time	12:00	06:10	05:00	05:51	07:08

Table 4.1: Characteristics of the PMW sensors used for this work. LST denotes local solar time.

present, following the procedure adopted by Tedesco (2009) for Antarctica. Specifically, we use data recorded by stations of the Greenland Climate Network (GC-Net; Steffen et al., 1996). The AWSs provide continuous measurements of air temperature, wind speed, wind direction, humidity, pressure and other parameters. We focus on air temperature data collected every hour by 17 selected stations reported in Table 5.2. We considered a validation period from 2000 (when all the considered AWS were in operation) to 2016 and used daily averaged values. More information about the GC-Net dataset can be found at http://cires1.colorado.edu/steffen/gcnet/.

4.2.3 The MAR model

We assess the enhanced PMW-based surface melt maps with the outputs of the regional climate model Modèle Atmosphérique Régional (MAR, e.g., Alexander et al., 2014; Fettweis et al., 2013; Fettweis et al., 2017; Tedesco et al., 2013). MAR is a modular atmospheric model that uses the sigma-vertical coordinate to simulate airflow over complex terrain and the soil ice snow vegetation atmosphere transfer scheme (e.g., De Ridder and Gallée, 1998) as the surface model. MAR outputs have been assessed over Greenland (e.g., Fettweis et al., 2005; Fettweis et al., 2017; Alexander et al., 2014). The snow model in MAR, which is based on the CROCUS model of Brun et al. (1992), calculates albedo for snow and ice as a function of snow grain properties, which in turn depend on energy and mass fluxes within the snowpack. Lateral and lower boundary conditions of the atmosphere are prescribed from reanalysis datasets. Sea-surface temperature and sea-ice cover are prescribed using the same reanalysis data. The atmospheric model within MAR interacts dynamically with the surface model. In this study, we use the output from MAR version v3.11.2 characterized by an enhanced computational efficiency and improved snow model parameters (Fettweis et al., 2017; Delhasse et al., 2020). The model is

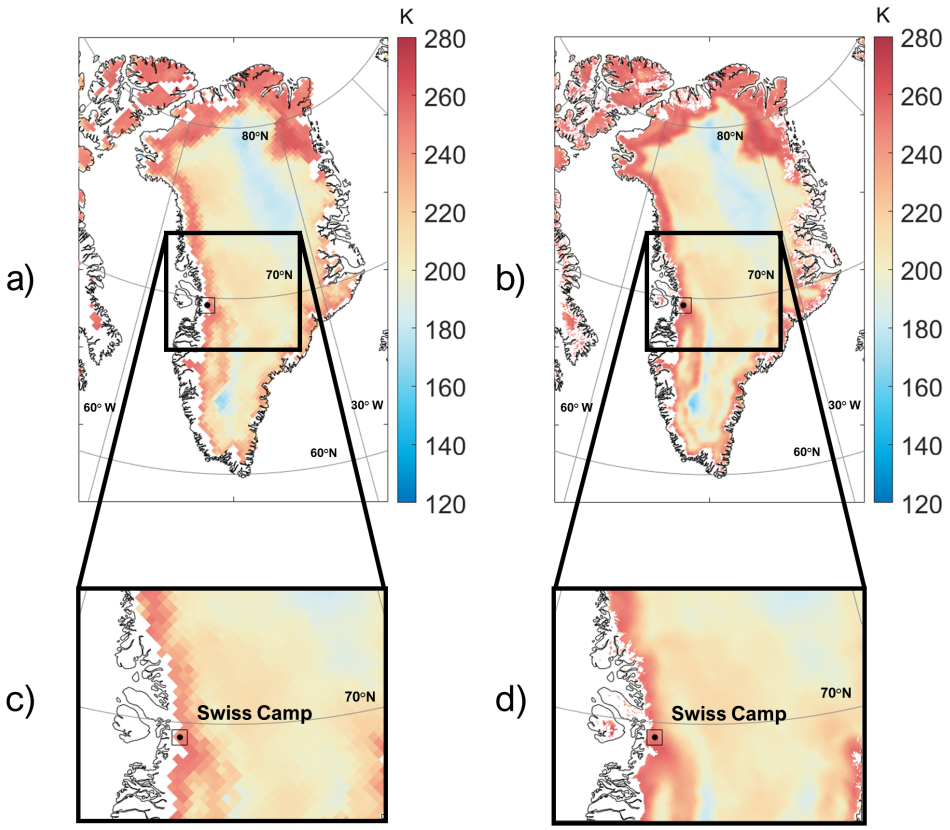

Figure 4.1: Maps of PMW T_b at 37 GHz, horizontal polarization, acquired over Greenland on 16 July 2001 with the (a) coarse (25 km) and (b) enhanced (3.125 km) resolution products. Panels (c) and (d) refer to the area highlighted in the square in panels (a) and (b).

forced at the boundaries using ERA5 reanalysis (Hersbach et al., 2020), the newest generation of global atmospheric reanalysis data that superseded ERA-Interim (Dee et al., 2011), and output is produced at a horizontal spatial resolution of 6 km. In order to compare output from MAR with estimates of melt extent obtained from PMW data, we average the liquid water content (LWC) simulated by MAR along the first 5 cm and 1 m from the surface of the vertical profile of the snowpack, following Fettweis et al. (2007).

4.2.4 Melt detection algorithms

Generally speaking, melt detection algorithms can be divided into threshold-based and edge-detection algorithms (e.g., Liu et al., 2005; Joshi et al., 2001; Steiner and Tedesco, 2014). Here we focus on threshold-based algorithms, detecting melting when T_b values (or their combination) exceed a defined threshold, computed in different ways depending on the algorithm. For example, Steffen et al. (1993) used the normalized gradient ratio $GR = (T_b^{19H} - T_b^{37H})/(T_b^{37H} + T_b^{19H})$ to detect wet pixels with a threshold value computed based on in-situ measurements. This method was later updated by Abdalati and Steffen (1995) who introduced the cross-polarized gradient ratio $XPGR = (T_b^{19H} - T_b^{37V})/(T_b^{37H} + T_b^{19V})$, where the Ka-band component of the

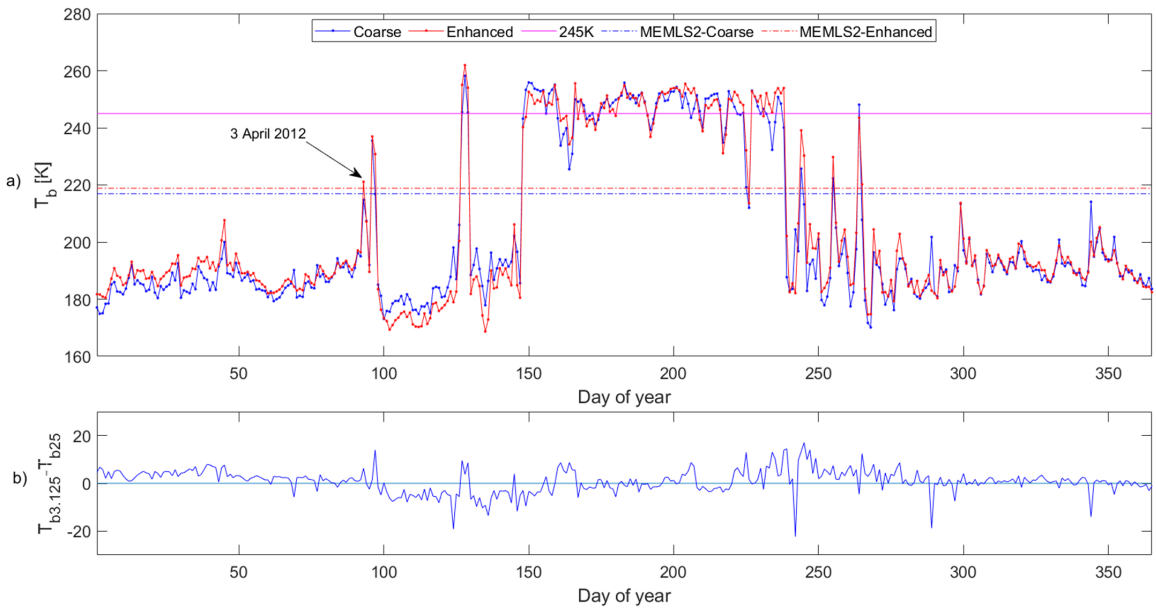

Figure 4.2: (a) Time series of T_b at 37 GHz, horizontal polarization, for the year 2012 for the pixel containing the Swiss Camp site in the case of the coarse (blue) and enhanced (red) products. Threshold values, shown as horizontal lines, are obtained from two approaches considered in this study: 245 K and MEMLS. (b) The difference between the 3.125 km and the 25 km Tb time series for the same pixel (mean of 0.895 K and standard deviation of 4.89 K).

Station	**Latitude**	**Longitude**	**Elevation [m a.s.l.]**
Swiss Camp	69° 34' 06" N	49° 18' 57" W	1149
Crowford Pt. 1	69° 52' 47" N	46° 59' 12" W	2022
NASA-U	73° 50' 31" N	49° 29' 54" W	2369
GITS	77° 08' 16" N,	61° 02' 28" W	1887
Humboldt	78° 31' 36" N	56° 49' 50" W	1995
Summit	72° 34' 47" N	38° 30' 16" W	3254
TUNU-N	78° 01' 0" N	33° 59' 38" W	2113
DYE-2	66° 28' 48" N	46° 16' 44" W	2165
JAR-1	69° 29' 54" N	49° 40' 54" W	962
Saddle	66° 00' 02" N	44° 30' 05" W	2559
South Dome	63° 08' 56" N	44° 49' 00" W	2922
NASA-E	75° 00' 00" N	29° 59' 59" W	2631
Crowford Pt. 2	69° 54' 48" N	46° 51' 17" W	1990
NASA-SE	66° 28' 47" N	42°30' 00" W	2425
KAR	69° 41' 58" N	33° 00' 21" W	2579
JAR-2	69º 25' 12" N	50º 03' 27" W	568
KULU	65° 45' 30" N	39° 36' 06" W	878

Table 4.2: Locations of the automatic weather stations of the Greenland Climate Network (GC-Net) sites used to validate the results in this study

algorithm was switched from horizontally to vertically polarized. Aschraft and Long (2006) proposed a threshold based on dry (winter) and wet snow T_b as $T_c = \alpha M + (1 - \alpha)T_{wet}$ where M is the average of winter T_b (January and February), T_{wet} fixed as 273 K and T_c indicates the

threshold value (we keep the same notation in the following). The mixing coefficient α=0.47 was derived considering LWC=1% in the first 4.7 cm of snowpack. Similarly, a method based on a fixed threshold (set to 245 K and derived from the outputs of electromagnetic model) above which melting is assumed to be occurring was proposed in (Tedesco et al., 2007). Several other studies have been detecting melting when T_b values exceed the mean winter value plus an additional value ΔT_b ($M + \Delta T_b$ approaches) associated with the insurgence of liquid water within the snowpack:

$$T_c = M + \Delta T_b \tag{4.1}$$

Torinesi et al. (2003) proposed a value of $\Delta T_b = N\sigma$ with M and σ (standard deviation of the timeseries) varying in space (specific pixel) and time (specific year) but fixed N=3 from the analysis of weather station temperature data. Zwally and Fiegles (1994) used a fixed value of ΔT_b=30 K. Tedesco (2009) proposed an alternative approach based on the outputs of the Microwave Emission Model of Layered Snowpack (MEMLS) electromagnetic model (Weisman and Matzler, 1999). In this case, an ensemble of outputs is generated by MEMLS model by varying the inputs (e.g., correlation length, LWC, snow density, etc.). These outputs are, then, used to build a linear regression model for the ΔT_b that is a function of the winter T_b value as follows:

$$\Delta T_b = \varphi M + \omega \tag{4.2}$$

with the values of the coefficients obtained from the linear regression. This is done to account for the increment related to the presence of LWC within the snowpack as a function of the snow properties: a fixed increase would correspond to different values of LWC, potentially making the mapping of the wet snow areas inconsistent in terms of LWC values. For example: a snowpack with small grain size will require a relatively larger amount of LWC with respect to a snowpack with larger grain size for the T_b values to increase by 30 K. Or, from a complementary point of view, an increase of 30 K due to presence of liquid water in the case of a snowpack with relatively coarse grains will correspond to a lower value of LWC than an increase occurring in a snowpack with smaller grain size. In summary, the adoption of this approach provides consistency in terms of the minimum LWC that is detected by the algorithm. Building on Tedesco (2009), we considered the LWC value of 0.2%. The coefficients are φ = -0.52 and ω = 128 K (R^2=0.92). The T_b threshold value computed in this case can, therefore, be written as follows:

$$T_c = M + \varphi M + \omega = (1 + \varphi)M + \omega = \gamma M + \omega \tag{4.3}$$

where (γ, ω) assume the values of 0.48 and 128 K.

Here, we focus five approaches: the $M + \Delta T_b$ approach choosing ΔT_b equal to 30K and, to test the sensitivity to Zwally and Fiegles (1994), 35K and 40K (M+30, M+35 and M+40 from here on), the algorithm based on MEMLS in case of LWC=0.2% (referred simply as MEMLS from here on for brevity) and the 245 K fixed threshold (245K from here on). We selected $M + \Delta T_b$ and MEMLS due to their higher accuracy in detecting both sporadic and persistent melting with respect to the other approaches presented above, i.e. Torinesi et al. (2003) and Ashcraft and Long (2006), proved in previous studies (Tedesco, 2009). We selected also the 245K to test a more conservative approach aimed to detect persistent melting only. In the following sections,

we report the results of two algorithms, namely the one using a fixed threshold of 245 K and the one based on MEMLS.

4.2.5 Inter-sensor calibration

In view of the novelty of this PMW dataset introduced by the enhancement in spatial resolution thanks to the improvement of the gridding technique, we first focus on the cross-calibration of the data acquired by the different sensors. This initial processing step aims to account for biases and differences associated with swath width, view angle, altitude and Local-Time-Of-Day as well as the specific intrinsic differences associated with each sensor on the different platforms (Table 4.1). Several approaches have been proposed in the literature to address this issue for the historical, coarser spatial resolution gridded datasets. For example, Jezek et al. (1993) compared SMMR and SSM/I over the Antarctic ice sheet for K and Ka bands ($\sim$ 19 GHz and $\sim$ 37 GHz) for both horizontal and vertical polarizations. Steffen et al. (1993) proposed an approach focusing over Greenland for the K-band; Abdalati et al. (1995) derived relations between SSM/I observations for the F08 and F11 platforms over Antarctica and Greenland for 19.35 GHz, 22.2 GHz and 37 GHz. Dai et al. (2015) intercalibrated SMMR, SSM/I (F08 and F13) and SSMI/S (F17) over snow covered pixels in China and SMMR, SSM/I and AMSR-E over the whole Earth surface sampling hot and cold pixels. Given the novelty of the T_b products used here and the absence of specific intercalibration of data collected from different platforms for this product, we developed an ad-hoc intercalibration for the enhanced PMW dataset. Following Stroeve et al. (1998), we perform the intercalibration using only data collected over the Greenland ice sheet. We perform a linear regression between the data acquired by two sensors over the Greenland ice sheet and calculate the slope (m) and intercept (q) of the linear regression

$$y = mx + q \tag{4.4}$$

In Equation 3.4 x and y represent the T_b values from coincident data from the two overlapping satellite products. We consider two approaches to compute the m and q values in Equation 3.4. In the first method we compute the weighted average of the daily slope and intercept values from the regression of daily data. Considering n days, for every i-th day we first compute m_i, q_i and the coefficient of determination for the linear regression of Equation 3.4 (R_i^2), and then we average them according to Equation 4.5 and Equation 4.6

$$m = \frac{\sum_{i=1}^{n} m_i R_i^2}{\sum_{i=1}^{n} R_i^2} \tag{4.5}$$

$$q = \frac{\sum_{i=1}^{n} q_i R_i^2}{\sum_{i=1}^{n} R_i^2} \tag{4.6}$$

This choice assigns higher values to the weights obtained from pairs of data with higher correlation. In the second method, we consider all values for all days when data from both platforms are available and then evaluate m and q through a linear regression fitting procedure based on least-square fitting. Using the estimated values of m and q, we then correct the values for one of the sensors by applying Equation 3.4 to the T_b values of one sensor (x, e.g. SMMR) to obtain new corrected T_b values (y). We perform an additional comparison using the average difference between the T_b values and evaluating the matching between histograms of the overlapping data (Dai et al., 2015) by means of the Nash-Sutcliffe Efficiency (NSE) coefficient (Nash and Sutcliffe, 1970), defined as:

$$NSE = 1 - \frac{\sum(h_i(T_b^A) - h_i(T_b^B))^2}{\sum(\overline{h}_i(T_b^B) - h_i(T_b^B))^2} \tag{4.7}$$

where h_i is the absolute frequency of the i-th value of T_b of the two sensors (A and B) considered. The NSE is usually applied in calibration/validation procedures to assess the matching between measured and modelled quantities, as in Subsection 4.2. After the application of linear relations found using Equation 3.4 through 4.6, in order to quantitatively assess the impacts of the intercalibration on T_b values, we computed the absolute difference between the values of the histograms of the T_b obtained as:

$$D_i = |h_i(T_b^A) - h_i(T_b^B)| \tag{4.8}$$

where D_i is the absolute difference between the two histograms A and B for the i-th value of T_b. Then, we sum the differences over the total number of pixels and compute the relative variation as follows:

$$d = \frac{D_{original} - D_{corrected}}{D_{original}} \tag{4.9}$$

where $D_{original}$ and $D_{corrected}$ are, respectively, the summations of D_i before and after the calibration. The relative variation d can range from $-\infty$, indicating worsening in matching of the histograms, to 1, indicating a perfect matching of the histograms after the intercalibration.

4.2.6 Spatial autocorrelation: the variogram analysis

Variogram analysis is generally adopted in geostatistical analyses to evaluate autocorrelation of spatial data (Delhomme, 1978; Edward et al., 1989) with variograms being characterized by three parameters: the sill, the range and the nugget effect. The sill is the variance value at which the variogram becomes flat. The range is the distance at which the variogram reaches the sill. Beyond this value, the data are no longer autocorrelated. The nugget effect is the variance value at null distance, theoretically zero and resulting from measurement errors or highly localized variability. We computed the empirical variogram as

$$\gamma(\delta) = \frac{1}{2N(\delta)} \sum_{i,j \in N(\delta)} (x_i - x_j)^2 \tag{4.10}$$

where γ is the semi-variance, $N(\delta)$ is the number of pair measurements (i, j) spaced by distance δ and x_i and x_j are the values of the i-th and j-th measured variable. Generally, the semi-

variance γ increases as the distance δ increases according to the principle that close events are more likely to be correlated than distant events. The experimental variogram is the graphical representation of the semi-variance γ as a function of the distance δ. Finally, the experimental variogram is fitted with a function (here we use a spherical function) to compute the sill, the range and the nugget effect.

4.3 Results and discussion

4.3.1 Inter-sensor calibration of enhanced resolution passive microwave data

At first, we show the results obtained for the inter-sensor calibration of the selected satellite constellation. The overlapping periods for the different sensors are the following: SMMR and SSM/I-F08 overlap between 9 July 1987 and 20 August 1987 for a total of 22 days (one every two days as sensed by SMMR sensor); F08 and F11 overlap between 3 December 1991 and 18 December 1991 for a total of 16 days, F11 and F13 overlap between 3 May 1995 and 30 September 1995 for a total of 76 days; and F13 and F17 overlap for the period 1 March 2008 – 10 December 2008 for a total of 71 days. In Figure 4.3 we show the scatter plots of the data used for the linear regression for Greenland for both evening and morning passes for the SMMR and SSM/I-F08 sensors, reporting values of m, q and R_2. We point out that the overlap between SMMR and SSM/I-F08 data occurs in the months of July and August. During these months, the differences between acquisition times (Table 5.2) might lead to biases and errors associated with snow conditions (e.g., wet vs. dry). Specifically, we expect larger errors at the beginning of the melting season when snow undergoes thawing/refreezing cycles during the day, potentially having frozen snow (low values of T_b) early in the morning and late at night (SMMR ascending and SSMI/-F08 descending passes) and presence of liquid water (high values of T_b) during the day. We report in Table 4.3 average values of the difference between pairs of T_b data and values of the NSE coefficient for the histograms of the same pairs. In Table 4.4 we report the values for slope and intercept obtained from the linear regression analysis of enhanced PMW T_b (37 GHz, H-pol.) over Greenland for SMMR vs. SSM/I-F08, F08 vs. F11, F11 vs. F13 and F13 vs. F17, together with the R_2 values and values of d computed according to Equation 4.6. In the case of SSM/I and SSMI/S, R_2 values are higher, mostly around 0.98. In Figure 4.4 we also show examples of histograms in the case of the SMMR and SSM/I F08 sensors. Large differences are obtained in the case of the SMMR and SSM/I-F08, for both evening and morning passes, likely because of the difference in overpass time and the presence/absence of melting in some of the scenes observed by one sensor but not present in the other (Table 4.3). On the other hand, in the case of the SSM/I and SSMI/S sensors, the average difference is close to 0 K (with the exception of the F-08 and F-11 satellites showing an average difference slightly larger than 1 K, consistent with previous results obtained by Abdalati et al. (1995) in the case of the 25 km resolution data) together with NSE values extremely close to 1 (Table 4.3). Still in the case of SMMR and SSM/I-F08, the higher average difference (ranging between -3.4 K to -4.3 K) and the relatively lower NSE values (ranging between 0.89 and 0.96) show that these sensors show the largest bias. Lastly, we only applied the correction to SMMR and we did not apply the linear regression to the SSM/I F08 – SSM/I F11, SSM/I F11 – SSM/I F13, SSM/I F13

– SSMI/S F17 datasets as, in this case, the linear correction worsened the agreement between the two sets of measurements. We applied the correction coefficients obtained with the second method according to the higher relative improvement for the evening pass.

Sensors	**SMMRvs.F08**		**F08vs.F11**		**F11vs.F13**		**F13vs.F17**	
	Eve.	**Mor.**	**Eve.**	**Mor.**	**Eve.**	**Mor.**	**Eve.**	**Mor.**
NSE	0.898	0.936	0.999	0.999	0.999	0.999	0.997	0.997
Average difference [K]	-4.27	-3.43	0.50	0.24	-0.49	0.02	0.17	0.52

Table 4.3: Average enhanced-resolution T_b differences at 37 GHz, horizontal polarization, for the different PMW sensors and NSE coefficient computed for the histograms of T_b.

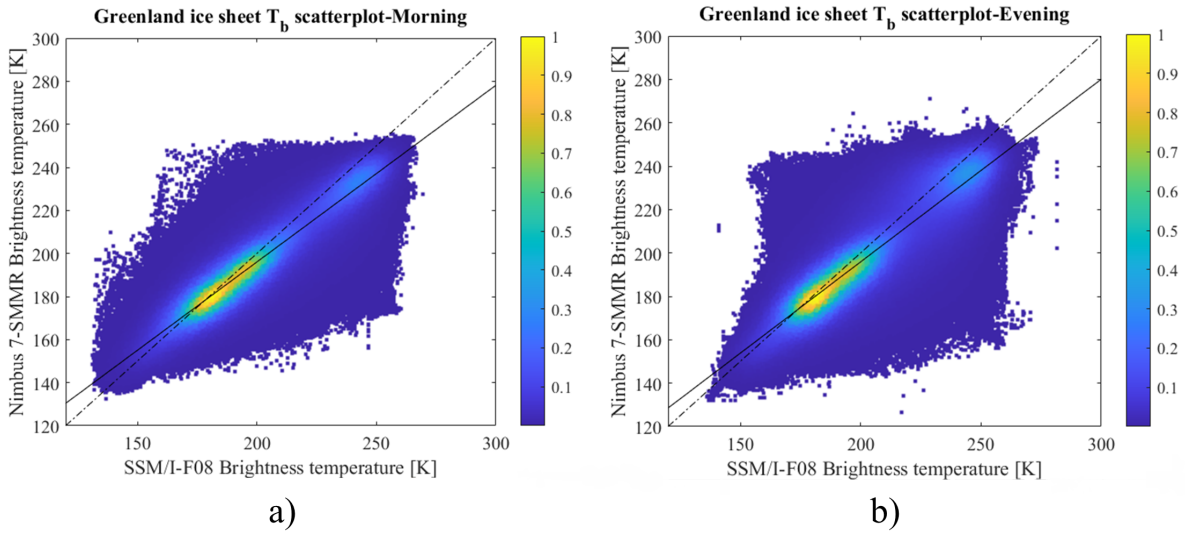

Figure 4.3: Density scatterplots of SMMR and SSM/I-F08 T_b data sensed during the overlap period (9 July–20 August 1987) of the two sensors over the Greenland ice sheet for (a) morning and (b) evening passes. The solid black lines show the linear fitting, and the dashed black lines show the 1 : 1 line. The color palette indicates the relative frequency.

4.3.2 Assessment of melt detection algorithms

In order to assess the capability of the selected algorithms, we compare the outputs obtained by PMW data with in situ air temperature daily averaged from AWS as an index of surface melting (Braithwaite and Oelsen, 1989) and with the liquid water content simulated by the regional climate model MAR. We first evaluate performances at local scale (at the specific locations of the selected AWS), comparing the number and the concomitance of melting days according to PMW and the ground truth reference. Then, according to the results obtained, we focus on MEMLS and 245K algorithms to evaluate at ice sheet scale the capability of the two approaches in describing the surface melt extent.

Greenland SMMR vs. SSM/I-F08							
X=F08	m_1	m_2	q_1	q_2	R_1^2	d_1	d_2
Morning	0.818	0.821	32.387	31.856	0.88	0.69	0.46
Evening	0.849	0.842	26.027	27.511	0.81	0.12	0.33
X=SMMR	m_1	m_2	q_1	q_2	R_1^2	d_1	d_2
Morning	1.075	1.0722	-11.140	-10.581	0.88	0.56	0.52
Evening	0.964	0.9653	11.424	11.123	0.81	0.09	0.12
Greenland F08 vs. F11							
X=F11	m_1	m_2	q_1	q_2	R_1^2	d_1	d_2
Morning	0.991	0.989	2.041	2.537	0.98	0.31	-2.91
Evening	0.998	1.002	0.979	-0.010	0.98	0.25	0.31
X=F08	m_1	m_2	q_1	q_2	R_1^2	d_1	d_2
Morning	0.987	0.995	2.230	0.528	0.98	0.10	0.26
Evening	0.980	0.980	3.332	3.711	0.98	0.08	0.11
Greenland F11 vs. F13							
X=F13	m_1	m_2	q_1	q_2	R_1^2	d_1	d_2
Morning	0.996	1.001	2.328	-0.262	0.98	0.11	0.14
Evening	0.981	0.985	3.831	0.185	0.99	-4.82	-4.98
X=F11	m_1	m_2	q_1	q_2	R_1^2	d_1	d_2
Morning	0.962	0.977	8.322	4.482	0.98	-1.73	-0.32
Evening	0.998	1.002	0.934	0.185	0.99	0.10	0.28
Greenland F13 vs. F17							
X=F17	m_1	m_2	q_1	q_2	R_1^2	d_1	d_2
Morning	1.019	1.029	-3.029	-5.013	0.98	-0.11	-0.005
Evening	1.004	1.007	-0.438	-1.161	0.99	0.14	0.20
X=F13	m_1	m_2	q_1	q_2	R_1^2	d_1	d_2
Morning	0.959	0.953	7.267	8.370	0.98	-0.19	-0.35
Evening	0.982	0.982	3.200	3.205	0.99	0.27	0.25

Table 4.4: Slope (m) and intercept (q) obtained from the linear regression analysis between the selected couples of satellites enhanced PMW T_b at 37 GHz, horizontal polarization over Greenland. The subscripts refer to the case when the coefficients are weighted by means of the R^2 (case 1, see Equation 4.5 and 4.6) or not (case 2). In the Table, we also report the values for the R^2 as well as the values of d computed according to Equation 4.9.

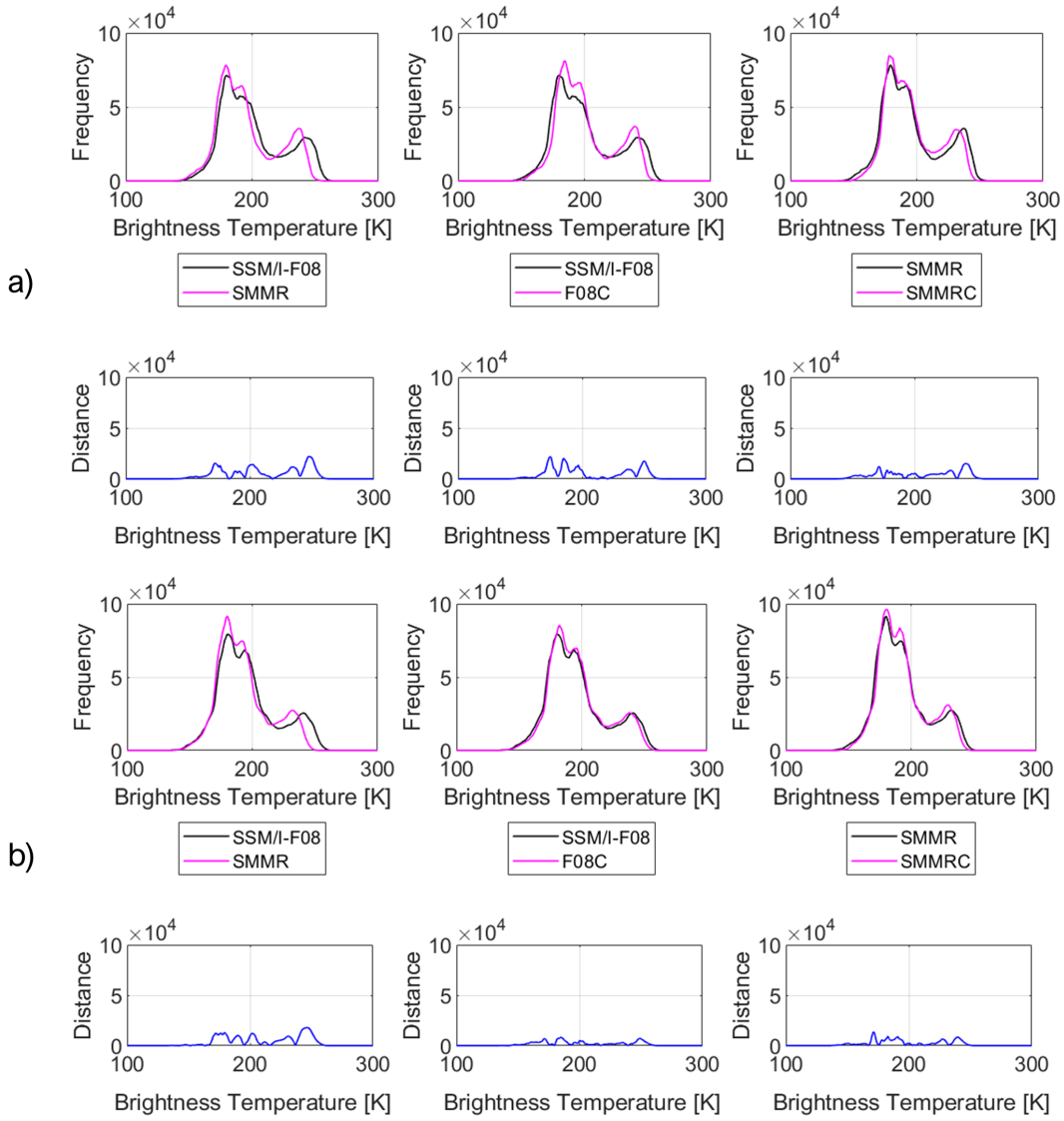

Figure 4.4: Histograms of T_b before and after the application of the intercalibration relations (for Greenland). Relations are applied for both evening (a) and morning (b) passes, and the histograms of the data and the distance (absolute value of the difference as in Equation 4.8) between the histograms for original data are reported. The left column represents the uncorrected data, the central column represents the results applying the correction to SMMR data and the right column represents the results applying the correction to the SSM/I data.

Assessment with AWS data

Historically, the presence of liquid water within the snowpack using data from AWS has been estimated when recorded air temperature exceeds a certain threshold during the day. Because melting can also occur because of radiative forcing (i.e., solar radiation) and the air temperature does not necessarily represent the snow surface temperature, we tested three threshold values for air temperature of 0°C, -1°C and -2°C, as in Tedesco (2009). We assessed the performance of the PMW-based algorithm by defining commission and omission errors. Commission error occurs when melting is detected by PMW data but not by AWS data and omission error occurs when melting is detected by AWS data but not by PMW. The results of the error analysis

are summarized in Table in the case of the different algorithms and the Mote (2014) dataset for the different threshold values on the AWS air temperature values. In the table, values of commission and omission errors are reported as an average over all stations. Specific results for each AWS location are reported in the supplementary material (Table S2, Table S3 and Table S4) together with a map of the AWS network (Figure B.1). Table 4.5 also reports as more general performance indicator the sum of the two commission and omission errors, computed for each AWS case (C+O). We also report an average value of all the C+O (for both AWS and MAR assessments, presented in the next subsection) for each PMW algorithm (C+O Mean) as synthetic index of performance. Our results indicate that the 245K algorithm shows the lowest commission error (between 0.31% and 0.63%) and the highest omission error (5.38%-9.19%). This is consistent with this algorithm being the most conservative among those considered (i.e., the algorithm is not sensitive to sporadic melting). In contrast, a higher commission error is achieved in the case of the $M+30$, $M+35$ and $M+40$ thresholds, particularly for the Humboldt and GITS stations (North-West Greenland), where the commission error is up to one order of magnitude larger than in the case of MEMLS and 245K algorithms for every ground-truth reference (e.g. from 0.70% for MEMLS and 0.09% for 245K to 5.63% for $M+30$, in case of air temperature equal to 0°C). Moreover, we note in the case of the MEMLS algorithm the lowest omission error in Swiss Camp, JAR-1 and JAR-2 sites (6.9% for MEMLS and 8.4% for $M+30$, 10.0% for $M+35$, 12.4% for $M+40$ and 17.4% for 245K). The coarse resolution dataset presents a commission error between 1.02% and 1.74% and an omission error between 4.06% and 7.12%, confirming the capability of historical data in detecting surface melting over the Greenland ice sheet. However, the enhanced resolution dataset presents better results in terms of C+O when applying the $M+40$ and MEMLS algorithms. The sensitivity to the air temperature threshold is low, with commission and omission error, respectively decreasing by about 1% and increasing by 3% when considering threshold values from 0°C to -2°C.

In order to better understand the sources of the relatively high values of the commission errors at some locations, we show in Figure 4.5 the timeseries of air temperature and T_b at 37 GHz H-pol. at three selected stations: a) Summit, b) Humboldt and c) Swiss Camp for the year 2005. The threshold values obtained with the different detection algorithms are also plotted as horizontal lines (black) as well as the 0°C air temperature threshold (magenta). We selected these three locations as they are representative of three different environmental and melting conditions. The timeseries recorded at Summit station (Figure 4.5a) shows the sensitivity of T_b to physical temperature and its seasonal variations. In this case, the air temperature remains below 0°C throughout year and the T_b signal does not exceed any threshold value (horizontal lines). This timeseries is typical of a location where melting is generally absent. The T_b timeseries collected in correspondence of Humboldt location (Figure 4.5b) shows a strong and sudden peak starting on 20 July, when the air temperature average is about -0.5 °C (detected by -1°C and -2°C air temperature thresholds). This event is detected by all algorithms. Nevertheless, the $M+30$ (and similar algorithms) indicate the potential presence of melting also for the period preceding the July melting (between 17 June and 17 July). This melting is not confirmed by other algorithms or by the AWS analysis, suggesting that the threshold value used for these algorithms might be too low. Lastly, melting clearly occurs in the case of Swiss Camp

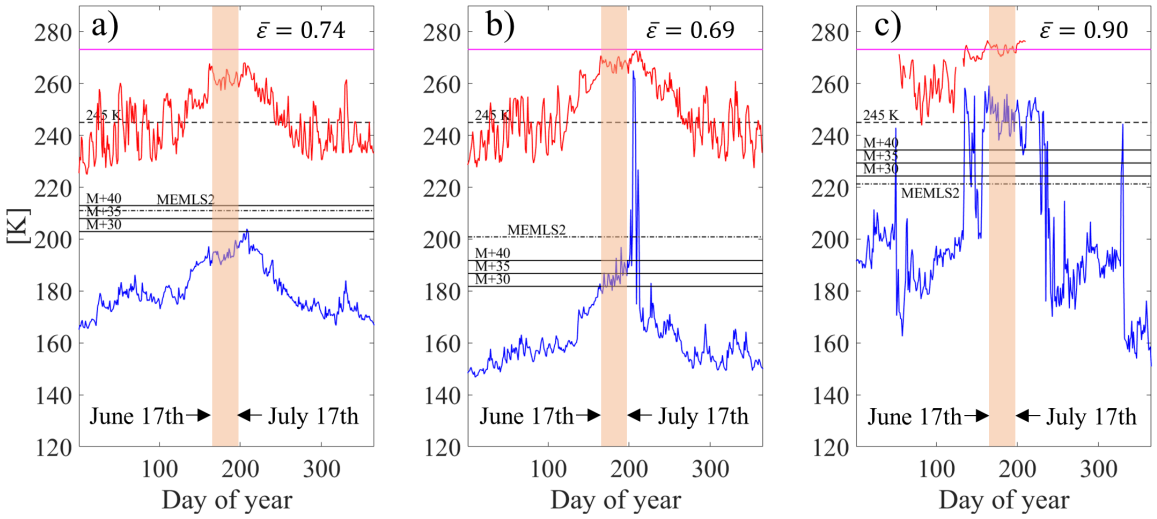

Figure 4.5: Time series of (blue) enhanced-resolution T_b 37 GHz, horizontal polarization, and (red) air temperature at the (a) Summit, (b) Humboldt and (c) Swiss Camp stations for the year 2005. Threshold values obtained with the different detection algorithms are reported as horizontal black lines (solid line, $M + \Delta T_b$; dashed line, 245 K; and dot-dashed line, MEMLS), and the 0 ∘C threshold is reported as a magenta solid line. The 30 d window between 17 June and 17 July is shown in the shaded orange area and reports the average estimated emissivity $(\epsilon)values$.

(Figure 4.5c), characterized by the sharp and substantial increment of T_b beginning around mid-May. For this case, all algorithms detect melting, with the MEMLS providing the lowest threshold and the 245K fixed threshold being the most conservative. The computed rough estimation of the average emissivity for the period 17 June – 17 July (as T_b divided by the recorded air temperature) also suggests that melting is not occurring in the considered period in Humboldt case, presenting an average emissivity even lower than in Summit case. Figure 4.6 shows maps of surface melt extent obtained using the different approaches for July 13th, 2008. Consistent with the results discussed above, the $M + 30$ and $M + 35$ algorithms suggest melting up to high elevations, within the dry snow zone, where it likely did not occur. The $M + 40$ and MEMLS algorithms show similar results, while the 245K fixed-threshold approach shows, as expected, the most conservative estimates. As mentioned, the threshold algorithms for ΔT_b (M+30, etc.) rely on a fixed ΔT_b value, which could produce errors if there is a large seasonal range in T_b due to temperature variability. In contrast, the MEMLS algorithm is based on the linear regression of the ΔT_b as function of different combinations of dry snow conditions (LWC=0, i.e. different winter T_b means). This provides an appropriate threshold value that takes into account the snow conditions before melting and, at the same time, follows a more consistent approach with respect to the amount of LWC detected in the snowpack.

Assessment with MAR outputs

For the comparison between PMW-based and MAR outputs, we averaged the vertical profiles of LWC computed by MAR to the top 5 cm (MAR_{5cm}) and the top 1m (MAR_{1m}) of snowpack

PMW	AWS/MAR	Average % Commission	Average % Omission	C+O %	C+O Mean %
M+30	**0°C**	3.71	2.63	6.34	7.79
	-1°C	3.04	3.78	6.82	
	-2°C	2.44	5.66	8.1	
	MAR$_{1m}$	7.11	1.51	8.62	
	MAR$_{5cm}$	7.01	2.07	9.07	
M+35	**0°C**	2.34	3.19	5.53	6.83
	-1°C	1.83	4.5	6.33	
	-2°C	1.37	6.35	7.72	
	MAR$_{1m}$	5.5	1.83	7.33	
	MAR$_{5cm}$	4.78	2.48	7.26	
M+40	**0°C**	1.73	3.98	5.72	6.84
	-1°C	1.3	5.37	6.68	
	-2°C	0.93	7.32	8.25	
	MAR$_{1m}$	4.49	2.23	6.72	
	MAR$_{5cm}$	3.88	2.98	6.87	
MEMLS	**0°C**	2.7	2.38	5.08	6.66
	-1°C	2.13	3.62	5.76	
	-2°C	1.63	5.44	7.07	
	MAR$_{1m}$	6.33	1.49	7.81	
	MAR$_{5cm}$	5.52	2.04	7.56	
245K	**0°C**	0.63	5.38	6.01	6.92
	-1°C	0.46	7.02	7.48	
	-2°C	0.31	9.19	9.51	
	MAR$_{1m}$	2.58	2.95	5.53	
	MAR$_{5cm}$	2.23	3.83	6.06	
25 km Mote (2014)	**0°C**	1.74	4.06	5.80	7.10
	-1°C	1.37	5.35	6.72	
	-2°C	1.02	7.12	8.15	
	MAR$_{1m}$	4.74	2.72	7.46	
	MAR$_{5cm}$	4.11	3.28	7.39	

Table 4.5: Performance of the PMW melt detection algorithms studied with AWS and MAR data. Five thresholds are used to detect melt at a 3.125 km resolution, and the Mote (2014) melting dataset is used as a 25 km resolution comparison. For each case, three thresholds (0, 1 and 2 ∘C) are applied to the AWS data and two approaches (MAR$_{1m}$ and MAR$_{5cm}$) are applied to the MAR-simulated LWC to detect melt. The performance of the respective PMW melting products is computed in terms of commission and omission errors averaged for all of the AWS sites considered. C+O refers to the total error considering both commission and omission. The average of the C+O of each melting dataset (C+O Mean) is reported as a synthetic index of performance.

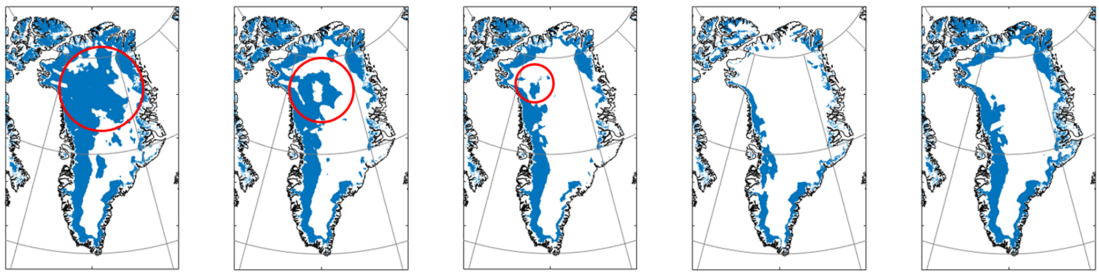

Figure 4.6: Melting maps obtained using the (a) $M + 30$, (b) $M + 35$, (c) $M + 40$, (d) 245 K and (e) MEMLS algorithms over the Greenland ice sheet on 13 July 2008. An example of an area presenting the false detection problem is shown in the red circle.

following Fettweis et al. (2007). In order to be consistent with the minimum LWC to which the MEMLS algorithm is sensitive, we set the threshold on the LWC values to which we assume melting is occurring to 0.2% for both depths. We selected two different depths for our analysis so we could study two types of melting events: (1) sporadic surface melting, affecting the first few centimeters of the snowpack, and (2) persistent subsurface melting, affecting the snowpack from the surface up to around the first meter. For consistency with the AWS analysis, we report the results averaged over those MAR pixels containing the AWS stations discussed in the section above in Table 4.5. The comparison between the results obtained from the PMW and modelled LWC indicates that the more conservative approaches (i.e., 245K) perform better when considering the case of MAR_{5cm}. In fact, the 245K threshold shows the lowest overall error for this case (C+O = 6.06%). The coarse resolution dataset shows a C+O error equal to 7.39%, slightly lower than in case of MEMLS (7.56%). In the case of the top 1 m, all the algorithms present similar performances on average, with the best performance obtained again in the case of the 245K (C+O=5.53%). However, all the $M + \Delta T_b$ algorithms present the same issue of larger commission error than MEMLS and 245K (e.g., from 0.99% for MEMLS and 0.26% for 245K to 4.62% for $M + 30$) in North-East Greenland (e.g., Humboldt and GITS stations, see Table S2 and Table S3 in the supplementary material). This confirms the results we obtained from the comparison with AWS data, pointing out the overestimation of melting in some dry areas by $M + \Delta T_b$. For both the MAR_{1m} and MAR_{5cm} cases, for all the considered algorithms, we find a high commission error in the cases of the JAR-1, JAR-2 and Swiss Camp sites (between 10% and 22%).

In order to better understand the origins of these errors, we show in Figure 4.7 further insights into the differences between the PMW T_b and MAR outputs. Figure 4.7a and b show, respectively, the timeseries of LWC averaged over the first 5cm (MAR_{5cm}) and 1m (MAR_{1m}) obtained from MAR at the Swiss Camp site. In Figure 4.7c we report the T_b timeseries and the daily average air temperature (threshold values reported as horizontal lines). We first note an early melt event (labeled LWC=0.046% in Figure 4.7b for the 108th day of the year) detected by PMW MEMLS algorithm and at the AWS station but apparently undetected in MAR_{1m}. A closer look to the time series shows that in fact MAR_{1m} does estimate a LWC of 0.046% on this

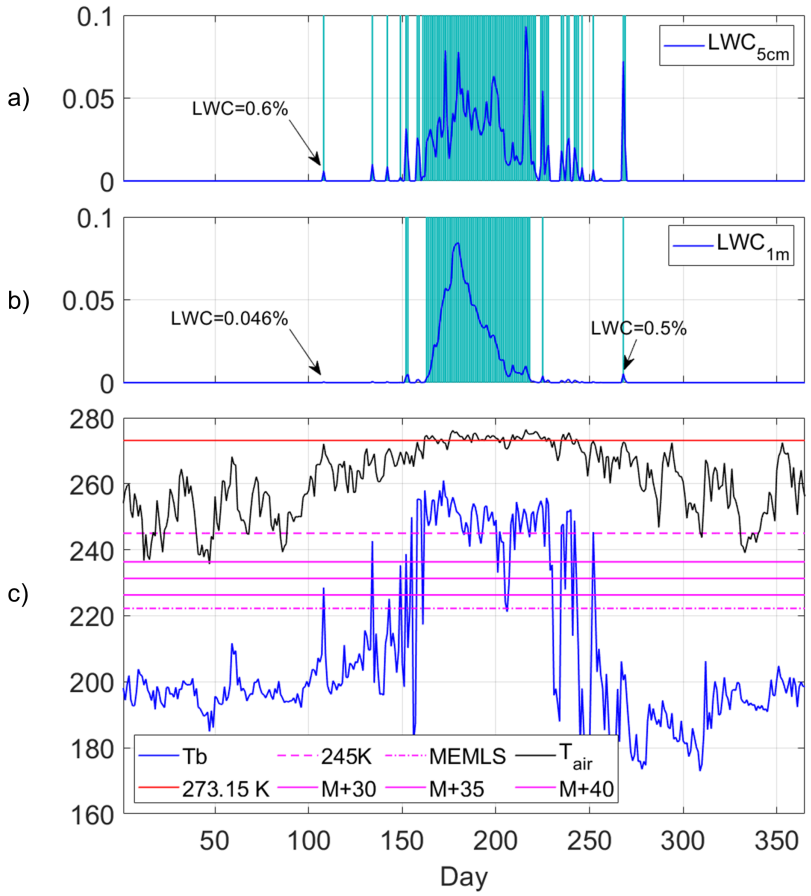

Figure 4.7: LWC from MAR averaged in the first 5 cm (a) and the first 1 m (b) of the snowpack. (c) Time series of the 37 GHz horizontally polarized T_b (3.125 km, blue), air temperature from AWS (black) and 245 K (dashed magenta line), $M + \Delta T_b$ (solid magenta lines) and MEMLS (dot-dashed magenta line) thresholds for the Swiss Camp site in the year 2001. Melting days according to MAR are marked as vertical light blue lines in panels (a) and (b).

day while MAR_{5cm} a LWC of 0.6%. This suggests that in some cases (before the main melt season) the MEMLS algorithm is actually sensitive to the LWC in the first 5 cm of snowpack, as a consequence of the approximation of the electromagnetic outputs imposed by the linear fitting. We also note a melt event (labeled with LWC=0.5% in Figure 4.7b) at the end of the melting season detected by both AWS data (air temperature larger than -1°C) and MAR (both in the first 5 cm and 1 m of snow) but not by any PMW algorithm. The T_b timeseries reveals a small peak, but the signal is not strong enough to exceed any threshold. This corresponds to a rainfall event (simulated by MAR) suggesting that the sensitivity to liquid clouds of the 37 GHz channel could mask some melt events. Moreover, at the end of the melting season the T_b appears to be slightly lower than January/February average, possibly because of an increment in grain size after refreezing, leading to a lower emissivity.

The results discussed above (together with results from the comparison with AWS data) suggest that 245K is the most conservative among the approaches we tested, providing the lowest

(highest) commission (omission) error but being unable to detect sporadic melt events. On the contrary, the MEMLS and $M + \Delta T_b$ algorithms can detect sporadic melt events and present lower omission error compared to 245K. However, $M + \Delta T_b$ algorithm overestimate melting in some dry areas (North West of the ice sheet), suggesting melting when it is not actually occurring. Contrarily, MEMLS algorithm is not affected by the large commission error in dry areas, presents the lowest omission error in Swiss Camp area (together with $M + 30$) and is still sensitive to low levels of LWC. Considering the average error (C+O Mean in Table 4.5), the MEMLS algorithm shows the best performance (6.66%). In view of the presented analysis and the different sensitivity to surface and subsurface melting, in the following we focus on the 245K and MEMLS algorithms to study the extent of persistent and sporadic surface melting, respectively.

As a further analysis, we compared the PMW-retrieved melt extent with that estimated from MAR outputs. In Figure 4.8 we show the timeseries of melt extent integrated over the whole ice sheet for two selected years ((a) 1983 and (b) 2005, selected randomly to present an example of SMMR and SSM/I cases) estimated according to MAR_{1m} and MAR_{1m} together with the timeseries of the melt extent from the PMW data. The analogous figure for the coarse resolution dataset is reported in the supplementary material (Figure S2). For each year, we compute the daily melt extent for the period 1 May to 15 September and use the Nash-Sutcliffe Efficiency (NSE) coefficient (Nash and Sutcliffe, 1970), described in Section 3, for a quantitative analysis. Here, we remind the reader that NSE coefficient can assume values in the interval $(-\infty, 1]$. A perfect match between the two timeseries is achieved when the NSE coefficient is 1. NSE coefficient in the [0,1] interval indicate that the modelled variable is a better predictor of the measurements than the mean. If NSE coefficient is a negative number, the mean of the measured data describes the timeseries better than the modelled predictor. Here, we chose NSE=0.4 as efficiency threshold, considering that we compute melt extent at daily timescale and from datasets at two different resolutions (i.e., resulting in an intrinsic bias related to the different pixel size). We compared the timeseries of melt extent obtained using the 245K algorithm with MAR_{1m} (245K vs. MAR_{1m}) and the MEMLS melt extent with MAR_{1m} (MEMLS vs. MAR_{1m}) due to the expected differences in sensitivity to detect persistent and sporadic melting between 245K and MEMLS, respectively. We compare the melt extent obtained from the coarse resolution dataset with MAR_{1m}, according to the similarity with MEMLS in terms commission/omission error. We report NSE coefficients computed for the 41-year (34-year in case of the coarse resolution dataset) period in Table 4.6. At first, we notice that for the 1979-1992 period the comparison between 245K and MAR_{1m} produces large negative NSE coefficients, indicating an unsatisfactory match between PMW and MAR derived melt extents. The comparison between MEMLS and MAR_{1m} presents negative values of NSE coefficient as well (unsatisfactory results). Similarly, the coarse resolution dataset shows negative values of NSE coefficient, larger than MEMLS but smaller than 245K. Between 1987 and 1992, we found larger but still negative NSE coefficients presenting smaller absolute values. Between 1993 and 2019, we found for every year negative values of NSE coefficient for 245K and positive values for MEMLS, indicating satisfactory results only for the latter algorithm. However, the coarse resolution dataset presents positive (but not satisfactory) values of NSE coefficient only in 2003 and

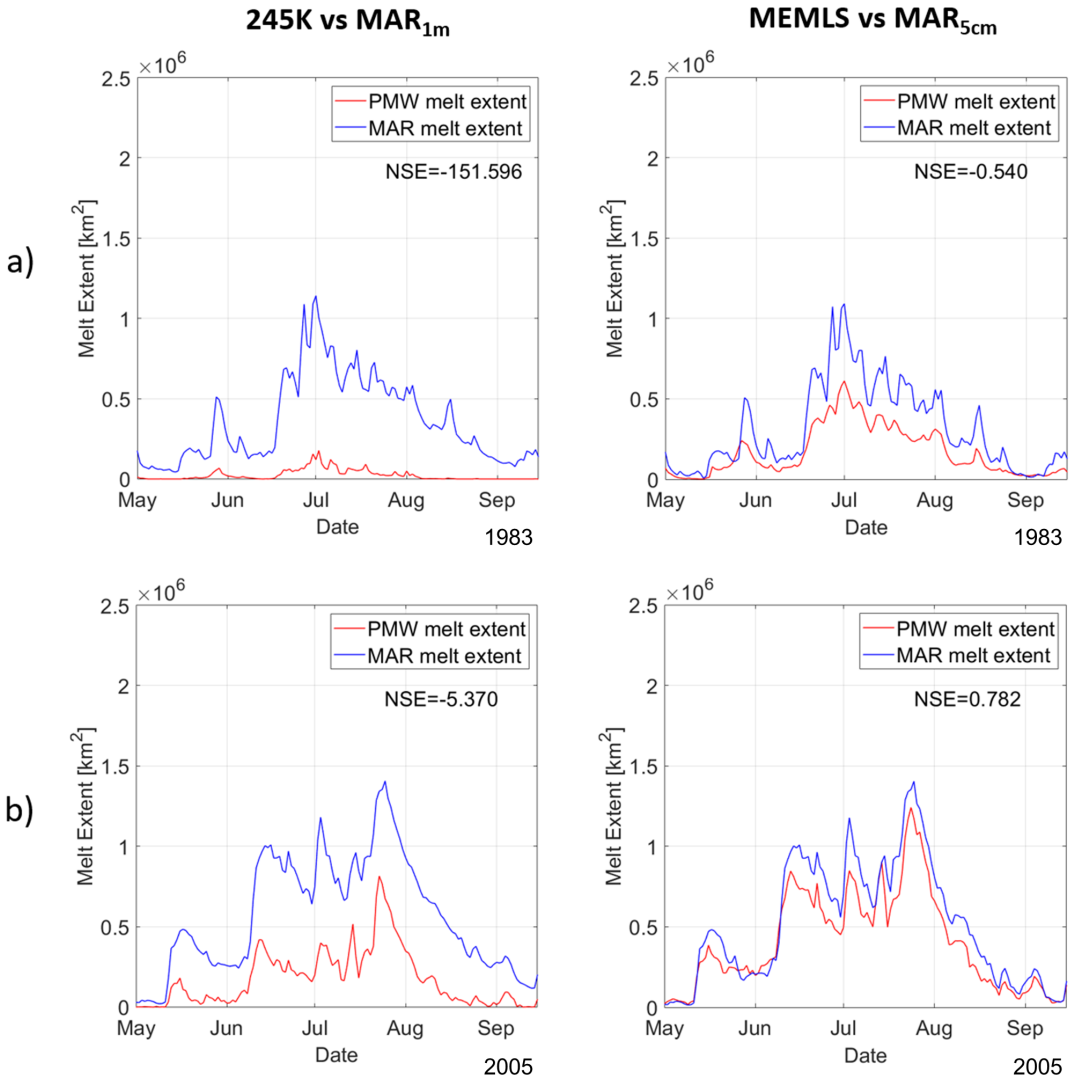

Figure 4.8: Melt extent estimation from PMW 37 GHz horizontally polarized T_b (red) and the MAR (blue) regional climate model. Time series were obtained using the 245 K algorithm and the LWC average in the first 1 m of the snowpack (left), and the MEMLS algorithm and the LWC average in the first 5 cm of the snowpack (right), for the years (a) 1983 and (b) 2005.

2012 (0.111 and 0.208, respectively). The timeseries in Figure 4.8a reveals a strong underestimation of 245K-derived melt extent relative to MAR_{1m} (the cause of low NSE= -151.596) and shows the slightly better matching in case of MEMLS (NSE=-0.540). This result suggests that, in case of SMMR data, T_b values cannot always reach the 245 K threshold, even if the snowpack is saturated with liquid water and surface melting is developed, possibly due to a persistent bias after the intercalibration of the dataset. As a consequence, the 245K threshold might be too high in the first part of the dataset, resulting in an underestimation of the melt extent. On the contrary, MEMLS threshold, generally lower, can better capture the spatiotemporal evolution of surface melting, even if the melt extent is still underestimated. A possible consequence of the melt extent being underestimated in the first part of the timeseries is a slightly overestimated

long-term trend. To address this possible implication, in the next section we compute long-term trends considering both 1979 – 2019 and 1987 – 2019 reference periods. In Figure 4.8b, the timeseries obtained with 245K appears to better follow the temporal variability of melt extent from MAR during the melting season but still presenting a strong underestimation (NSE= -5.250). On the other hand, MEMLS-derived timeseries better matches the MAR-derived one, showing a largely satisfactory NSE coefficient (0.782). In these two years the NSE coefficient computed for the coarse resolution case is negative. The magnitude of the errors is lower than in case of 245K algorithm, indicating a weaker underestimation of the melt extent. This can be a consequence of the coarser resolution, lacking in capturing melting areas at the edges of the Greenland ice sheet.
In summary, 245K threshold, even if presenting acceptable results in terms of commission and omission error considering both AWS and MAR comparison, is too high to fully capture the melt extent everywhere over the ice sheet. Contrarily, we found that MEMLS algorithm is suitable in capturing the evolution of melting over the Greenland ice sheet. The comparison with 25 km historical surface melting dataset shows the same underestimation issue of 245K. Even showing lower errors than in case of 245K, we did not find acceptable values of NSE coefficient.

4.3.3 Surface melting trends

Here, we report results concerning trends of melt duration, length of the melting season and melt extent. We define melt duration (MD) as the total number of days when melting is detected. We compute trends of MD over the whole ice sheet (mean melt duration, MMD, averaged over the total ice sheet area) and at a pixel by pixel scale. We also study the maximum melting surface (MMS, maximum extent of melting area, i.e. the sum of the pixel areas in which melting has been detected at least once over a period, expressed as a fraction of the total ice sheet area) and the cumulative melting surface or melting index (MI, the sum of the melting pixel days multiplied by the area subjected to melting, i.e. the integral of the MD timeseries; Tedesco et. al, 2007). Lastly, we define melt onset date (MOD) and melt end date (MED) as the first day when melting occurs for two days in a row and when melting does not occur for at least 2 days in a row. We report the comparison with the trends computed according to the coarse resolution dataset with reference to the time period of data availability (1979 – 2012). Figures related with this analysis can be found in the supplementary material. We report in Figure 4.9 the timeseries of annual values of MMD, MMS and MI for the 1979-2019 and 1988-2019 reference periods. We decided to look at two different reference periods in view of the fact that SMMR data is collected every other day and that the SMMR and SSM/I sensors are fundamentally different from each other (where this is not true in the case of the remaining SSM/I sensors). We show the results obtained applying the MEMLS algorithm (the one that presented the highest performances in all the considered cases) and the 245K threshold (because it presents good performances in the omission/commission errors analysis, even if it shows the limit of strong underestimation of melt extent from the comparison with MAR outputs). In the case of MMD (Figure 4.9a), we obtain a positive statistically significant (p-value¡0.05) trend from both the 245K and MEMLS algorithms (except for the 245K for the period 1988-2019), being 0.249 d y^{-1} (0.108 d y^{-1}) in

Year	NSE 245K vs. MAR_{1m}	NSE MEMLS vs. MAR_{5cm}	NSE MOTE vs. MAR_{5cm}	Year	NSE 245K vs. MAR_{1m}	NSE MEMLS vs. MAR_{5cm}	NSE MOTE vs. MAR_{5cm}
1979	-128.769	-0.792	-5.644	**2000**	-5.578	0.879	-0.113
1980	-278.146	-2.917	-15.301	**2001**	-10.947	0.771	-0.108
1981	-173.495	-0.881	-7.615	**2002**	-6.553	0.731	-0.537
1982	-176.464	-1.251	-15.989	**2003**	-13.279	0.727	0.111
1983	-151.596	-0.540	-4.987	**2004**	-7.827	0.682	-0.476
1984	-144.117	-1.616	-11.158	**2005**	-5.370	0.782	-0.880
1985	-267.337	-2.639	-12.886	**2006**	-5.250	0.747	-0.159
1986	-128.639	-1.573	-12.325	**2007**	-4.858	0.824	0.0628
1987	-39.524	-1.893	-8.267	**2008**	-9.047	0.701	-0.128
1988	-35.124	-0.299	-2.683	**2009**	-5.219	0.770	-0.957
1989	-22.782	-0.030	-4.096	**2010**	-8.352	0.638	-0.506
1990	-41.515	-0.342	-3.331	**2011**	-4.591	0.882	-1.016
1991	-31.614	-0.422	-4.805	**2012**	-3.400	0.851	0.208
1992	-10.904	0.893	-0.644	**2013**	-8.618	0.760	-
1993	-6.456	0.818	-1.494	**2014**	-9.785	0.646	-
1994	-11.267	0.529	-2.410	**2015**	-11.418	0.611	-
1995	-7.7644	0.021	-0.839	**2016**	-11.827	0.505	-
1996	-10.212	0.512	-2.562	**2017**	-90.906	-0.323	-
1997	-6.449	0.771	-0.648	**2018**	-35.901	0.485	-
1998	-8.263	0.605	-2.558	**2019**	-39.983	0.319	-
1999	-4.201	0.865	-5.644				

Table 4.6: Nash-Sutcliffe Efficiency (NSE) coefficients computed for the comparison of retrieved melt extent using 245K and MEMLS algorithms applied to the enhanced resolution PMW Tb and MAR liquid water content outputs averaged in the first 1 m and first 5 cm of the snowpack. Nash-Sutcliffe Efficiency coefficients for the comparison of the coarse resolution dataset (Mote, 2014) are computed considering MAR_{5cm}.

the case of the 245K algorithm for the period 1980 – 2019 (1988 – 2019) and 0.451 d y^{-1} (0.291 d y^{-1}) in the case of the MEMLS algorithm. The trends computed using the coarse resolution dataset (Figure S3a in the supplementary material) results equal to 0.587 d y^{-1} for the period 1979 – 2012 and 0.595 d y^{-1} for the period 1988 – 2012, smaller than MEMLS (0.704 and 0.671 d y^{-1}, respectively) but larger than 245K (0.457 and 0.418 d y^{-1}, respectively). Also for the MMS (Figure 4.9b), both the 245K and MEMLS algorithm indicate statistically significant positive trends (p-value¡0.05 for every case, p-value¡0.1 for MEMLS for the period 1988-2019). The computed trends suggest that the MMS has been increasing by 0.69% y^{-1} in the case of MEMLS and 0.94% y^{-1} in the case of the 245K algorithm for the period 1979-2019 (percentage with respect to the whole ice sheet surface area). For the 1988 – 2019 period, we also found that the trends are statistically significant but smaller in value (0.36% y^{-1} for MEMLS and 0.47% y^{-1} for 245K). The obtained trends computed using the 25 km dataset (Figure S3c in the supplementary material) are equal to 1.31% y^{-1}.for the period 1979 – 2012 and 0.91% y^{-1} for the period 1988 -2012, larger than the trends computed for MEMLS (1.03% y^{-1} and 0.7% y^{-1}) but smaller than the ones computed for 245K (1.50% y^{-1} and 1.23% y^{-1}). In the case of MI (Figure 4.9c), we also found positive statistically significant trends of 9.166 x 105 km^2 d y^{-1} (MEMLS) and 5.862 x 105 km^2 d y^{-1} (245K) for the complete timeseries. When considering the reduced reference period, we found a 95% statistically significant trend of 5.726 x105 km^2 d y^{-1} only in case of MEMLS. The trends computed for the 25 km resolution dataset (Figure S3b in the supplementary material) results equal to 0.999 x106 km^2 d y^{-1} (1979 - 2012) and 1.019 x106 km^2 d y^{-1} (1988 - 2012), smaller than MEMLS (1.428 x106 km^2 d y^{-1} and 1.325 x106 km^2 d y^{-1}, respectively) and 245K for the period 1979-2012 (0.999 x106 km^2 d y^{-1}) but larger than 245K for the period 1988 - 2012 (1.019 x106 km^2 d y^{-1}). Lastly, we report in Figure 4.9d the MOD and MED averaged spatially over the pixels with 95% significant trends. We found that average MOD (crosses in Figure10d) presents similar trends for 245K and MEMLS considering both the entire and shortened time series equal to -0.546 d y^{-1} and -0.273 d y^{-1}, respectively, in case of 245K and -0.404 d y^{-1} and -0.254 d y^{-1} in case of MEMLS. For the reference period 1979 – 2012 (1988 – 2012) the trends of the MOD computed from the 25 km resolution dataset (Figure S4a in the supplementary material) resulted equal to -0.585 d y^{-1} (- 0.562 d y^{-1}), respectively equal and larger in absolute value than MEMLS between 1979-2012 (-0.585 d y^{-1}) and MEMLS between 1988-2012 (-0.494 d y^{-1}) but smaller than 245K for the period 1979-2012 (-0.801 d y^{-1}) and 245K for the period 1988-2012 (-0.568 d y^{-1}). On the contrary, in case of average MED (in red) we found larger differences when considering the reduced timeseries with results equal to 0.687 d y^{-1} for 245K (1979-2019), 0.708 d y^{-1} for MEMLS (1979-2019) and 0.396 d y^{-1} for MEMLS (1988-2019). The 245K algorithm does not present a statistically significant trend over the period 1988 - 2019. This difference suggests that 245K algorithm may have stronger limitations in capturing the last portion of the melting season in case of SMMR data thus confirming the problems observed for the melt detection with this source of data vs. MAR_{1m} simulations. The trends computed from the coarse resolution dataset (Figure S4b in the supplementary material) are equal to 0.850 for the period 1979 – 2012 and 0.716 for 1988 – 2012. For the period 1979 – 2012 (1988 – 2012) we found a delay of 0.937 d y^{-1} (0.621 d y^{-1}) in case of MEMLS and 1.046 d y^{-1} (0.521 d y^{-1}).

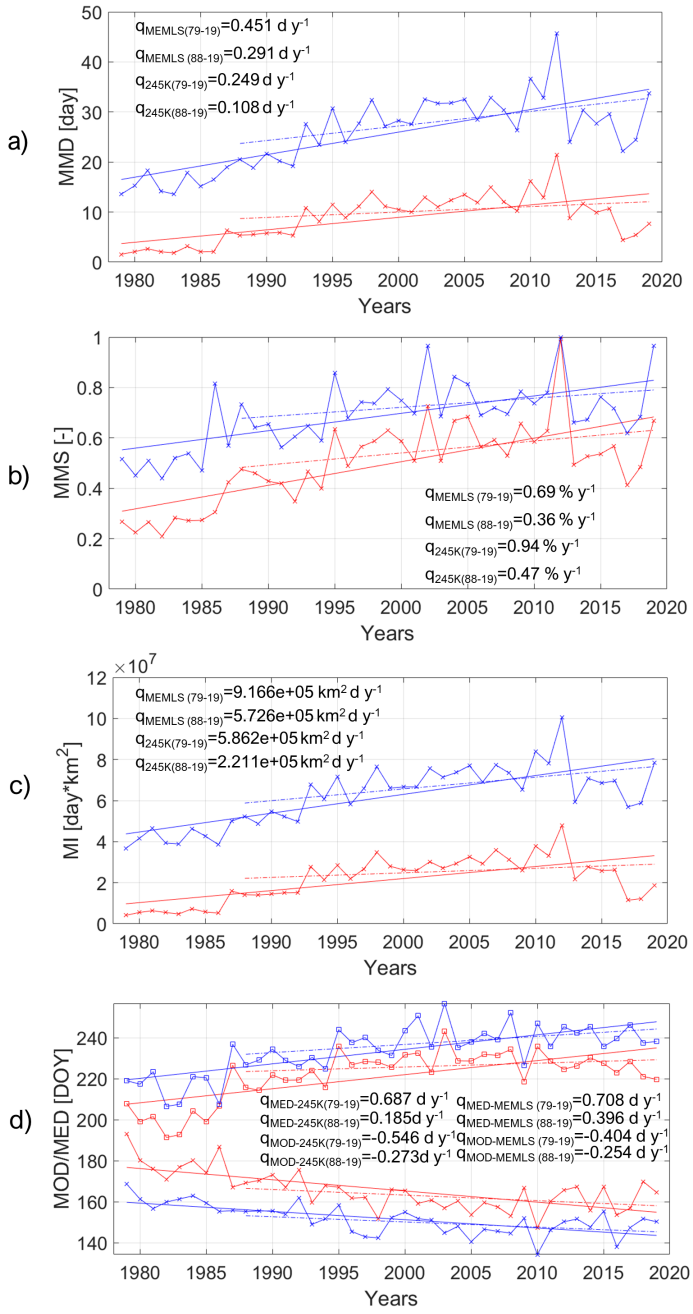

Figure 4.9: Time series of annual (a) mean melt duration (MMD), (b) maximum melting surface fraction (MMS, expressed as fraction of the surface area of the ice sheet), (c) melt index (MI), and (d) melt onset date (MOD) and melt end date (MED). Regression lines were computed for the 1979–2019 (solid line) and 1988–2019 (dot-dashed line) periods. The MMD is averaged over all of the Greenland ice sheet pixels. Red (blue) lines refer to the 245 K (MEMLS) algorithm; in panel (d), squares (crosses) refer to MED(MOD).

In Figure 4.10 we show the trends of MD, MOD and MED on a pixel-by-pixel basis for the complete time series (1979-2019). We found that the trend in MD exhibits the highest statistical significance (in terms of number of statistically significant pixels), being the most stable and

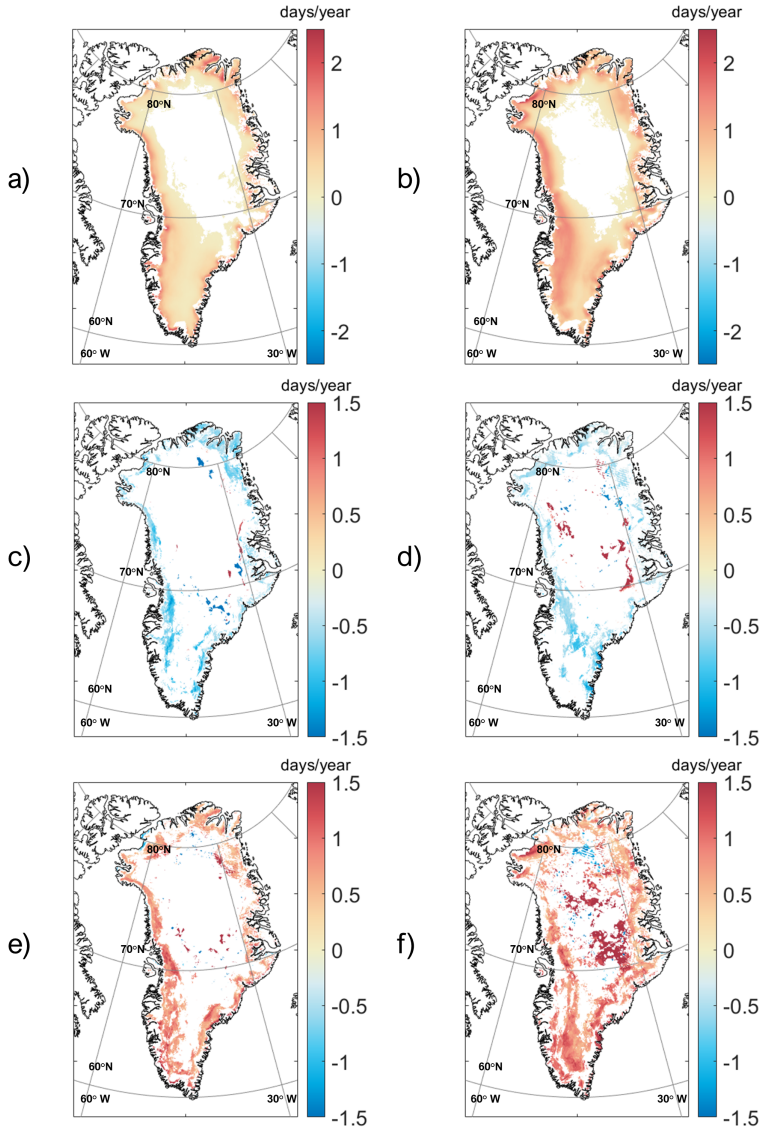

Figure 4.10: Maps of 95 % significant trends (1979–2019) obtained with the 245 K (a, c, e) and MEMLS (b, d, f) algorithms for melt duration (MD; panels a and b), melt onset date (MOD; panels c and d) and melt end date (MED; panels e and f). MOD and MED are defined as the first and last 2 melting days in a row.

reliable trend among the pixel-by-pixel parameters analyzed. We found mostly positive trends in MD in all pixels (Figure 4.10a and b), with higher values moving towards the coastline, maxima in the ablation zone of the Jakobshavn Isbrae (2.40 d y^{-1}) for 245K and 2.66 d y^{-1} for MEMLS) and minima in high altitude areas. We averaged the statistically significant trends, finding an average of 0.468 d y^{-1} for the 245K algorithm, and of 0.697 d y^{-1} in the case of the MEMLS. In case of MOD and MED, we found a lower number of statistically significant pixels. The statistically significant pixels exhibit a negative trend for MOD (Figure 4.10c and d) and a positive trend for MED (Figure 4.10e and f), with the melting season starting on average 0.694 d y^{-1} earlier and ending 0.680 d y^{-1} later according to 245K algorithm (0.360 d y^{-1} earlier and

0.909 d y^{-1} later for MEMLS). We point out that the average of the statistically significant trends is generally higher than the trends computed at ice sheet scale since we computed the average over the statistically significant pixels only.

4.3.4 Spatial information content

In order to investigate the spatial information content of the enhanced resolution PMW data with respect to the coarser one, we also performed a variogram-based analysis of MD estimated from the two products when using either the 245K or the MEMLS algorithms. We point out that knowledge of scales is imperative for improving our understanding of the observed changes because processes and related relationships change with scale. Moreover, quantifying the variability of processes across scales is a critical step, ultimately leading to proper observation and modeling scale resolution. In this regard, the relationship between processes, observation and modeling scales controls the ability of a tool to detect and describe the constituent processes. Here, we show our preliminary results of a variogram-based analysis applied to MD estimated from the MEMLS and 245K algorithms for the months of May through August of 2012 when using either the enhanced or the coarse resolution products. We also performed the same analysis applied to MD estimated using LWC modelled with MAR, according to the same rationale described in the previous sections. Here, we compute the MD for each month of the melting season at pixel-scale as the number of days of the month (May, June, July or August) detected as melting for the specific pixel. The results of our analysis are summarized in Figure 4.11, where we show the empirical (blue crosses) and modelled (red line) semi-variograms for Greenland MD computed applying the MEMLS and 245K algorithms to both 25 km and 3.125 km resolution data for the months of May through August of 2012, and in Table 7, where we report the parameters of the spherical fitting of the empirical semi-variogram in case of MD obtained according to MAR_{1m} and MAR_{5cm} approaches (an analogous representation of Figure 4.11 is reported in the supplement in Figure S5). At first, we note that R^2 values of the fitting for the modeled variograms are consistently higher in the case of enhanced resolution data, suggesting that enhanced resolution data might be more suitable for a variogram-based analysis. For the coarse resolution data, we found R^2 values of comparable magnitude with the enhanced resolution case only in May. When computing the spherical fitting of the empirical variograms of MD from MAR, we found for each case considered similar R^2 values (between 0.118 and 0.484). The values for the range in the case of the 3.125 and 25 km products are similar in May for the 245K algorithm (on the order of $\sim$ 200 km) but they appear different in the case of the MEMLS algorithm, when the enhanced product shows a lower value of $\sim$ 170 km against $\sim$ 270 km in the case of the coarse product. This could be due to the fact that the MEMLS algorithm is more sensitive to sporadic melting and when applied to the enhanced T_b dataset it allows to detect melting driven by processes whose scale cannot be captured by the coarser nature of the historical dataset. In case of MAR, the value of the range is lower in case of MAR_{5cm} (187.70 km) than in case of MAR_{1m} (199.17 km), suggesting again the affinity of MEMLS algorithm with melting strictly confined in the very first layer of snowpack. As the melting season progresses, the variograms of the coarse dataset shows either similar values for the range or a poor fit of the experimental variogram. Instead, in the case of the enhanced

	May		June		July		August	
	$\mathbf{MAR}_{1m}$	$\mathbf{MAR}_{5cm}$	$\mathbf{MAR}_{1m}$	$\mathbf{MAR}_{5cm}$	$\mathbf{MAR}_{1m}$	$\mathbf{MAR}_{5cm}$	$\mathbf{MAR}_{1m}$	$\mathbf{MAR}_{5cm}$
r	199.17	187.70	233.05	207.26	186.16	282.57	211.7	230.32
s	3.97	4.02	18.28	17.78	19.66	5.24	14.08	1.78
n	3.35	4.66	44.97	37.94	79.79	31.86	28.64	5.58
$\mathbf{R}^2$	0.2	0.34	0.41	0.48	0.24	0.14	0.38	0.12

Table 4.7: Parameters of the spherical function fitted to the empirical semi-variogram for the maps of melt duration (MD) obtained cumulating the LWC simulated by MAR over the first 1m and 5 cm of snowpack.

product, the values of the range tend to decrease up to July and increase again in August. We found the same temporal variability in case of MAR_{1m}, while in case of MAR_{5cm} we found that the range increases until July and decreases in August (see Figure S5 in the supplementary material). Moreover, a proper fitting of the experimental variograms is achieved for all cases for the enhanced resolution PMW and the MAR derived MD. This suggests that the 25 km spatial resolution might be too coarse to capture the spatial autocorrelation of melting processes. In terms of nugget effect, we found larger values from the MAR outputs than in case of PMW. The decrease in the range in the case of the enhanced product may be a consequence of the local processes that drive melting as the melting season progresses (e.g., impact of bare ice exposure, cryoconite holes, new snowfall, etc.) and of a more developed network of surface meltwater, the presence of supraglacial lakes and, in general, the fact that the processes driving surface meltwater distribution (e.g., albedo, temperature) promote a stronger spatial dependency of meltwater production at smaller spatial scales. This is even more important when considering that the width of regions such as the bare ice area (where substantial melting occurs) is of the same order of magnitude of the resolution of the coarse PMW dataset. In August, the start of freezing of the surface runoff system and the covering of bare ice, cryoconite holes, together with the draining of the supraglacial lakes and rivers might justify the increase in the range values computed for this month. Our preliminary results, therefore, point to an increased information content of the enhanced spatial PMW product with respect to the historical, coarse one, offering the opportunity to better capture the spatial details of how surface melting evolved over the Greenland ice sheet over the past $\sim$ 40 years. Further analysis will help to shed light on the processes responsible for the recent acceleration of surface melting.

4.4 Conclusions and future work

We applied threshold-based melt detection algorithms to the 3.125 km resolution 37 GHz horizontal polarization PMW T_b to assess the skills of the PMW enhanced-resolution data to detect surface melting over the 1979-2019 period over the Greenland Ice Sheet. As the product is composed of data acquired by different sensors onboard of different platforms, we first developed a cross calibration among all the sensors. Then, we compared surface melting detected from PMW enhanced-resolution data with that estimated from AWS air temperature data and the outputs of the regional climate model MAR. We found that the algorithm making use of a fixed threshold value on T_b values (245K) and the one based on the outputs of an electromagnetic model

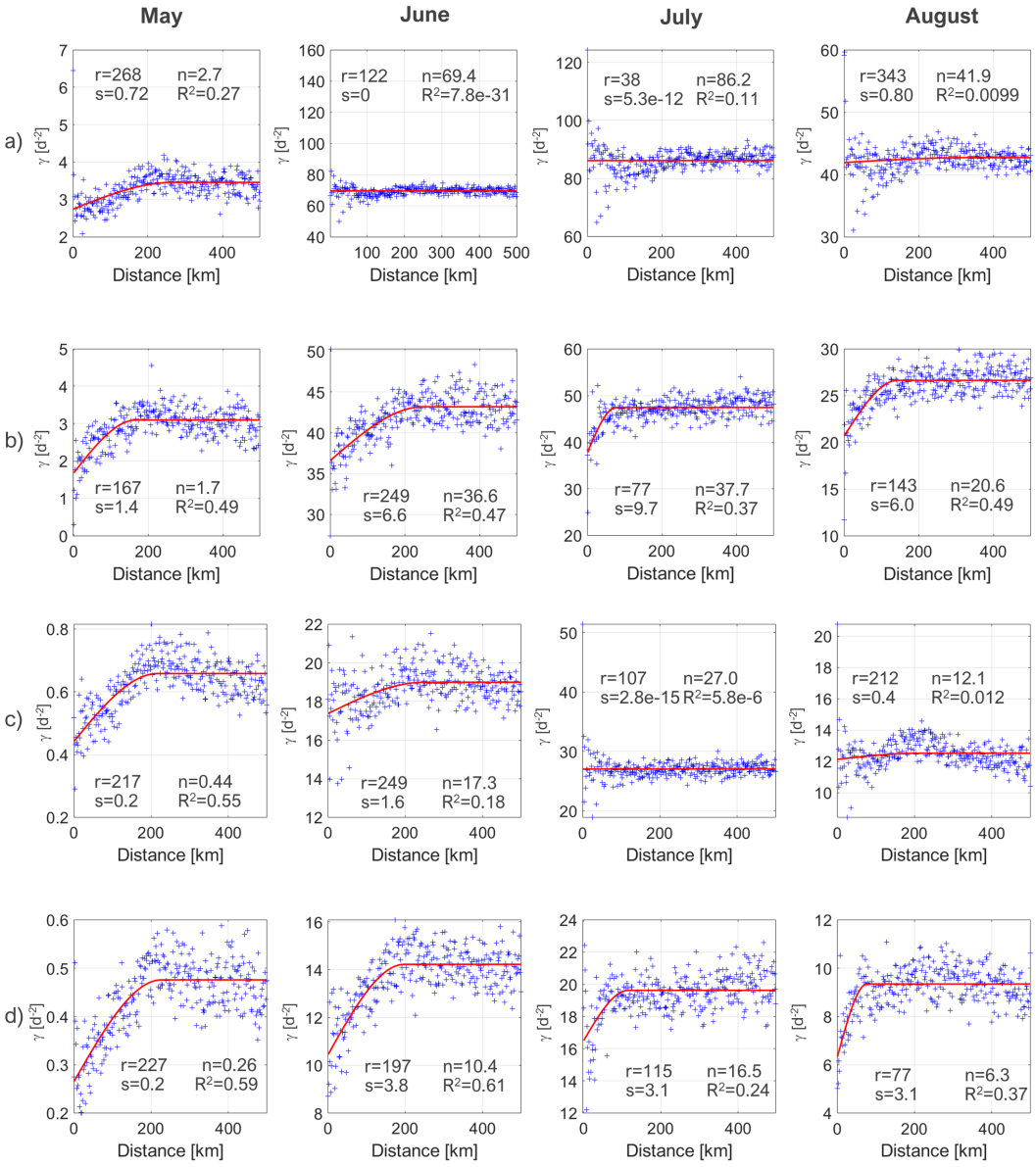

Figure 4.11: Empirical (blue crosses) and modeled (red line) semi-variograms for the Greenland melt duration (MD) computed by applying the (a, b) MEMLS and (c, d) 245 K algorithms to both the (a, c) 25 km and (b, d) 3.125 km resolution data for each month of the melting season (May, June, July and August). The range (r), sill (s), nugget (n) and R^2 values are reported.

were the most suitable to detect persistent (245K) and sporadic (MEMLS) melting. Overall, we found that that MEMLS algorithm showed the best performance (lowest commission and omission errors). We compared surface melting detected from PMW enhanced-resolution data with the one estimated by the MAR model when considering the two cases of integrating LWC over the top 5cm and 1m, respectively. We selected these two depths to study those conditions when melting occurs sporadically (5 cm) or persistently (1 m). We obtained good matching (i.e., NSE¿0.4 or, at least, positive) in most of the years from 1992-2019 when comparing MEMLS

derived melt extent with MAR LWC in the first 5 cm of snowpack. On the other hand, we found bad matching in the period 1979-1992, possibly due to differences in sensor characteristics. In the case of melt extent retrieved by 245K, we found a strong underestimation of melt extent (largely negative values of NSE coefficient) from 1979 to 1987 likely because of the lower values of "wet" T_b in case of SMMR data, slightly improving from 1993 to 2019 but still negative. Accordingly, the results obtained applying MEMLS approach are more reliable than in case of 245K algorithm when considering the period 1979 – 2019. When comparing with the PMW coarse-resolution dataset (25 km), we found that the melt extent timeseries derived from the PMW enhanced-resolution data using MEMLS better agree with MAR simulations than the ones obtained using the 25 km resolution data. After assessing the outputs of the PMW-based algorithms, we studied the melt onset date, melt end date, mean melt duration and maximum melting surface for the period 1979 – 2019. According to MEMLS algorithm, we found that the melting season has begun 0.404 (0.254) days earlier every year between 1979-2019 (1988-2019) and has ended 0.708 (0.396) days later every year between 1979-2019 (1988-2019). These values are averaged over the whole ice sheet and the trends are statistically significant at a 95% level (p-value¡0.05). The mean melt duration has increased every year by 0.451 d y^{-1} (0.291 d y^{-1}) during the period 1979-2019 (1988-2019). We found differences in trends computed using the PMW coarse-resolution with respect to the PMW enhanced-resolution data for the reference periods 1979 – 2012 and 1988 -2012, possibly because of the different rationale behind the melt detection algorithms and the higher level of detailing of the PMW enhanced-resolution dataset. When we performed a spatial analysis of the trends for the melt onset dates and duration, we found that the areas where the number of melting days has been increasing are mostly located in West Greenland. The maximum melting surface presents positive trends as well, with an increment of 0.69% (0.36%) every year respect to the Greenland ice sheet surface since 1979 (1988). Finally, we explored the information content of the PMW enhanced-resolution dataset with respect to the one at 25 km and the MAR outputs through a semi-variogram approach. The results obtained showed a better fitting of the modelled spherical function to the empirical semi-variogram in case of the enhanced-resolution data and MAR maps of melt duration. Our analysis suggests that the enhanced resolution product is sensitive to local scale processes, with higher sensitivity in case of MEMLS algorithm. This offers the opportunity to improve our understanding of the spatial scale of the processes driving melting and potentially paves the way for using this dataset in statistically downscaling model outputs. In this regard, as a future work, we plan to extend the analysis of spatial scales to the atmospheric drivers of surface melting, such as incoming solar radiation, surface temperature and longwave radiation and complement this analysis with our previous work focusing on understanding the changes in atmospheric patterns that have been promoting enhanced melting in Greenland over the recent decades (Tedesco and Fettweis, 2020). Assessed the capability of this dataset and method in observing temporal trends, a further development can include a combination of the PMW enhanced-resolution dataset with higher resolution satellite data (optical sensors or lower frequencies) in order to investigate the evolution of the surface meltwater networks and the application of similar tools to other regions, such as the Canadian Arctic Archipelago, the Himalayan Plateau and the Antarctic Peninsula, where the enhancement in spatial resolution can be fully exploited.

Chapter 5

A computationally efficient statistically downscaled 100 m resolution Greenland product from the regional climate model MAR

Everything is on a reduced scale here in the Polar regions; we can't afford to be extravagant.

R. Amundsen,
Sydpolen

Submitted:

Tedesco, M., Colosio, P., Fettweis, X., and Cervone, G.(2023). A computationally efficient statistically downscaled 100 m resolution Greenland product from the regional climate model MAR, The Cryosphere Discuss. [preprint], in review.

Abstract

The Greenland Ice Sheet (GrIS) has been contributing directly to sea level rise and this contribution is projected to accelerate over next decades. A crucial tool for studying the evolution surface mass loss (e.g., surface mass balance, SMB) consists of regional climate models (RCMs) which can provide current estimates and future projections of sea level rise associated with such losses. However, one of the main limitations of RCMs is the relatively coarse horizontal spatial resolution at which outputs are currently generated. Here, we report results concerning the statistical downscaling of the SMB modeled by the Modele Atmosphérique Regional (MAR) RCM from the original spatial resolution of 6 km to 100 m building on the relationship between elevation and mass losses in Greenland. To this goal, we developed a geospatial framework that allows the parallelization of the downscaling process, a crucial aspect to increase the computa-

tional efficiency of the algorithm. The results obtained in the case of the SMB, assessed through the comparison of the modeled outputs with in-situ SMB measurements, show a considerable improvement in the case of the downscaled product with respect to the original, coarse output. In the case of the downscaled MAR product, the coefficient of determination (R^2) increases from 0.868 for the original MAR output to 0.935 for the downscaled product. Moreover, the value of the slope and intercept of the linear regression fitting modeled and measured SMB values shifts from 0.865 for the original MAR to 1.015 for the downscaled product in the case of the intercept and from the value -235mm (original) to -57 mm (downscaled) in the case of the slope, considerably improving upon results previously published in the literature.

5.1 Introduction

The Greenland Ice Sheet (GrIS) has been contributing directly to sea level rise since the beginning of the century through meltwater runoff and ice mass loss. Hörhold et al. (2022) found that modern temperatures are 1.5 °C warmer than the twentieth century and that meltwater run-off, a major contributor to sea level rise, has been consequently enhanced. Surface melting has also been increasing since 1979, as measured by passive microwave satellite observations in terms of extension and persistency (e.g., Tedesco et al. 2013, Colosio et al., 2021). Moreover, Hanna et al. (2021) found that over the 1972-2018 period each 1°C of summer warming corresponds to 116 Gt of surface mass loss and 26 Gt of solid ice discharge increase. A key tool for studying the evolution surface mass loss (e.g., surface mass balance, SMB) over the GrIS is represented by (polar) regional climate models (RCMs), which, differently from remote sensing observations can provide information on the actual mass loss and represent an irreplaceable tool to provide future projections of such losses. A widely used model in this regard is the Modele Atmospherique Regional (MAR, Fettweis et al., 2013, 2017, 2020; Tedesco et al., 2013)., a coupled surface-atmospheric model forced at its boundaries with reanalysis data. However, one of the limitations of MAR (and of RCMs in general) lies in the horizontal spatial resolution at which outputs can be generated. This is due to computational considerations as well as to the physics behind the models. Currently, MAR simulations over Greenland are generated at a horizontal spatial resolution of 6 km (e.g., Colosio et al., 2021). Such spatial resolution guarantees a sufficiently fine mesh for ice-sheet-wide climatological studies, but it does not allow capturing fine-scale processes occurring in areas characterized by complex topography (e.g., glaciers terminating in fjords) or small glaciated surface (e.g., ice caps). Moreover, the knowledge of mass loss at a horizontal spatial resolution higher than the one currently available (e.g., 100s of meters) would allow to better constrain the relationships between the surface and sub-surface and englacial hydrological systems as well as would allow a better characterization of the meltwater fluxes into the ocean surrounding the GrIS.

To address the limitations associated to the current horizontal spatial resolution of the MAR model, statistical downscaling can be used to enhance the spatial resolution of the modeled outputs. For example, Hanna et al. (2005, 2008, 2011) statistically downscaled reanalysis data over the GrIS. A statistical downscaling technique based on elevation correction was also applied by Franco et al. (2012) to the 25 km MAR outputs to reconstruct GrIS SMB at 15 km spatial

resolution. Following that, Noël et al. (2016) applied an elevation dependent statistical downscaling technique to SMB components simulated by the Regional Atmospheric Climate Model (RACMO2) at 11 km resolution to reconstruct a daily dataset of SMB over the GrIS over a 1 km resolution grid. Here, we build upon the approach proposed by Noël et al. (2016) to generate a 100 m, statistically downscaled output of MAR SMB over the whole GrIS. Beside applying the approach to a different set of modeled outs (MAR instead of RACMO) and the enhanced spatial resolution with respect to Noël et al. (2016), we developed a geospatial framework that allows the parallelization of the downscaling process which increases the computational efficiency of the algorithm. In the following, we first describe the datasets used for our approach (Section 2), then we introduce the methodology (Section 3), followed by the results (Section 4) and our conclusions and future work (Section 5).

5.2 Datasets

5.2.1 MAR model

Modeled quantities to be downscaled are obtained from the regional climate model MAR (Colosio et al., 2021; Alexander et al., 2014; Fettweis et al., 2013; Fettweis et al., 2017; Tedesco et al., 2013). MAR is a modular atmospheric model that uses the sigma-vertical coordinate to simulate airflow over complex terrain and the Soil Ice Snow Vegetation Atmosphere Transfer scheme (SISVAT) (e.g., De Ridder and Gallee, 1998) as the surface model. The snow model in MAR, which is based on the CROCUS model of Brun et al. (1992), calculates albedo for snow and ice as a function of snow grain properties, which in turn depend on energy and mass fluxes within the snowpack. Lateral and lower boundary conditions are prescribed from reanalysis datasets. Sea-surface temperature and sea-ice cover are prescribed over ocean using the same reanalysis data. The atmospheric model within MAR interacts dynamically with SISVAT. MAR outputs have been assessed over the Greenland ice sheet by many authors (e.g., Fettweis et al., 2017, 2020; Alexander et al., 2014).
In this study, we use the output from MAR version v3.11.5 characterized by an enhanced computational efficiency and improved snow model parameters (Fettweis et al., 2020; Delhasse et al., 2020). The model is 6-hourly forced at the boundaries from 1950 using ERA5 reanalysis (Hersbach et al., 2020), the newest generation of global atmospheric reanalysis data that superseded ERA- Interim (Dee et al., 2011), and output is produced at a horizontal spatial resolution of 6 km. Specifically, we focus our attention on daily air temperature (TT variable), surface temperature (ST variable) and surface mass balance (SMB) outputs.

5.2.2 Digital Elevation Model

For the Digital Elevation Model (DEM), we adopt the ArcticDEM data product (Porter et al., 2018, Figure 5.1). ArcticDEM is a National Geospatial-Intelligence Agency (NGA) and National Science Foundation (NSF) public-private initiative to produce high-quality DEM of the Arctic applying stereo auto-correlation techniques to high-resolution optical satellite images and adopting the SETSM open-source photogrammetric software (Noh and Howat, 2015). Further

information about the dataset can be found at https://www.pgc.umn.edu/guides/arcticdem/introduction-to-arcticdem/. Specifically, we use a DEM provided at the spatial resolution of 100 m. The data are projected to the National Snow and Ice Data Center (NSIDC) Sea Ice Polar Stereographic North and referenced to WGS84 datum. The overall dataset is composed of 403,920,000 cells and is distributed as a GeoTIFF with a total size of approximately 1.6 Gb.

5.2.3 PROMICE Surface Mass Balance measurements

The main objective of this work is to obtain a high-resolution SMB dataset from the downscaling of the MAR model suitable for local (i.e., glacier scale) studies. Consequently, we carried out a validation of our results by comparing the original SMB outputs from MAR at a spatial resolution of 6 km and the downscale outputs at 100 m with in-situ SMB measurements. For this purpose, we used the dataset collected by Machguth et al. (2016), containing 2955 measurements from 46 sites, reported in Figure 5.1 as blue dots. The dataset is available on GEUS Dataverse portal (Machguth, 2022; last access 16/02/2023). Such comprehensive dataset spans from 1892 to 2015. From the 123 years, we focused our attention to the period 1980 - 2015 when the largest portion of the dataset is temporally located and the MAR outputs are available. From the 2955 measurements we obtained 1982 suitable SMB measurements to be used for validation. The SMB measurements are carried out by computing the difference of stake readings between two dates. The observations are identified by the measuring site (i.e., the area or location, containing at least one measuring point), measuring pint (i.e., specific stakes, associated with multiple readings) and the actual readings (i.e., the SMB measurement). In Table 5.1 we report the number of readings for each measuring site considered, together with its coordinates (WGS 84) and time period when the measurements were collected. Measurement periods are various, covering specific seasons (summer or winter SMB) or an entire year (annual SMB). In some cases, also short-term (at least one month) and multi-year measurements are present. We reconstructed the SMB in correspondence of the measurement location as algebraic sum of the daily simulated SMB between the start and end dates of the measurement. In order, as a metric to assess the performance of the downscaled product, we compute the root mean squared error (RMSE) and the least-square linear regression parameters (slope and intercept) between model outputs (SMB variable, original and downscaled) and measurements.

5.2.4 GC-Net air temperature

To test the results of the applied downscaling procedure at local scale we also compare the values of surface temperature obtained from MAR with in-situ measurements. We use data from the Greenland Climate Network (GC-Net; Steffen et al., 1996), a set of Automatic Weather Stations (AWS) located all around the Greenland ice sheet and continuously measuring air temperature, wind speed, wind direction, humidity, pressure, and other parameters. Since direct measurements of surface temperature are not available as continuous records at multiple sites around Greenland, we use the air temperature records measured at 3 m above ground level. Specifically, we consider 17 selected stations reported in Figure 5.1 as red triangles. Specific location and elevation for each station are also reported in Table 2 in the Results section. The AWS thermometers collect air temperature measurements at sub-daily temporal scale while

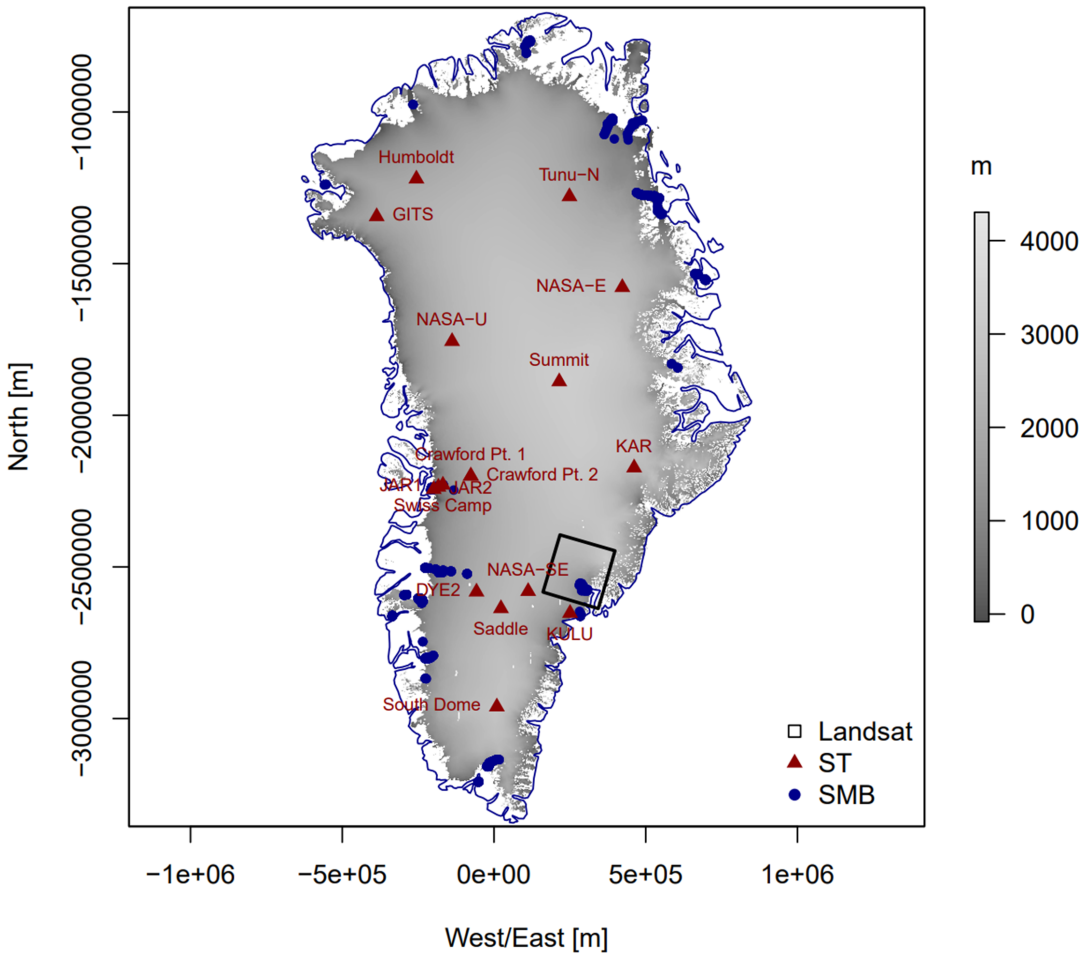

Figure 5.1: Map of Greenland ice sheet. The digital elevation model (DEM) at 100 m resolution is represented in greyscale, the GC-Net air temperature locations are plotted as red triangles and the PROMICE surface mass balance measurements locations are reported as blue dots.

MAR outputs are provided at daily temporal resolution. Consequently, we compute daily average air temperatures for the comparison with the modelled and downscaled near-surface temperatures (TT variable).

5.2.5 Landsat-8 surface temperature

As in situ measurements are only available at point scale, it is not possible to assess the potential improvement of the downscaling approach on spatially distributed fields. In the absence of spatially distributed, high spatial resolution SMB outputs, we use seven different Landsat-8 scenes covering the Jakobshavn and the Helheim Glaciers, acquired on 5 June 2015, 30 June 2015 (two images), 9 July 2015 (two images), 16 July 2015, and 18 July 2015. The Landsat-8 surface temperature product is available at 30 m spatial resolution since April 2013 and is generated from Landsat Collection 2 Level-1 thermal infrared bands and other parameters obtained from satellite observations and reanalysis data. The images were downloaded from the USGS Earth Explorer data portal (https://earthexplorer.usgs.gov/, last access 17/01/2023).

ID	Glacier/Site name	Latitude [°]	Longitude [°]	Measurement years	Points	Readings
126	Qaanaaq Ice cap	77° 30' 36" N	69° 9' 0" W	2012-2015	6	12
128	Petermann	80° 41' 2" N	60° 17' 35" W	2002-2013	2	4
130	Hans Tausen Ice Cap	82° 29' 24"	37° 30' 0" W	1995 and earlier	5	13
140	Hare Glacier	82° 50' 24" N	36° 40' 12" W	1994-95	29	62
170	Kronprins Christian Land	79° 46' 48" N	25° 11' 24" W	1993-1994, 2008-2013	20	62
180	Nioghalfvjerdsfjorden	79° 30' 0" N	21° 36' 0" W	1996-1997	13	13
215	Storstrømmen	77° 30' 0" N	23° 0' 0" W	1989-1994	22	113
220	A.P. Olsen Ice Cap	74° 38' 24" N	21° 26' 60" W	2008-2013	17	56
230	Freya Glacier	74° 22' 48" N	20° 49' 12" W	2008-2013	29	93
232	Violin Glacier	72° 20' 60" N	26° 58' 48" W	2008-2013	2	12
254	Helheim	66° 24' 36" N	38° 20' 24" W	2008-2010	21	118
270	Isertoq	65° 42' 0" N	38° 53' 24" W	2007-2013	2	15
315	Nordbo Glacier	61° 30' 0" N	45° 22' 12" W	1977-83	41	200
412	Isortuarssup Sermia	63° 47' 60" N	49° 47' 60" W	1983-1988	3	9
414	Qamanarssup Sermia	64° 30' 0" N	49° 23' 60" W	1979-1988, 2007-2013	20	164
416	Kangilinnguata Sermia	64° 52' 48" N	49° 17' 60" W	2010-2013	1	3
420	Qapiarfiup	65° 34' 48" N	52° 12' 36" W	1980-1989	5	75
440	Amitsuloq Ice Cap	66° 8' 24" N	50° 19' 12" W	1981-1990	26	422
450	Tasersiaq	66° 15' 36" N	51° 23' 60" W	1982-1989	6	111
454	K-Transect	67° 5' 60" N	48° 51' 36" W	1990-2013	11	193
456	Paakitsoq, JAR	69° 29' 24" N	49°51' 36" W	1982-1992, 1996-2013	22	220
458	Swiss Camp/ST2	69° 33' 53" N	49° 19' 51" W	1990-2014	2	12

Table 5.1: PROMICE surface mass balance measurements information for the selected Glaciers and measurements sites.

We compared the Landsat-8 observations with the original and downscaled MAR outputs of surface temperature (ST variable).

5.3 Methods

5.3.1 Downscaling methodology

We adopted the methodology proposed by Noël et al. (2016) applied to the MAR regional climate model (instead of RACMO). Differently from Noël et al. (2016), however, we push the horizontal resolution of the downscaled product to 100m (instead of 1 Km). The method exploits the potential dependency of the modelled variables (e.g., surface temperature, runoff) with elevation. In order, to overcome the large number of cells and reduce the computational time, we parallelized the procedure through a combination of geospatial tools (in the software R) so that our approach can also be used for near-real time generation of downscaled maps over

a specific region of the Greenland ice sheet.
The first step involves the calculation of the local dependency of the MAR outputs with respect to the elevation. For this step we refer to the methodology proposed by Noël et al. (2016). Accordingly, we compute the local linear regression (least squares) between the specific variable and the elevation (obtained from the MAR DEM) obtaining the values of slope (m_{6km}) and intercept (q_{6km}). The linear regression is carried out for each pixel of the MAR 6 km resolution DEM using the values of the adjacent pixels with a minimum of 6 points used for the regression. In the case of pixels with less than 5 adjacent pixels, we compute m and q for that pixel by interpolation. Such regression is carried out for every day and pixel of the region of interest. Figure 5.2 provides an example of such procedure. The local linear regression sample consists of the red pixel (5) and the surrounding green pixels (1,2,3,4,6,7,8 and 9), for a total of 9 pixels (Figure 5.2a). The dashed red line in Figure 5.2b represents the linear regression curve obtained fitting the numbered points. Parallelizing such procedure for each MAR pixel, we obtain the daily maps of m_{6km} and q_{6km} for the considered MAR output variable. Then, the m_{6km} and q_{6km} maps are reprojected to the Polar Stereographic coordinate system which is used by the DEM. The original MAR data are distributed by providing only the coordinates for the centre of each grid cell. To create a continuous grid, and avoid introducing errors, the coordinates for the four corners of each MAR grid are computed, and then they are transformed into the Polar Stereographic coordinate system. The result is a shapefile that contains a polygon for each MAR grid. Additionally, the new shapefile contains metadata to ease computations, such as a unique MAR grid ID, the Polar Stereographic coordinates for the centre of the grid, the corresponding coordinates in longitude and latitudes for the centre of the grid. The next step consists in fragmenting the high-resolution DEM into a series of smaller files, specifically one for each polygon of the reprojected MAR cells generated in the previous steps. There are a total of 55,144 files generated through each step, which are less than the total number of cells in the original MAR output. This discrepancy is due to the fact that the DEM is limited to only areas covered by the ice sheet, and it thus does not cover all the locations of where MAR output is generated. While it might seem counterintuitive that maintaining over 55,000 small files is more efficient than maintaining a single file, the answer lies in the fact that this pre-processing step enables the downscaling to be an embarrassingly parallel problem which can be efficiently solved using multi-core and multi-node infrastructure. Because the DEM is required for downscaling each grid cell, which are computed simultaneously in parallel, each task needs to read only a small file of a few kb, rather than one larger file, and it also avoids file system bottlenecks when multiple processes try accessing the same file. Most file systems do not allow for concurrent access to the same file, and therefore if hundreds of tasks try to read the same file, each task would have to idle in a queue for the file access to become available. This problem is prevented by generating a DEM file for each MAR grid, so that both I/O transfer rate and file access are optimized. Furthermore, because the DEM are segmented using the original Polar Stereographic projection, which matches the reprojected MAR grid, no further transformation is required, further speeding up the downscaling process. The final step consists in obtaining the high-resolution maps of slope and intercept (m_{100m} and q_{100m}) by bilinear interpolation of m_{6km} and q_{6km} over the high-resolution DEM grid. While this process was not

parallelized in the current version, it is possible to speed it up using a parallel solution. Finally, the downscaled variable is obtained by applying the high-resolution linear regression coefficients to the high-resolution DEM as

$$VAR_{100m} = m_{100m} H_{100m} + q_{100m} \tag{5.1}$$

where VAR is the generic downscaled variable computed as linear function of high-resolution elevation of the DEM (H_{100m}) through the coefficients previously obtained (m_{100m} and q_{100m}). In Figure 5.2a, we show a random ensemble of points of the 100 m grid (black dots within the red pixel) around the high-resolution pixel centred in the original MAR grid (blue dot). The values of the downscaled variable (in this example surface temperature) of such points are reported as grey dots (blue for the central pixel) in Figure 5.2b, distributed along the linear regression curve. Since the origin of the MAR DEM and the high-resolution DEM is different, errors in terms of mass conservation can arise. For example, within a MAR pixel the average elevation of the high-resolution DEM might be higher than the original MAR elevation, possibly leading to the previously mentioned mass conservation error (e.g., the original MAR pixel suggests for a day a lower mass loss than the ensemble of the high-resolution pixels). For this reason, differently from Noël et al. (2016), we decided to provide physical constrains to be satisfied as very final step of the downscaling procedure.
In this research, we apply the downscaling methodology to daily near-surface temperature (TT), surface temperature (ST) and SMB MAR outputs.

5.3.2 Spatial autocorrelation analysis and variograms

Beside RMSE and slop and intercept, we also focus on evaluating the potential improvements of the downscaled product with respect to the original coarser resolution MAR outputs in terms of capability to describe the spatial distribution of the considered variable. To this aim, we perform a spatial autocorrelation analysis using variograms. Variogram analysis is generally adopted in geostatistical analyses to evaluate autocorrelation of spatial data (Edward et al., 1989). Autocorrelation and variogram analysis are geostatistical tools that can be used to quantify spatial variability using metrics such as the spatial correlation length (simply correlation length hereafter). Though these techniques were mainly designed to support the prediction of values at locations where measurements are not available, they can be used for characterizing processes across the scale spectrum (Herzfeld, 1993). Once process scales are known, the scale ranges over which process relationships (and thus spatial pattern) are consistent must be determined. The knowledge of these scaling ranges will identify scales at which the process interactions change, being such scales critical for measurement or model interests (Mark and Aronson, 1984; Vedyushkin, 1994). Geostatistical methods such as spatial covariance, variogram analysis, and spectral analysis (Webster and Oliver, 2001) quantify the spatial pattern of variability of an observed property over a scale range from the minimum sample separation to the distance at which the variable becomes spatially independent. This quantified variability can, then, be used for spatial estimation based on a finite number of data points. In geostatistical approaches, spatial variation is treated as having both deterministic and stochastic components, with the determin-

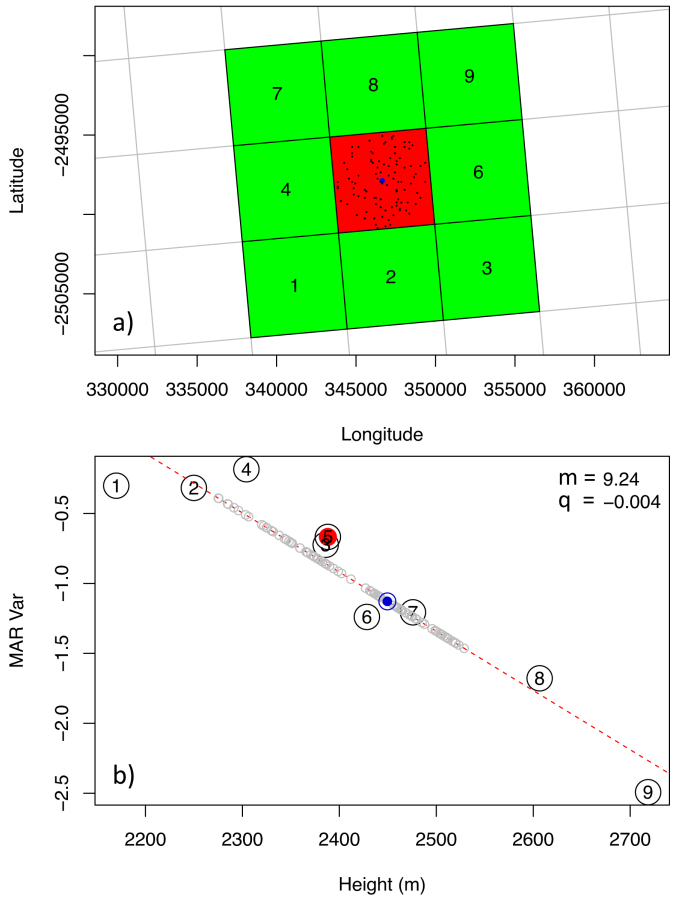

Figure 5.2: Elevation downscaling procedure example for a generic variable. In panel (a) the considered MAR pixel (red) and the surrounding pixels (green) adopted for the local linear regression are represented. In panel (b) the variable value of each considered pixel is reported as numbered circle. The dashed red line represents the linear regression computed for such pixels and the grey circles represent the downscaled variable for a group of 100 m pixels randomly picked within the considered MAR pixel.

istic component modeled using a trend surface, for example, while the stochastic component modeled as random deviations from that surface, whose spatial structure can be characterized by the variogram (Webster and Oliver, 2001). In this specific case, we fit the experimental variogram with a circular model, as it has shown to be the one that provides the highest R2 when fitting the experimental data. The experimental variogram is computed as

$$\gamma(\delta) = \frac{1}{2N(\delta)} \sum_{i,j \in N(\delta)} (x_i - x_j)^2 \tag{5.2}$$

where γ is the semi-variance, $N(\delta)$ is the number of data pairs (i-th and j-th) distanced by δ while x_i and x_j are the corresponding variable values. The fitting spherical function is, then, used to compute the three main parameters characterizing the variogram: the sill, the range and the nugget effect. The sill is defined as the maximum value at which the fitted curve becomes flat; such variance value is reached at a certain distance called range, beyond which the data are no longer autocorrelated. The nugget corresponds to $\gamma(0)$ and it is a result of

measurement errors or highly localized variability. Here, following Colosio et al. (2021), we focus our attention on the range, the descriptor of the correlation length, comparing the range values computed for the original MAR temperature outputs, the downscaled temperature and the surface temperature observed by Landsat-8.
To further investigate and quantify possible improvements in terms of spatial description of the variable of interest by th downscaled product, we also compute the so-called Structural Similarity Index Measure (SSIM). Such index has been introduced by Wang et al. (2004) to provide a similarity measure between two images. This index can objectively quantify a qualitative aspect such the similarity between two images. Considering a pair of images (X, Y) to be compared, the values assumed by the SSIM are bounded by a unique maximum ($SSIM(X, Y) = 1$) in case $X = Y$, otherwise $SSIM(X, Y) < 1$. We compute such similarity index for both original and downscaled MAR ST outputs, considering as reference the Landsat-8 surface temperature image.

5.4 Results and discussion

5.4.1 Surface and near-surface temperature

We first tested the downscaling algorithm with the MAR near-surface temperature outputs. We compared the results obtained with air temperature measurements from 17 AWS of the GC-Net. We performed the comparison by computing RMSE and R^2 between the modelled (original and downscaled) and the observed variable. The results obtained for the original MAR and the downscaled temperatures are reported in Table 2. Both R^2 and RMSE obtained for the downscaled temperatures do not exhibit significant improvements or worsening with respect to the original coarser resolution output. The difference between the 6 km and 100 m resolution is in the order 10^{-3} for R^2 and 10^{-2} °C for RMSE, with improvements in some stations (Swiss Camp, Crawford Pt. 1, NASA-U, Summit, Crawford Pt. 2, KAR, JAR2 and KULU) and worsening in others (Tunu-N, JAR1, South Dome and NASA-E). However, such small differences appear to be randomly distributed in space, without any clear correlation with elevation or latitude/longitude. Such results demonstrate that the applied downscaling methodology does not introduce errors in case of the TT variable at point scale.

To evaluate the results over a wider area, we considered two Landsat-8 surface temperature images collected over two different areas of the ice sheet. The two selected areas are located on the eastern and western coasts of Greenland and show a variable topography. In Figure 5.3 we report the surface temperature image from Landsat-8 (Figure 5.3a), the original ST output at 6 km spatial resolution (Figure 5.3b) and the downscaled ST at 100 m resolution (Figure 5.3c) for one of the selected Landsat-8 scenes. We compare the original MAR and downscaled high-resolution ST by computing the difference of these maps with the Landsat-8 image for the sole pixels common to all three maps. In Figure 5.4 we report the histograms of the difference between Landsat-8 surface temperature and the original ST (Figure 5.4a) and the downscaled one (Figure 5.4b) for the same image. The results show no differences in terms of mean difference (μ), with an average difference of 2.7°C in both cases, similarly to the AWS comparison.

Station	**Latitude** [°]	**Longitude** [°]	**Elevation** [m]	$\mathbf{R^2}$ **6km**	$\mathbf{R^2}$ **100m**	**RMSE 6km**	**RMSE 100m**
Swiss Camp	69° 34' 06"	49° 18' 57"	1149	0.945	0.945	2.37	2.36
Crawford Pt.1	69° 52' 47"	46° 59' 12"	2022	0.872	0.873	3.95	3.95
NASA-U	73° 50' 31"	49° 29' 54"	2369	0.788	0.789	5.35	5.34
GITS	77° 08' 16"	61° 02' 28"	1887	0.915	0.915	3.4	3.4
Humboldt	78° 31' 36"	56° 49' 50"	1995	0.801	0.801	5.64	5.64
Summit	72° 34' 47"	38° 30' 16"	3254	0.837	0.84	4.62	4.58
Tunu-N	78° 01' 0"	33° 59' 38"	2113	0.937	0.936	3.17	3.2
DYE2	66° 28' 48"	46° 16' 44"	2165	0.94	0.94	2.72	2.72
JAR1	69° 29' 54"	49° 40' 54"	962	0.787	0.786	4.37	4.38
Saddle	66° 00' 02"	44° 30' 05"	2559	0.935	0.935	2.77	2.77
South Dome	63° 08' 56"	44° 49' 00"	2922	0.915	0.915	2.76	2.77
NASA-E	75° 00' 00"	29° 59' 59"	2631	0.882	0.881	3.94	3.97
Crawford Pt.2	69° 54' 48"	46° 51' 17"	1990	0.893	0.894	3.62	3.61
NASA-SE	66° 28' 47"	42°30' 00"	2425	0.86	0.86	3.83	3.83
KAR	69° 41' 58"	33° 00' 21"	2579	0.935	0.936	2.6	2.57
JAR2	69º 25' 12"	50º 03' 27"	568	0.706	0.709	4.79	4.76
KULU	65° 45' 30"	39° 36' 06"	878	0.59	0.595	5.22	5.19

Table 5.2: Root-mean-square error and R^2 computed comparing MAR_{6km} and MAR_{100m} with air temperature measurements from the GC-Net considered stations. Longitude, latitude and elevation of the station are also reported.

Also, the standard deviation (σ) remains unvaried, being equal to 2.6°C. Similar results have been obtained for all the compared Landsat-8 images, with mean differences ranging between -0.59°C and 3.44°C for the downscaled product (2.09°C on average) and between -0.62°C and 3.43°C for the original MAR data (2.07°C on average). We expected a similar result in terms of average difference considering the physical constrain imposed for the ST to maintain the average ST constant for each MAR pixel as final step of the downscaling procedure. These results indicate that in case of ST the downscaling algorithm does not introduce significant improvements or errors in terms of overall difference with observed temperature (expressed as RMSE for the AWS case and spatial average difference for the Landsat-8 image).

Considering such results in terms of difference at point scale and spatially averaged difference, we evaluated possible improvements in terms of spatial information content and spatial description obtained in the downscaled product. We report in Figure 5.5 the results of the semi-variogram analysis performed for two sub-regions of interest within the same Landsat-8 image shown in Figure 5.3. The two areas have been selected because of the strong differences in topography and elevation gradients. Concerning the results obtained over the topographically more complex area, we observe that the scale break of the downscaled temperature (blue line) is 13.5 km, better capturing the one from Landsat-8 data (11.5 km, red line) with respect to the original MAR outputs (24.1 km, black line). On the other hand, the same analysis performed over an area in a more interior region of the ice sheet, where downscaling might lead to less improvement in view of the reduced topography, does not present improvements in terms of spatial autocorrelation (Figure 5.5b) and that all three datasets do not reach the semi-variogram

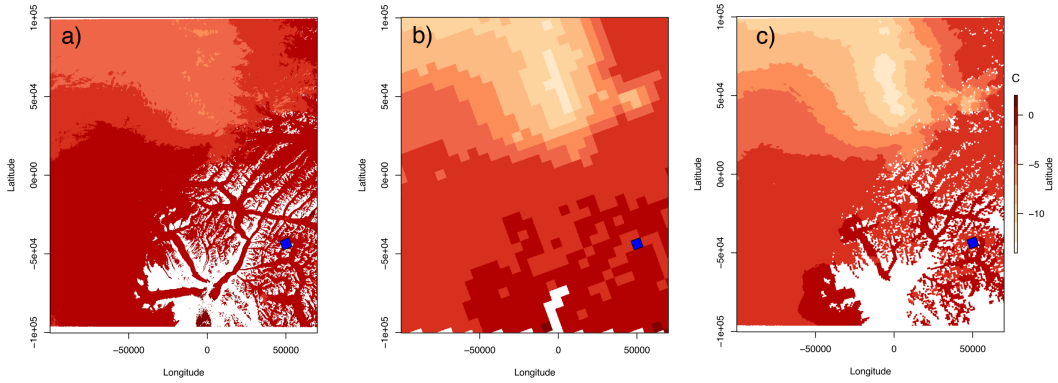

Figure 5.3: Maps of temperature from (a) Landsat-8, (b) MAR_{6km} and (c) MAR_{100m} over the area covered by the Landsat 8 selected image on 30 June 2015. The blue dot reported to every map represents the 6 km pixel of the original MAR grid reported in red in Figure 5.2a.

plateau within the considered distance.

In order to extend the comparison to another area of the ice sheet, we performed the same variogram based analysis for another Landsat-8 scene in the surroundings of Jakobshavn glacier collected on 11 June (Figure 5.6a). The map also shows the two regions of interests (ROI) selected for the analysis. We selected ROI_1 as this area is characterized by a large topographic gradient within a relatively small distance and to understand the potential improvement of the downscaling procedure over regions that are outside the main ice sheet (e.g., smaller glaciers). On the other hand, ROI_2 contains both strong and mild elevation gradients (e.g., nunataks and ice sheet elevation gently increasing as moving towards the interior). This area is covered by most of its portion containing the ice sheet (right portion of ROI_2) by the DEM, being this absent in the case of the left portion of the ROI, where fjords and ocean features are dominating. In case of ROI1 (Figure 5.6b), the variogram analysis indicates that the break scale distance for Landsat-8 when considering only the pixels where the DEM is available is 7.5 km. This value becomes 14.6 km for the high-resolution map of ST and 24.7 km in the case of the original MAR outputs, suggesting that the downscaled product is able to perform better than the original one in terms of spatial scale similarity with respect to the Landsat-8 data. The mean difference between Landsat-8 and the downscaled (original MAR) surface temperature, considering only the pixels where the DEM is available, are 1.69°C (1.7°C) with a standard deviation of 2.02°C (2.14°C), with differences of the same order of magnitude obtained in the previous analysis for the other Landsat-8 image. When considering all pixels within the ROI (e.g., also where no DEM is available), the mean differences between Landsat-8 and downscaled (original) MAR surface temperature become 1.89°C (2.12°C) with a standard deviation of 2.15°C (2.23°C). In this case, the scale breaks for the original and the downscaled MAR versions are similar, ∼25 km (∼16km in the case of Landsat-8). We point out that the scale breaks are sensitive to the different physical processes driving the spatial properties. The ROI_2 contains both strong and mild elevation gradients given the presence of nunataks and the slow ice sheet increasing elevation after the ice cliff begins. The area is covered by most of its portion containing the ice sheet (right of the image) by the DEM, which, however, is absent in the case of the left portion

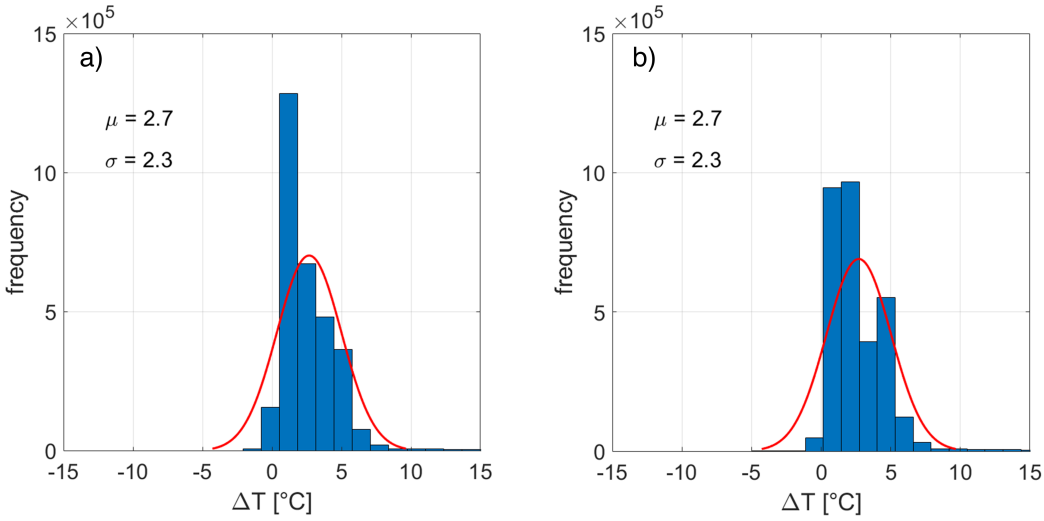

Figure 5.4: Histograms of the difference (a) between the 6 km MAR temperature and Landsat-8 temperature and (b) between 100 m MAR temperature and Landsat-8 temperature.

of the ROI, containing fjords and the ocean. The scale breaks for the Landsat-8, downscaled and original MAR cases for the portion of the ROI_2 where the DEM is available are close to each other, on the order of ∼25 km. We observe an improvement in the SSIM in the case of the downscaled data by 30% (from 0.33 in the case of the original MAR resolution to 0.43 in the case of downscaled MAR). Also, despite as expected the mean and standard deviation of the distribution of the differences between the Landsat-8 data and the simulated quantities remains similar, we notice a reduction in both the mean (from 0.86ºC for original MAR to 0.83ºC for the downscaled product) and of the standard deviation (from 0.71ºC for original MAR to 0.63ºC for the downscaled product) when downscaling the MAR output. We further note that when considering all pixels (including those where no DEM), the SSIM of the two products improves from 0.11 (original) and 0.14 (downscaled) and that the scale break of the original MAR products is larger (∼63km) than the one of the Landsat-8 data (∼21 km). In synthesis, the downscaling does not introduce any considerable bias on the original value, preserves the total integrated quantity of energy within each area and improves, from a quantitatively point of view, the spatial performance of the MAR outputs by generating a product that has a spatial structure that is closer to the one of the observed remote sensing dataset.

5.4.2 Surface Mass Balance

After applying the downscaling algorithm to surface temperature, we applied it to MAR SMB outputs of SMB and assessed the results obtained with in situ measurements from the dataset collected by Machguth et al. (2016). As mentioned, we compared 1982 SMB measurements carried out between 1980 and 2015 and localized in the ablation area of the GrIS (Table 5.1). Figure 5.7 shows the scatterplots of the comparison of modelled SMB from the original MAR (Figure 5.7a) and the downscaled product (Figure 5.7b) with in situ measured SMB. Our results show that the downscaled product better estimates the measured SMB, exhibiting an

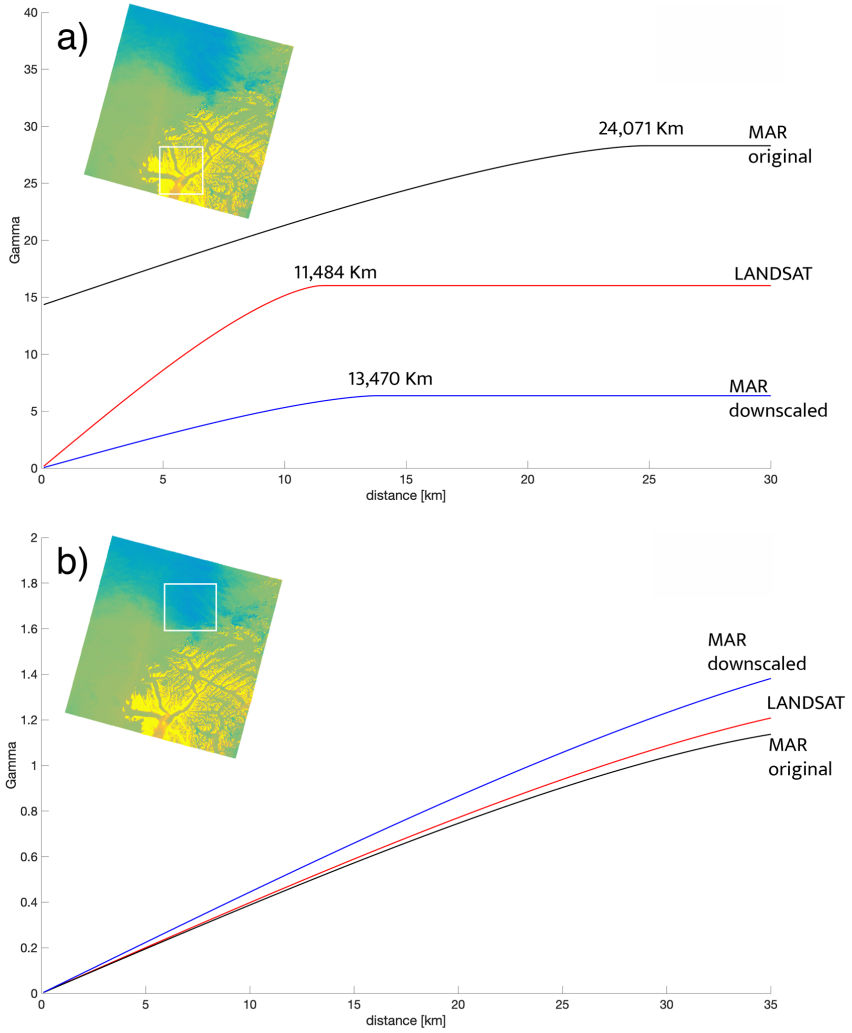

Figure 5.5: Modelled semi variograms for the Landsat-8, MAR_{6km} and MAR_{100m} computed over two regions of interest reported in the inset.

increased R^2 from an already relatively high value of 0.868 for the original MAR to 0.935 for the downscaled product. As a comparison, Noël et al. (2016) obtained an increase of R^2 from the downscaling of SMB outputs of the RACMO regional climate model from 0.47 in the case of the original 11 km spatial resolution outputs to 0.78 in case of the downscaled SMB (1 km resolution). We point out that, in our case, the starting value of R^2 for the original MAR product already exceeds the value obtained in the case of the downscaled RACMO outputs.

The values of slope and intercept of the best-fitting line improve as well when considering the downscaled product. The value of the slope shifts from 0.865 for the original MAR to 1.015 for the downscaled product; similarly, the intercept increases from the value -235 mm of the coarse resolution outputs to -57 mm of the downscaled SMB, closer to its optimal value (i.e., null intercept). As a comparison, the downscaling algorithm of Noël et al. (2016) applied to RACMO improved the estimate of SMB in terms slope from 0.72 to 1.03, with a slight increase of the intercept (from 70 mm to 100 mm). The RMSE between modelled and measured SMB

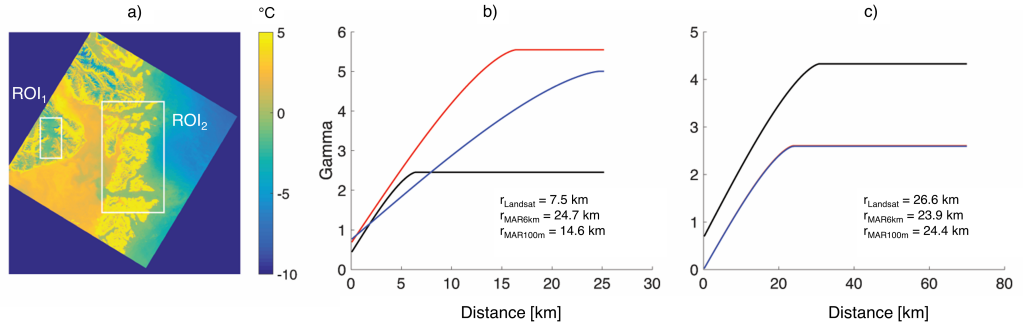

Figure 5.6: (a) Landsat-8 temperature captured on 11 June 2015 over areas around the Jakobshavn Glacier and (b, c) modelled semi variograms for the Landsat-8, MAR_{6km} and MAR_{100m} computed over (b) the first region of interest (ROI1) and (b) the second region of interest (ROI2).

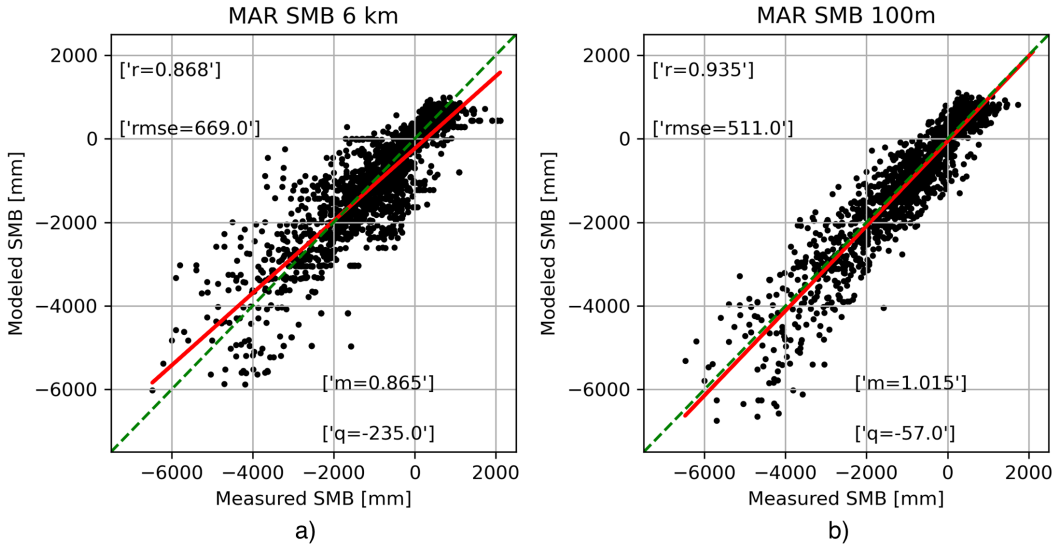

Figure 5.7: Comparison between measured and modelled surface mass balance from (a) original 6 km MAR and (b) downscaled 100 m MAR.

also decreases in the case of the downscaled product from 669 mm for the 6 km outputs to 511 mm for the 100 m case, significantly improving the estimate of SMB at local scale. Noël et al. (2016) obtained a reduction of the RMSE passing from a value of 1200 mm for the 11 km RACMO outputs to a value of 740 mm for the 1 km case. Fettweis et al. (2020) compared MAR and RACMO, among 13 models of four types (positive degree day models, energy balance models, regional climate models and general circulation models), SMB estimates with the same PROMICE in situ measurements within the GrIS SMB model intercomparison project (GrSMBMIP). They considered only the measurements collected between 1980 and 2012 and with measurement period longer than 3 months. They also excluded the records located outside the 1 km ice mask they used for the intercomparison of the models, for a total of 1438 SMB measurements. The model versions in this case are MARv3.9.6, an older version than the one we adopted and at the spatial resolution of 15 km, and RACMO2.3p2 (Noël et al., 2019), a new version of the one adopted in Noël et al. (2016) and with a spatial resolution of 5.5 km.

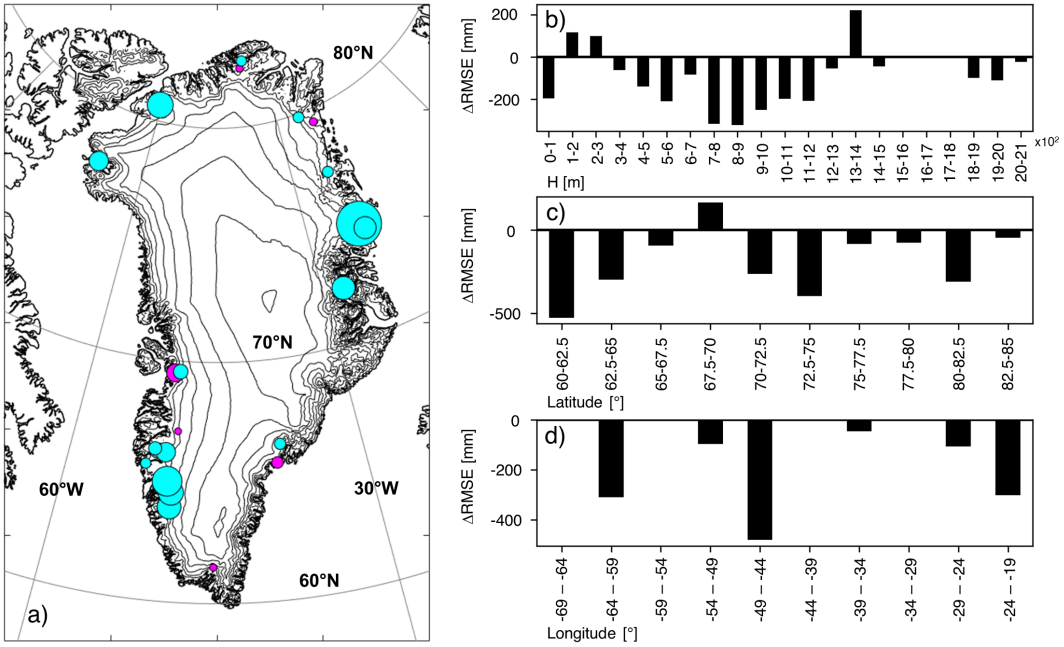

Figure 5.8: Difference between original and downscaled MAR modelled surface mass balance RMSE with respect to the measured surface mass balance data (RMSE100m-RMSE6km) by (a) glacier, (b) elevation, (c) latitude and (d) longitude. In the bubble chart map the contour lines are plotted every 500 m (original MAR6 km DEM), positive values (worsening) of $\Delta RMSE$ are reported in magenta while negative values (improvement) in cyan.

From the comparison, they obtained a RMSE of 480 mm for MAR and 630 mm for RACMO. In both cases, the RMSE is lower than the one obtained in this work for MAR (both original and downscaled) and by Noël et al. (2016) for RACMO. The difference can be related to the differences in spatial resolution and model versions and, most probably, to the sub-sampling of the SMB measurements discarding short-term records (i.e., measurement period lower than 3 months), suggesting that the bias might be dissipated for longer observation periods.

To further investigate our results, we compute the variation in RMSE between the 6 km spatial resolution MAR outputs and the downscaled product for different elevation classes, longitude and latitude ranges and for each specific glacier/location (i.e., for each station ID, Table 5.1) of the PROMICE in situ SMB dataset. The RMSE difference is computed as $\Delta RMSE = RMSE_{6km} - RMSE_{100m}$ (i.e., improvements are characterized by negative values of $\Delta RMSE$) and the results obtained are reported in Figure 5.8 grouped by location (Figure 5.8a), elevation (Figure 5.8b), latitude (Figure 5.8c) and longitude (Figure 5.8d). The results exhibit improvements in the estimate of SMB at all the altitudes besides the 100-200 m asl, 200-300 m asl and 1300-1400 m asl elevation classes, with the best performance obtained at 700-800 m asl and 800-900 m asl elevation classes. The results grouped by latitudinal bands show the highest improvements in south Greenland; a decrease in performance has been recorded in the latitudinal band 67.5-70 °N where the only Paakitsoq JAR ($\Delta RMSE$= 181 mm, worst result obtained) and Swiss Camp/ST2 ($\Delta RMSE$= -127 mm) measurement sites are located, and the improvement obtained in case of Swiss Camp is strongly counterbalanced by the reduced performances in Paakitsoq JAR. However, the longitudinal classes do not present

any decrease of the performances, indicating that the worsening in the spotted critical stations is counterbalanced by the improvements measured in the others. We obtained a decrease in performances in 6 out of 22 considered cases with the worst result obtained for the already presented Paakitsoq JAR case. In the 5 other cases (i.e., Hans Tausen Ice Cap, Nioghalfvjerdsfjorden, Isertoq, Nordbo Glacier and K-Transect) we recorded an average $\Delta RMSE$ of 26 mm (ranging from 6 mm to 80 mm). On the other hand, we obtained an improvement in 16 out of 22 measurement sites with the best performances in case of A.P. Olsen Ice Cap ($\Delta RMSE$= -611 mm). In the other 15 cases (i.e., Qaanaaq Ice Cap, Petermann, Hare Glacier, Kronprins Chistian Land, Storstrømmen, Freya Glacier, Violin Glacier, Helheim, Isortuarssup Sermia, Qamanarssup Sermia, Kangilinnguata Sermia, Qapiarfiup, Amitsuloq Ice Cap, Tasersiaq and Swiss Camp/ST2) we found an average decrease in RMSE of 183 mm (ranging between 59 mm and 371 mm). Even if such reduction of performances in terms of SMB estimate accounts for 27% of the considered stations, it does not compromise the overall improvement, being smaller in terms of average, minimum and maximum absolute values of $\Delta RMSE$ than the results obtained for the stations were improvement occurred.

5.5 Conclusions and future work

We applied a statistical downscaling technique to increase the horizontal spatial resolution of the outputs of the MAR regional climate model from 6 km to 100 m for the surface temperature and SMB quantities. The approach builds on the dependency of such quantities on elevation, as originally proposed in Noël et al. (2016). Here, however, the technique was applied to the output of a different climate model (RACMO) and the spatial resolution of the downscaled product was 1 km, rather than 100 m. Moreover, differently from Noël et al. (2016), we imposed a mass conservation so that the overall mass obtained for each pixel at high resolution nested within a coarse resolution one is preserved. To address the computational issues associated with the relatively high spatial resolution, we developed a geospatial, parallelized framework that allows to perform the downscaling over the whole ice sheet in an efficient way.

We, first, tested our approach by applying it to surface and near-surface temperature data and assess the outputs using both in-situ ad satellite data. Our results showed no significant improvement nor deterioration of the downscaled product with respect to the original MAR outputs. This confirms that our approach was not introducing any bias and was properly implemented. However, we found improvement of the downscaled surface temperature when analyzing the skills of the downscaled product to capture the spatial scales (e.g., scale breaks) of the observed surface temperature fields. The results obtained in the case of the SMB, assessed through the comparison of the modeled outputs with in-situ SMB measurements, show a considerable improvement in the case of the downscaled product with respect to the original, coarse output, evaluated through the analysis of the RMSE, R^2 and the slope and intercept of the modeled vs. measured values. In the case of the downscaled MAR product, the R2 value increases from 0.868 for the original MAR to 0.935 for the downscaled product with the value of the slope and intercept shifting from 0.865 for the original MAR to 1.015 for the downscaled product in the case of the intercept and from the value -235 mm of the coarse resolution outputs

to -57 mm of the downscaled SMB in the case of the slope. As a reference, Noël et al. (2016) obtained an increase of R^2 from the downscaling of SMB outputs of the RACMO regional climate model from 0.47 in the case of the original 11 km spatial resolution outputs to 0.78 in case of the downscaled SMB (1 km resolution) and a shift in the slope and intercept from 0.72 to 1.03 (slope) and from 70 mm to 100 mm (intercept). An analysis of the performance of the downscaled product for different elevation classes, longitude, and latitude ranges and for each specific glacier/location where SMB in-situ data is available shows that for 27% of the stations, the downscaled product does not perform as expected. However, this does not compromise the overall improvement, being the deterioration of the performance smaller in terms of average, minimum and maximum absolute values of $\Delta RMSE$ than the results obtained for the stations were improvement occurred.

The next step is to implement a similar approach for downscaling MAR outputs over both the Greenland and Antarctica ice sheet using machine learning (ML) based approaches. Indeed, the approach here proposed cannot be easily extended to Antarctica, where surface melting does not exhibit a strong dependency from elevation, as most of it occurs over ice shelves, at the sea level and where little elevation gradients exist. Moreover, improvements to the downscaling of the SMB can be obtained by either considering complementary inputs that can improve estimates of losses (e.g., remotely sensed albedo) or of mass gains (e.g., accumulation). ML tools can help in this regard. ML tools have, indeed, been used for improving predictions beyond that of state-of-the-art physical models or for improving parameterization in models. In particular, conditional generative adversarial networks (C-GANs or simply GANs in the following) can be successfully applied to the problems discussed above (Goodfellow et al., 2014). GANs is a class of ML tools in which two neural networks compete with each other in a min-max optimization problem. The first network, called generator, aims to generate new data samples that are indistinguishable from the training data (e.g., high-resolution melting maps obtained from the remote sensing observations) by the other network, called discriminator. In our case the GAN aims to generate high-resolution melting maps that are indistinguishable by the second network from high-resolution remote sensing observations or numerical model outputs. We have already started to build the architecture for this framework and are in the phase of collecting the necessary datasets and build the proper data framework to perform such work.

Chapter 6

Conclusions

Now this is not the end. It is not even the beginning of the end. But it is, perhaps, the end of the beginning.

W.S. Churchill,
10 Novembre 1942

We studied different aspects of the cryosphere from global, through regional to local scale. The specific conclusions of each paper are reported at the end of every chapter. In the following a summary of the main findings is reported.

From the analysis of snow depth and snow density measurements, we studied the climatology of snow depth and SWE in six groups of catchments in the Italian Alps between 1967 and 2020. We investigated changes and variability in snow depth and SWE due to climate modifications, especially temperature increase, in the past century. We found that snow depth has been decreasing of about 12 cm every decade and SWE of about 37 mm every decade. On average, during the monitoring period 1994-2020 maximum snow depth has been 33% lower than between 1967 and 1993, with stronger differences at low elevations, up to 63% below 1500 m asl. Similarly, we found a decrease of 36% of maximum SWE. For the second half-period we also obtained higher snow line elevation, confirming that snow is retreating and disappearing at low elevations. We found that the strongest decrease is recorded in spring, suggesting a strong impact of global warming on spring snowmelt, potentially impacting the hydrological regime of the considered catchments, flood magnitude and timing, and water availability in summer. The data also exhibited a change point at the end of the 1980s, with significantly lower snow depth and SWE in the next decades. This result has been confirmed by the analysis of temperature and precipitation data from the HISTALP dataset. The analysis pointed out the strong dependance of snow cover in the Alps on air temperature, regulating solid-liquid precipitation separation and snowmelt onset in spring. We also found a positive correlation with the WeMO index and a negative correlation with the NAO index. Finally, we provided a SWE model to estimate the average SWE as function of day of the year and elevation for a given basin. This study highlighted the impacts of climate change on the cryosphere at regional scale, quantifying the reduction of water resources in the Alpine region since the end of the 1960s.

At local scale, we investigated the effects of snow cover in the formation of flood events. Specifically, we studied the snowmelt contribution in case of intense rainfall events in Lombardy, considering the case study of Aprica and Pantano d'Avio stations. Since 1996, these two stations collect precipitation, temperature and snow depth measurements. The calibration of a SWE model provided the degree-day factor used to estimate the snowmelt produced during rainy days. We reconstructed the cumulated precipitation series (P) for the fixed durations 1, 3, 6, 12 and 24 hours and computed, for the same durations, the combined timeseres of precipation and meltin (P+M). From the annual maxima analysis (using GEV, EV1 and L-N distributions) we found that snowmelt can increase the quantiles of precipitation for a given return period of about 2.2%, on average. We found larger impacts for longer durations, with snowmelt contributing up to 10% of the precipitation. Consequently, future studies will focus on investigating longer durations. Finally, we provided the intensity-duration-frequency curves at the two considered locations, computed considering only precipitation and the combination of precipitation and snowmelt.

Moving to larger scale, we investigated surface melting over the Greenland ice sheet by using threshold-based melt detection algorithm applied to high-resolution passive microwave data. We computed the cross-calibration parameters necessary to reduce the bias within the timeseries. Then we applied the melt detection algorithms to the 40 years long dataset, assessing the performances through the comparison with automatic weather station air temperature measurements and the output of the regional climate model MAR. We found that the best surface melting estimate is provided by the algorithm based on the electromagnetic model MEMLS, showing the lowest commission and omission errors and better capturing the temporal evolution of surface melt extent. We also found that surface melt extent is largely underestimated by the oldest sensors, limiting the consistency of the timeseries. From the long-term trend analysis, we found that the melting season has started about 0.4 days earlier and ended 0.7 days later every year since 1979. These trends reduce respectively to 0.3 and 0.3 if computed over the period 1988-2019. The average number of melting days has increased by 0.45 (0.3) days every year since 1979 (1988). The maximum melt extent has been increasing of about the 6.9% of the Greenland ice sheet total surface every year since 1979 and of 3.6% since 1988. The enhanced resolution dataset better performed in capturing the spatial distribution of surface melting when compared with regional climate model outputs than the coarser resolution one.

A further step towards high resolution data for the Greenland ice sheet has been taken applying a statistical downscaling technique to MAR regional climate model, obtaining 100 m spatial resolution outputs for air temperature, surface temperature and SMB. In case of air temperature, our results showed no significant improvement nor deterioration with respect to the original MAR data, suggesting that we are not introducing errors. We found improvements in case of surface temperature data, with the enhanced resolution dataset better capturing the spatial scales in terms of autocorrelation when compared with Landsat-8 observations. The downscaled product better estimates SMB at local scale. The comparison with in-situ observations exhibits an increased R2, from 0.868 to 0.935, a reduced RMSE for the majority of the considered measurement sites and the parameters of the regression line, slope and intercept, taking values closer to 1 and 0, respectively.

Bibliography

[1] Abdalati, W., Steffen, K., Otto, C., and Jezek, K. C.: Comparison of brightness temperatures from SSMI instruments on the DMSP F8 and FII satellites for Antarctica and the Greenland ice sheet. International Journal of Remote Sensing, 16(7), 1223-1229, 1995.

[2] Abdalati, W., and Steffen, K.: Passive microwave-derived snow melt regions on the Greenland ice sheet. Geophysical Research Letters, 22(7), 787-790, 1995.

[3] Alexander, P. M., M. Tedesco, X. Fettweis, R. Van De Wal, C.J.P.P. Smeets, and M.R. Van Den Broeke: Assessing spatio- temporal variability and trends in modelled and measured Greenland Ice Sheet albedo (2000–2013). The Cryosphere, 8, 2293– 2312, 2014.

[4] Allard, W.: Snow Hydrology: Summary Report of the Snow Investigations. Published by the North Pacific Division, Corps of Engineers, US Army, Portland, Oregon, 1956. 437 pages, 70 pages of plates, maps and figs., 27 cm. Journal of Glaciology, 3(22), 148-148, 1957.

[5] Anderson, E.: Development and testing of snow pack energy balance equations., Water Resourc. Res. 4(1) 19-37, 1968.

[6] Anderson, E.: National Weather Service river forecast system—snow accumulation and ablation model, NOAA Tech. Memo. NWS HYDRO-17, U.S. Dep. Commerce, Silver Springs, MD, 217 pp, 1973.

[7] Anderson, E. A., Colbeck, S., Slaughter, C. W., Bissell, V., Male, D. H., Crook, A. G., and Wiesnet, D. R.: Snow accumulation, distribution, melt, and runoff, Eos, Transactions American Geophysical Union, 60(21), 465-468, 1979.

[8] Armstrong, R., K. Knowles, M. Brodzik and M. A. Hardman: DMSP SSM/I-SSMIS Pathfinder Daily EASE-Grid Brightness Temperatures. Version 2. Boulder, Colorado USA: NASA DAAC at the National Snow and Ice Data Center, https://nsidc.org/data/NSIDC-0032/versions/2, 1994, updated current year.

[9] Arrhenius, S.: On the influence of carbonic acid in the air upon the temperature of the ground, The London, Edinburgh, and Dublin Philosophical Magazine and Journal of Science, 41(251), 237-276, 1896.

[10] Aschwanden, A., Fahnestock, M. A., Truffer, M., Brinkerhoff, D. J., Hock, R., Khroulev, C., Mottram, R. and Khan, S. A.: Contribution of the Greenland Ice Sheet to sea level over the next millennium, Science Advances, 5(6), eaav9396, 2019.

[11] Ashcraft, I. S., and Long, D. G.: Comparison of methods for melt detection over Greenland using active and passive microwave measurements. International Journal of Remote Sensing, 27(12), 2469-248, 2006.

[12] Auer, I., Böhm, R., Jurkovic, A., Lipa, W., Orlik, A., Potzmann, R., Schöner, W., Ungersbock, M., Matulla, C., Briffa, K., Jones, P., Efthymiadis, D., Brunetti, M., Nanni, T., Maugeri, M., Mercalli, L., Mestre, O., Moisselin, J.-M., Begert, M., Muller- ¨Westermeier, G., Kveton, V., Bochnicek, O., Stastny, P., Lapin,M., Szalai, S., Szentimrey, T., Cegnar, T., Dolinar, M., GajicCapka, M., Zaninovic, K., Majstorovic, Z. and Nieplova, E.: HISTALP—historical instrumental climatological surface time series of the Greater Alpine Region. International Journal of Climatology: A Journal of the Royal Meteorological Society, 27(1), 17-46, 2007.

[13] Avanzi, F., De Michele, C., and Ghezzi, A.: On the performances of empirical regressions for the estimation of bulk snow density, 2015.

[14] Backus, G.E. and J. F. Gilbert: Numerical applications of a formalism for geophysical inverse problems, Geophys. J. R. Astron. Soc., vol. 13, pp. 247–276, 1967.

[15] Backus, G. and Gilbert, F.: The Resolving Power of Gross Earth Data, Geophys J Int, 16(2), 169–205, 1968.

[16] Bavera, D., and De Michele, C.: Snow water equivalent estimation in the Mallero basin using snow gauge data and MODIS images and fieldwork validation. Hydrological Processes: An International Journal, 23(14), 1961-1972, 2009.

[17] Beaudry, P. G., and Golding, D. L.: Snowmelt during rain-on-snow in coastal British Columbia., in Proceedings of the Western Snow Conference (Vol. 51, pp. 55-66), 1983.

[18] Beniston, M.: Is snow in the Alps receding or disappearing?. Wiley Interdisciplinary Reviews: Climate Change, 3(4), 349-358, 2012.

[19] Beniston, M., Farinotti, D., Stoffel, M., Andreassen, L. M., Coppola, E., Eckert, N., Fantini, A., Giacona, F., Hauck, C., Huss, M., Huwald, H., Lehning, M., López-Moreno, J.-I., Magnusson, J., Marty, C., Morán-Tejéda, E., Morin, S., Naaim, M., Provenzale, A., Rabatel, A., Six, D., Stötter, J., Strasser, U., Terzago, S. and Vincent, C.: The European mountain cryosphere: a review of its current state, trends, and future challenges. The Cryosphere, 12(2), 759-794, 2018.

[20] Bennartz, R., Shupe, M. D., Turner, D. D., Walden, V. P., Steffen, K., Cox, C. J., Kulie, M. S., Miller, N. B. and Pettersen, C.: July 2012 Greenland melt extent enhanced by low-level liquid clouds, Nature, 496(7443), 83–86, 2013.

[21] Berris, S. N., and Harr, R. D.: Comparative snow accumulation and melt during rainfall in forested and clear-cut plots in the western Cascades of Oregon, Water Resources Research, 23(1), 135-142, 1987.

[22] Bocchiola, D., and Diolaiuti, G.: Evidence of climate change within the Adamello glacier of Italy. Theoretical and Applied Climatology, 100 (3), 351—369, 2009.

[23] Bony, S., Colman, R., Kattsov, V. M., Allan, R. P., Bretherton, C. S., Dufresne, J. L., Hall, A., Hallegatte, S., Holland, M. M., Ingram, W., Randall, D. A., Soden, B. J., Tselioudis, G., Webb, M. J.: How well do we understand and evaluate climate change feedback processes?, Journal of Climate, 19(15), 3445-3482, 2006.

[24] Braithwaite, R. J.: Positive degree-day factors for ablation on the Greenland ice sheet studied by energy-balance modelling, Journal of Glaciology, 41(137), 153-160, 1995.

[25] Braithwaite, R.J. and O. B. Oelsen, Calculation of glacier ablation from air temperature, West Greenland. In Oerlemens, J. (ed), Glacier Fluctuations in Cimatic Change. Dordrecth: Kluwer Academic Publishers, pp.219-233, 1989.

[26] Brodzik, M. J. and K. W. Knowles: EASE-Grid: a versatile set of equal-area projections and grids, in: Discrete Global Grids, M. Goodchild (Ed.), National Center for Geographic Information and Analysis, Santa Barbara, CA: USA, 2002.

[27] Brodzik, M. J., B. Billingsley, T. Haran, B. Raup and M. H. Savoie, EASE-Grid 2.0: Incremental but Significant Improvements for Earth-Gridded Data Sets. ISPRS Int. J. Geo-Inf., 1:32–45, 2012.

[28] Brodzik, M. J., Long, D. G., Hardman, M. A., Paget, A., and Armstrong, R. L.: MEaSUREs Calibrated Enhanced-Resolution Passive Microwave Daily EASE-Grid 2.0 Brightness Temperature ESDR, Version 1; National Snow and Ice Data Center: Boulder, CO, USA, Digital Media, 2016. Updated 2020.

[29] Brugnara, Y., and Maugeri, M.: Daily precipitation variability in the southern Alps since the late 19th century. International journal of climatology, 39(8), 3492-3504, 2019.

[30] Brun, E., David, P., Sudul, M., and Brunot, G.: A numerical model to simulate snow-cover stratigraphy for operational avalanche forecasting, J. Glaciol., 38, 13–22, 1992.

[31] Brunetti, M., Lentini, G., Maugeri, M., Nanni, T., Auer, I., Boehm, R., and Schöener, W.: Climate variability and change in the greater alpine region over the last two centuries based on multi-variable analysis. International Journal of Climatology, 29 (15), 2197—2225, 2009.

[32] Caccin, B., Roberti, C., Russo, P. and Smaldone, L. A.: The Backus-Gilbert inversion method and the processing of sampled data, IEEE Trans. Signal Process., 40(11), 2823–2825, 1992.

[33] Cagnati, A., Crepaz, A., Macelloni, G., Pampaloni, P., Ranzi, R., Tedesco, M., and Valt, M.: Study of the snow melt–freeze cycle using multi-sensor data and snow modelling, J. Glaciol., 50(170), 419-426, 2004.

[34] Cavalieri, D. J., and Parkinson, C. L.: Arctic sea ice variability and trends, 1979–2010. The Cryosphere, 6(4), 881-889, 2012.

[35] Cavalieri, D. J., Parkinson, C. L., DiGirolamo, N. and Ivanoff, A.: Intersensor Calibration Between F13 SSMI and F17 SSMIS for Global Sea Ice Data Records, IEEE Geosci. Remote Sensing Lett., 9(2), 233–236, 2012.

[36] Chimani, B., Böhm, R., Matulla, C., and Ganekind, M.: Development of a longterm dataset of solid/liquid precipitation. Advances in Science and Research, 6(1), 39-43, 2011.

[37] Cohen, J., Ye, H., and Jones, J.: Trends and variability in rain-on-snow events, Geophysical Research Letters, 42(17), 7115-7122, 2015.

[38] Colbeck, S. C.: A theory of water percolation in snow, Journal of glaciology, 11(63), 369-385, 1972.

[39] Colbeck, S. C., and Anderson, E. A.: The permeability of a melting snow cover, Water Resources Research, 18(4), 904-908, 1982.

[40] Collection 2 Landsat 8-9 OLI (Operational Land Imager) and TIRS (Thermal Infrared Sensor) Level-2 Science Product Digital Object Identifier (DOI) number: /10.5066/P9OGBGM6. [Last access, 16/02/2023].

[41] Colombo, N., Valt, M., Romano, E., Salerno, F., Godone, D., Cianfarra, P., Freppaz, M., Maugeri, M., and Guyennon, N.: Long-term trend of snow water equivalent in the Italian Alps. Journal of Hydrology, 614, 128532, 2022.

[42] Colosio, P., Tedesco, M., Ranzi, R., and Fettweis, X.: Surface melting over the Greenland ice sheet derived from enhanced resolution passive microwave brightness temperatures (1979–2019). The Cryosphere, 15(6), 2623-2646, 2021.

[43] Colosio, P., Ranzi, R., Boselli, V., Raccagni, P., and Galeati, G.: Climatology of snow depth and snow water equivalent in the Italian Alps (1967-2020). In AGU Fall Meeting Abstracts (Vol. 2021, pp. C35G-0953), 2021.

[44] Conway, H., and Raymond, C. F.: Snow stability during rain, Journal of Glaciology, 39(133), 635-642, 1993.

[45] Dai, L. and Che, T.: Cross-platform calibration of SMMR, SSM/I and AMSR-E passive microwave brightness temperature, edited by H. Guo and C. Wang, p. 784103, Beijing, China., 2009.

[46] Dai, L., Che, T. and Ding, Y.: Inter-Calibrating SMMR, SSM/I and SSMI/S Data to Improve the Consistency of Snow-Depth Products in China, Remote Sensing, 7(6), 7212–7230, 2015.

[47] De Ridder, K. and Gallee, H.: Land Surface-Induced Regional Climate Change in Southern Israel, J. Appl. Meteorol., 37, 1470–1485, 1998.

[48] Dee, D. P., Uppala, S. M., Simmons, A. J., Berrisford, P., Poli, P., Kobayashi, S., Andrae, U., Balmaseda, M. A., Balsamo, G., Bauer, P., Bechtold, P., Beljaars, A. C. M., van de Berg, L., Bidlot, J., Bormann, N., Delsol, C., Dragani, R., Fuentes, M., Geer, A. J.,

Haimberger, L., Healy, S. B., Hersbach, H., Holm, E. V., Isaksen, L., Kallberg, P., Kohler, M., Matricardi, M., McNally, A. P., Monge-Sanz, B. M., Morcrette, J.-J., Park, B.-K., Peubey, C., de Rosnay, P., Tavolato, C., Thepaut, J.-N. and Vitart, F.: The ERA-Interim reanalysis: configuration and performance of the data assimilation system, Q.J.R. Meteorol. Soc., 137(656), 553–597, 2011.

[49] Delhasse, A., Kittel, C., Amory, C., Hofer, S., van As, D., S. Fausto, R., and Fettweis, X.: Brief communication: Evaluation of the near-surface climate in ERA5 over the Greenland Ice Sheet, The Cryosphere, 14, 957–965, 2020.

[50] Delhomme, J.: Kriging in the hydrosciences, Advances in Water Resources, 1(5), 251–266, 1978.

[51] Durand, Y., Giraud, G., Laternser, M., Etchevers, P., Mérindol, L., and Lesaffre, B.: Reanalysis of 47 years of climate in the French Alps (1958–2005): climatology and trends for snow cover. Journal of applied meteorology and climatology, 48(12), 2487-2512, 2009.

[52] Edward, H., Isaaks, E. H., and Srivastava, R. M.: An introduction to applied geostatistics, Oxford University Press, Oxford (UK), 561 pp., 1989.

[53] Farrar, M. R. and Smith, E. A.: Spatial resolution enhancement of terrestrial features using deconvolved SSM/I microwave brightness temperatures, IEEE Trans. Geosci. Remote Sensing, 30(2), 349–355, 1992.

[54] Fettweis, X., Gallée, H., Lefebre, F. and van Ypersele, J.-P.: Greenland surface mass balance simulated by a regional climate model and comparison with satellite-derived data in 1990–1991, Climate Dynamics, 24(6), 623–640, 2005.

[55] Fettweis, X., Gallee, H., Lefebre, F. and van Ypersele, J.-P.: Greenland surface mass balance simulated by a regional climate model and comparison with satellite-derived data in 1990–1991, Climate Dynamics, 24(6), 623–640, 2007.

[56] Fettweis, X., Tedesco, M., van den Broeke, M. and Ettema, J.: Melting trends over the Greenland ice sheet (1958-2009) from spaceborne microwave data and regional climate models, The Cryosphere Discuss., 4(4), 2433–2473, 2010.

[57] Fettweis, X., Tedesco, M., van den Broeke, M., and Ettema, J.: Melting trends over the Greenland ice sheet (1958–2009) from spaceborne microwave data and regional climate models, The Cryosphere, 5, 359–375, 2011.

[58] Fettweis, X., Franco, B., Tedesco, M., van Angelen, J. H., Lenaerts, J. T. M., van den Broeke, M. R., and Gallee, H.: Estimating the Greenland ice sheet surface mass balance contribution to future sea level rise using the regional atmospheric climate model MAR, The Cryosphere, 7, 469–489, 2013.

[59] Fettweis, X., Box, J. E., Agosta, C., Amory, C., Kittel, C., Lang, C., van As, D., Machguth, H. and Gallee, H.: Reconstructions of the 1900–2015 Greenland ice sheet surface mass balance using the regional climate MAR model, The Cryosphere, 11(2), 1015–1033, 2017.

[60] Fettweis, X., Hofer, S., Krebs-Kanzow, U., Amory, C., Aoki, T., Berends, C. J., Born, A., Box, J. E., Delhasse, A., Fujita, K., Gierz, P., Goelzer, H., Hanna, E., Hashimoto, A., Huybrechts, P., Kapsch, M.-L., King, M. D., Kittel, C., Lang, C., Langen, P. L., Lenaerts, J. T. M., Liston, G. E., Lohmann, G., Mernild, S. H., Mikolajewicz, U., Modali, K., Mottram, R. H., Niwano, M., Noël, B., Ryan, J. C., Smith, A., Streffing, J., Tedesco, M., van de Berg, W. J., van den Broeke, M., van de Wal, R. S. W., van Kampenhout, L., Wilton, D., Wouters, B., Ziemen, F., and Zolles, T.: GrSMBMIP: intercomparison of the modelled 1980–2012 surface mass balance over the Greenland Ice Sheet, The Cryosphere, 14, 3935–3958, 2020.

[61] Fontrodona Bach, A., Van der Schrier, G., Melsen, L. A., Klein Tank, A. M. G., and Teuling, A. J.: Widespread and accelerated decrease of observed mean and extreme snow depth over Europe, Geophysical Research Letters, 45(22), 12-312, 2018.

[62] Franco, B., Fettweis, X., Lang, C., and Erpicum, M.: Impact of spatial resolution on the modelling of the Greenland ice sheet surface mass balance between 1990–2010, using the regional climate model MAR, The Cryosphere, 6(3), 695-711, 2012.

[63] Frezzotti, M., Urbini, S., Proposito, M., Scarchilli, C. and Gandolfi, S.: Spatial and temporal variability of surface mass balance near Talos Dome, East Antarctica, Journal of Geophysical Research, 112(F2), 2007.

[64] Ge, Y., and Gong, G.: North American snow depth and climate teleconnection patterns, Journal of Climate, 22(2), 217-233, 2009.

[65] Giorgi, F., Hurrell, J. W., Marinucci, M. R., and Beniston, M.: Elevation dependency of the surface climate change signal: a model study, Journal of Climate, 10(2), 288-296, 1997.

[66] Goodfellow, Ian J., Pouget-Abadie J., Mirza M., Xu B., Warde-Farley D., Ozair S., Courville A., and Bengio Y.: Generative adversarial networks, Commun. Acm, 63(11), 139-144, 2004.

[67] Greenwood, J. A., J. M. Landwehr, N. C. Matalas, and J. R. Wallis.: Probability weighted moments: Definition and relation to parameters of several distributions expressible in inverse form, Water Resour. Res. 15: 1049-1054, 1979.

[68] Grenfell, T. C., and Putkonen, J.: A method for the detection of the severe rain-on-snow event on Banks Island, October 2003, using passive microwave remote sensing, Water Resources Research, 44(3), 2008.

[69] Grossi, G., Lendvai, A., Peretti, G., and Ranzi, R.: Snow Precipitation Measured by Gauges: Systematic Error Estimation and Data Series Correction in the Central Italian Alps, Water, 9(7), 461, 2017.

[70] Grünewald, T., Bühler, Y., and Lehning, M.: Elevation dependency of mountain snow depth, The Cryosphere, 8(6), 2381-2394, 2014.

[71] Guyennon, N., Valt, M., Salerno, F., Petrangeli, A. B., and Romano, E.: Estimating the snow water equivalent from snow depth measurements in the Italian Alps, Cold Regions Science and Technology, 167, 102859, 2019.

[72] Hanna, E., Huybrechts, P., Janssens, I., Cappelen, J., Steffen, K., and Stephens, A.: Runoff and mass balance of the Greenland ice sheet: 1958–2003, Journal of Geophysical Research: Atmospheres, 110(D13), 2005.

[73] Hallikainen, M. T., Ulaby, F. T., and Van Deventer, T. E.: Extinction behavior of dry snow in the 18-to 90-GHz range, IEEE Transactions on Geoscience and Remote Sensing, (6), 737-745, 1987.

[74] Hanna, E., Huybrechts, P., Steffen, K., Cappelen, J., Huff, R., Shuman, C., Irvine-Fynn, T., Wise, S., and Griffiths, M.: Increased runoff from melt from the Greenland Ice Sheet: a response to global warming, Journal of Climate, 21(2), 331-341, 2008.

[75] Hanna, E., Huybrechts, P., Cappelen, J., Steffen, K., Bales, R. C., Burgess, E., McConnell, J. R., Steffensen, J. P., Van den Broeke, M., Wake, L., Bigg, B., Griffiths, M., and Savas, D.: Greenland Ice Sheet surface mass balance 1870 to 2010 based on Twentieth Century Reanalysis, and links with global climate forcing, Journal of Geophysical Research: Atmospheres, 116(D24), 2011.

[76] Hanna, E., Cappelen, J., Fettweis, X., Mernild, S. H., Mote, T. L., Mottram, R., Steffen, K., Ballinger, T.J., and Hall, R. J.: Greenland surface air temperature changes from 1981 to 2019 and implications for ice-sheet melt and mass-balance change, International Journal of Climatology, 41, E1336-E1352, 2021.

[77] Hersbach, H., Bell, B., Berrisford, P., Hirahara, S., Horanyi, A., Munoz-Sabater, J., Nicolas, J., Peubey, C., Radu, R., Schepers, D., Simmons, A., Soci, C., Abdalla, S., Abellan, X., Balsamo, G., Bechtold, P., Biavati, G., Bidlot, J., Bonavita, M., Chiara, G., Dahlgren, P., Dee, D., Diamantakis, M., Dragani, R., Flemming, J., Forbes, R., Fuentes, M., Geer, A., Haimberger, L., Healy, S., Hogan, R. J., Holm, E., Janiskova, M., Keeley, S., Laloyaux, P., Lopez, P., Lupu, C., Radnoti, G., Rosnay, P., Rozum, I., Vamborg, F., Villaume, S. and Thepaut, J. N.: The ERA5 global reanalysis, Quarterly Journal of the Royal Meteorological Society, 2020.

[78] Heywood, L.: Rain on snow avalanche events-Some observations, In Proceedings of the 1988 international snow science workshop (pp. 135-136), 1988.

[79] Hörhold, M., Münch, T., Weißbach, S., Kipfstuhl, S., Freitag, J., Sasgen, I., Lohmann, G., Vinther, B., and Laepple, T.: Modern temperatures in central–north Greenland warmest in past millennium, Nature 613, 503–507, 2023.

[80] Hosking, J. R. M.: L-moments: analysis and estimation of distributions using linear combinations of order statistics, J. R. Stat. Soc. Ser. B, 52: 105-124, 1990.

[81] Il Jeong, D., and Sushama, L.: Rain-on-snow events over North America based on two Canadian regional climate models, Climate Dynamics, 50, 303-316, 2018.

[82] Jenkinson, A. F.: General extreme value distribution, In Estimation of maximum floods, World metereological Organization, Technical Note, no. 98, chapter 5, 183-257, 1969.

[83] Jenkinson, A. F.: The frequency distribution of the annual maximun (or minimum) value of metereological elements, Q. J. Royal Meteorol. Soc., Vol. 81, 157-171, 1955.

[84] Jezek, K. C., Merry, C. J. and Cavalieri, D. J.: Comparison of SMMR and SSM/I passive microwave data collected over Antarctica, A. Glaciology., 17, 131–136, 1993.

[85] Joshi, M., Merry, C. J., Jezek, K. C. and Bolzan, J. F.: An edge detection technique to estimate melt duration, season and melt extent on the Greenland Ice Sheet using Passive Microwave Data, Geophys. Res. Lett., 28(18), 3497–3500, 2001.

[86] Kargel, J. S., Abrams, M. J., Bishop, M. P., Bush, A., Hamilton, G., Jiskoot, H., Kääb, A., Kieffer, H. H., Lee, E. M., Paul, F., Rau, F., Raup, B., Shroder, J. F., Soltesz, D., Stainforth, D., Stearns, L. and Wessels, R.: Multispectral imaging contributions to global land ice measurements from space, Remote Sensing of Environment, 99(1-2), 187–219, 2005.

[87] Kargel, J. S., Leonard, G. J., Bishop, M. P., Kääb, A., and Raup, B. H. (Eds.): Global land ice measurements from space. Springer, 2014.

[88] Kendall, M.: Rank Correlation Methods, 4th edition, London: Charles Griffin, 1975.

[89] Knowles, K. E., Njoku, G., Armstrong, R., and Brodzik, M.: Nimbus-7 SMMR Pathfinder Daily EASE-Grid Brightness Temperatures, version 1, NASA National Snow Ice Data Center Distributed Active Archive Center: Boulder, CO, USA, 2000.

[90] Knowles, K., M. Savoie, R. Armstrong and M. Brodzik: AMSR-E/Aqua Daily EASE-Grid Brightness Temperatures, Boulder, Colorado USA: NASA DAAC at the National Snow and Ice Data Center, doi:10.5067/XIMNXRTQVMOX, 2006.

[91] Kottegoda, N. T., and Rosso, R.: Applied statistics for civil and environmental engineers, Blackwell Publishing, 2008.

[92] Kouki, K., Anttila, K., Manninen, T., Luojus, K., Wang, L. and Riihelä, A.: Intercomparison of Snow Melt Onset Date Estimates From Optical and Microwave Satellite Instruments Over the Northern Hemisphere for the Period 1982–2015, Journal of Geophysical Research: Atmospheres, 124(21), 11205–11219, 2019.

[93] Le Meur, E., Magand, O., Arnaud, L., Fily, M., Frezzotti, M., Cavitte, M., Mulvaney, R. and Urbini, S.: Spatial and temporal distributions of surface mass balance between Concordia and Vostok stations, Antarctica, from combined radar and ice core data: first results and detailed error analysis, The Cryosphere, 12(5), 1831–1850, 2018.

[94] Lehning, M., Grünewald, T., and Schirmer, M.: Mountain snow distribution governed by an altitudinal gradient and terrain roughness, Geophysical Research Letters, 38(19), 2011.

[95] Lehr, C., Ward, P. J., and Kummu, M.: Impact of large-scale climatic oscillations on snowfall-related climate parameters in the world's major downhill ski areas: a review, Mountain Research and Development, 32(4), 431-445, 2012.

[96] Lejeune, Y., Dumont, M., Panel, J. M., Lafaysse, M., Lapalus, P., Le Gac, E., Lesaffre, B., and Morin, S.: 57 years (1960–2017) of snow and meteorological observations from a mid-altitude mountain site (Col de Porte, France, 1325 m of altitude), Earth System Science Data, 11(1), 71-88, 2019.

[97] Liu, H., Wang, L. and Jezek, K. C.: Wavelet-transform based edge detection approach to derivation of snowmelt onset, end and duration from satellite passive microwave measurements, International Journal of Remote Sensing, 26(21), 4639–4660, 2005.

[98] Long, D. G. and Daum, D. L.: Spatial resolution enhancement of SSM/I data, IEEE Trans. Geosci. Remote Sensing, 36(2), 407–417, 1998.

[99] López-Moreno, J. I., Soubeyroux, J. M., Gascoin, S., Alonso-Gonzalez, E., Durán-Gómez, N., Lafaysse, M., M., Vernay, M., Carmagnola, C., and Morin, S.: Long-term trends (1958–2017) in snow cover duration and depth in the Pyrenees, International Journal of Climatology, 40(14), 6122-6136, 2020.

[100] Macelloni, G., Paloscia, S., Pampaloni, P. and Tedesco, M.: Microwave emission from dry snow: a comparison of experimental and model results, IEEE Trans. Geosci. Remote Sensing, 39(12), 2649–2656, 2001.

[101] Macelloni, G., Paloscia, S., Pampaloni, P., Brogioni, M., Ranzi, R. and Crepaz, A.: Monitoring of melting refreezing cycles of snow with microwave radiometers: The Microwave Alpine Snow Melting Experiment (MASMEx 2002-2003). IEEE Transactions on Geoscience and Remote Sensing, 43(11), 2431-2442, 2005.

[102] Macelloni, G., Brogioni, M., Pampaloni, P., and Cagnati, A.: Multifrequency microwave emission fromthe dome-c area on the east antarctic plateau: temporal and spatial variability, IEEE transactions on geoscience and remote sensing, 45(7), 2029-2039, 2007.

[103] Machguth, H., H.H. Thomsen, W. Weidick, A.P. Ahlstrøm, J. Abermann, M. Andersen, S.B. Andersen, A.A. Bjørk, J.E. Box, R. Braithwaite, C.E. Bøggild, M. Citterio, P. Clement, W. Colgan, R.S. Fausto, K. Gleie, S. Gubler, B. Hasholt, B. Hynek, N.T. Knudsen, S.H. Larsen, S.H. Mernild, J. Oerlemans, H. Oerter, O.B. Olsen, C.J.P. Smeets, K. Steffen, M. Stober, S. Sugiyama, S. van As, M.R. van den Broeke and R.S.W. van de Wal.: Greenland surface mass-balance observations from the ice-sheet ablation area and local glaciers, Journal of Glaciology, 62: 861-887, 2016.

[104] Machguth, H.: Historical surface mass balance measurements from the ice-sheet ablation area and local glaciers, https://doi.org/10.22008/FK2/5VNBQA, GEUS Dataverse, V1, 2022. [Last access 16/07/2022].

[105] Mann, H.B.: Nonparametric tests against trend, Econometrica: Journal of the Econometric Society, 13, 245–259, 1945.

[106] Mann, H. B., and Whitney, D. R.: On a test of whether one of two random variables is stochastically larger than the other, The annals of mathematical statistics, 50-60,1947.

[107] Marbouty, D.: An experimental study of temperature-gradient metamorphism, Journal of Glaciology, 26(94), 303-312, 1980.

[108] Marcolini, G., Bellin, A., Disse, M., and Chiogna, G.: Variability in snow depth time series in the Adige catchment. Journal of Hydrology: Regional Studies, 13, 240-254, 2017.

[109] Mark, D. M., and Aronson, P. B.: Scale-dependent fractal dimensions of topographic surfaces: an empirical investigation, with applications in geomorphology and computer mapping, Journal of the International Association for Mathematical Geology, 16, 671-683, 1984.

[110] Marks, D., Kimball, J., Tingey, D., and Link, T.: The sensitivity of snowmelt processes to climate conditions and forest cover during rain-on-snow: A case study of the 1996 Pacific Northwest flood, Hydrological Processes, 12(10-11), 1569-1587, 1998.

[111] Martin-Vide, J., and Lopez-Bustins, J. A.: The western Mediterranean oscillation and rainfall in the Iberian Peninsula, International Journal of Climatology: A Journal of the Royal Meteorological Society, 26(11), 1455-1475, 2006.

[112] Martinec, J.: The degree-day factor for snowmelt runoff forecasting, IUGG General Assembly of Helsinki, IAHS Publ. No. 51, 468-477, 1960.

[113] Marty, C., Tilg, A. M., and Jonas, T.: Recent evidence of large-scale receding snow water equivalents in the European Alps. Journal of Hydrometeorology, 18(4), 1021-1031, 2017.

[114] Matiu, M., Crespi, A., Bertoldi, G., Carmagnola, C. M., Marty, C., Morin, S., Schöner, W., Cat Berro, D., Chiogna, G., De Gregorio, L., Kotlarski, S., Majone, B., Resch, G., Terzago, S., Valt, M., Beozzo, W., Cianfarra, P., Gouttevin, I., Marcolini, G., Natarnicola, C., Petitta M., Scherrer, S. C., Strasser, U., Winkler, M., Zebisch, M., Cicogna, A., Cremonini, R., Debernardi, A., Faletto, M., Gaddo, M., Giovannini, L., Mercalli, L., Soubeyroux, J. M., Sušnik, A., Trenti, A., Urbani, S., and Weilguni, V.: Observed snow depth trends in the European Alps: 1971 to 2019, The Cryosphere, 15(3), 1343-1382, 2021.

[115] McCabe, G. J., Clark, M. P., and Hay, L. E.: Rain-on-snow events in the western United States, Bulletin of the American Meteorological Society, 88(3), 319-328, 2007.

[116] Mote, T. L.: Greenland surface melt trends 1973–2007: evidence of a large increase in 2007, Geophys. Res. Lett., 34, L22507, 2007.

[117] Mote, T. L.: MEaSUREs Greenland Surface Melt Daily 25km EASE-Grid 2.0, Version 1., Boulder, Colorado USA. NASA National Snow and Ice Data Center Distributed Active Archive Center. https://doi.org/10.5067/MEASURES/CRYOSPHERE/nsidc-0533.001, 2014. [Access date: 15 December 2020].

[118] Poe, G. A.: Optimum interpolation of imaging microwave radiometer data, IEEE Trans. Geosci. Remote Sensing, 28(5), 800–810, 1990.

[119] Mouginot, J., Rignot, E., Bjørk, A. A., Broeke, M. van den, Millan, R., Morlighem, M., Noël, B., Scheuchl, B. and Wood, M.: Forty-six years of Greenland Ice Sheet mass balance from 1972 to 2018, PNAS, 116(19), 9239–9244, doi:10.1073/pnas.1904242116, 2019.

[120] Nash, J. E. and Sutcliffe, J. V.: River flow forecasting through conceptual models, Part 1 – a discussion of principles, J. Hydrol., 10, 282–290, 1970.

[121] Nghiem, S. V., Hall, D. K., Mote, T. L., Tedesco, M., Albert, M. R., Keegan, K., Shuman, C. A., DiGirolamo, N. E. and Neumann, G.: The extreme melt across the Greenland ice sheet in 2012, Geophysical Research Letters, 39(20), 2012.

[122] Noël, B., van de Berg, W. J., Machguth, H., Lhermitte, S., Howat, I., Fettweis, X., and Van Den Broeke, M. R.: A daily, 1 km resolution data set of downscaled Greenland ice sheet surface mass balance (1958–2015), The Cryosphere, 10(5), 2361-2377, 2016.

[123] Noël B, van de Berg, W. J., Lhermitte, S., and van den Broeke, M. R.: Rapid ablation zone expansion amplifies north Greenland mass loss, Sci Adv., 5, eaaw0123, 2019.

[124] Noh, M. J., and Howat, I. M.: Automated stereo-photogrammetric DEM generation at high latitudes: Surface Extraction with TIN-based Search-space Minimization (SETSM) validation and demonstration over glaciated regions, GIScience and Remote Sensing, 52.2 (2015): 198-217, 2015.

[125] NRCS: Part 630 Hydrology National Engineering Handbook, Chapter 11: Snowmelt, 2009.

[126] Osborn, T.: Winter 2009/2010 temperatures and a record-breaking North Atlantic Oscillation index, Weather, 66(1), 19-21, 2011.

[127] Pan, C. G., Kirchner, P. B., Kimball, J. S., Kim, Y., and Du, J.: Rain-on-snow events in Alaska, their frequency and distribution from satellite observations. Environmental Research Letters, 13(7), 075004, 2018.

[128] Pettitt, A. N.: A non-parametric approach to the change-point problem, Journal of the Royal Statistical Society: Series C (Applied Statistics), 28(2), 126-135, 1979.

[129] Pistocchi, A.: Simple estimation of snow density in an Alpine region. Journal of Hydrology: Regional Studies, 6, 82-89, 2016.

[130] Porter, C., Morin, P., Howat, I., Noh, M. J., Bates, B., Peterman, K., Keesey, S., Schlenk, M., Gardiner, J., Tomko, K., Willis, M., Kelleher, C., Cloutier, M., Husby, E., Foga, S., Nakamura, H., Platson, M., Wethington, M. Jr., Williamson, C., Bauer, G., Enos, J., Arnold, G., Kramer, W., Becker, P., Doshi, A., D'Souza, C., Cummens, P., Laurier, F., Bojesen, M.: ArcticDEM, Harvard Dataverse, 2018. [Last access 16/02/2023].

[131] Portner, H.O., Roberts, D.C., Masson-Delmotte, V., Zhai, P., Tignor, M., Poloczanska, E., Mintenbeck, K., Nicolai, M., Okem, A., Petzold, J. and Rama, B.: IPCC, 2019: IPCC Special Report on the Ocean and Cryosphere in a Changing Climate, 2019.

[132] Pulliainen, J., Luojus, K., Derksen, C., Mudryk, L., Lemmetyinen, J., Salminen, M., Ikonen, J., Takala, M., Cohen, J., Smolander, T., and Norberg, J.: Patterns and trends of Northern Hemisphere snow mass from 1980 to 2018, Nature, 581(7808), 294-298, 2020.

[133] Putkonen, J., and Roe, G. J. G. R. L.: Rain-on-snow events impact soil temperatures and affect ungulate survival, Geophysical research letters, 30(4), 2003.

[134] Ranzi, R., Grossi, G., and Bacchi, B.: Ten years of monitoring areal snowpack in the southern alps using noaa-avhrr imagery, ground measurements and hydrological data, Hydrological Processes, 13 (12-13), 2079—2095, 1999.

[135] Ranzi, R., Grossi, G., Gitti, A., and Taschner, S.: Energy and mass balance of the Mandrone glacier (Adamello, central alps), Geografia Fisica e Dinamica Quaternaria, 33 (1), 45—60, 2010.

[136] Ranzi, R., Michailidi, E. M., Tomirotti, M., Crespi, A., Brunetti, M., and Maugeri, M.: A multi-century meteo-hydrological analysis for the Adda river basin (Central Alps). Part II: Daily runoff (1845–2016) at different scales, International Journal of Climatology, 41(1), 181-199, 2021.

[137] Reynard, E.: Mountain Tourism and Water and Snow Management in Climate Change Context, Journal of Alpine Research— Revue de géographie alpine, (108-1), 2020.

[138] Rignot, E., Velicogna, I., van den Broeke, M. R., Monaghan, A. and Lenaerts, J. T. M.: Acceleration of the contribution of the Greenland and Antarctic ice sheets to sea level rise, Geophys. Res. Lett., 38(5), doi:10.1029/2011GL046583, 2011.

[139] Robinson, W. D., Kummerow, C. and Olson, W. S.: A technique for enhancing and matching the resolution of microwave measurements from the SSM/I instrument, IEEE Trans. Geosci. Remote Sensing, 30(3), 419–429, 1992.

[140] Rosa, J.: Forest snowmelt and spring floods, J. Forestry 54(4), 1956.

[141] Schaefli, B., Hingray, B., and Musy, A.: Climate change and hydropower production in the Swiss Alps: quantification of potential impacts and related modelling uncertainties, Hydrology and Earth System Sciences, 11(3), 1191-1205, 2007.

[142] Schöner, W., Koch, R., Matulla, C., Marty, C., and Tilg, A. M.: Spatiotemporal patterns of snow depth within the Swiss-Austrian Alps for the past half century (1961 to 2012) and linkages to climate change, International Journal of Climatology, 39(3), 1589-1603, 2019.

[143] Serreze, M. C., Clark, M. P., Armstrong, R. L., McGinnis, D. A., and Pulwarty, R. S.: Characteristics of the western United States snowpack from snowpack telemetry (SNOTEL) data, Water Resources Research, 35(7), 2145-2160, 1999.

[144] Serreze, M. C., and Barry, R. G.: Processes and impacts of Arctic amplification: A research synthesis, Global and planetary change, 77(1-2), 85-96, 2011.

[145] Steffen, K., Abdalati, W. and Stroeve, J.: Climate sensitivity studies of the Greenland ice sheet using satellite AVHRR, SMMR, SSM/I and in situ data, Meteorl. Atmos. Phys., 51(3–4), 239–258, doi:10.1007/BF01030497, 1993.

[146] Singh, P., Spitzbart, G., Hübl, H., and Weinmeister, H. W.: Hydrological response of snowpack under rain-on-snow events: a field study, Journal of Hydrology, 202(1-4), 1-20, 1997.

[147] Steffen, K., Box, J. E., and Abdalati, W.: Greenland Climate Network: GC-Net, in: CRREL 96-27 Special report on glaciers, ice sheets and volcanoes, trib. to M. Meier, edited by: Colbeck, S.C., US Army Cold Regions Research and Engineering Laboratory (CRREL), Hanover, New Hampshire, USA, 98–103, 1996.

[148] Steffen, K., Houtz, D., Vandecrux, B., Abdalati, W., Bayou, N., Box, J., Colgan, W., Espona Pernas, L.; Griessinger, N., Haas-Artho, D., Heilig, A., Hubert, A., Iosifescu Enescu, I., Johnson-Amin, N., Karlsson, N. B., Kurup, R., McGrath, D., Naderpour, R., Pederson, A. Ø., Perren, B., Phillips, T., Plattner, G., Proksch, M., Revheim, M. K., Saettele, M., Schneebeli, M., Sampson, K., Starkweather, S., Steffen, S., Stroeve, J., Walter, B., Winton, Ø. A. and Zwally, J., Greenland Climate Network (GC-Net) Data., EnviDat 2020, 2020.

[149] Steiner, N. and Tedesco, M.: A wavelet melt detection algorithm applied to enhanced-resolution scatterometer data over Antarctica (2000–2009), The Cryosphere, 8(1), 25–40, 2014.

[150] Steirou, E., Gerlitz, L., Apel, H., and Merz, B.: Links between large-scale circulation patterns and streamflow in Central Europe: A review, Journal of hydrology, 549, 484-500, 2017.

[151] Stogryn, A.: Estimates of brightness temperatures from scanning radiometer data, IEEE Trans. Antennas Propagat., 26(5), 720–726, 1978.

[152] Stroeve, J., Maslanik, J. and Xiaoming, L.: An Intercomparison of DMSP F11- and F13-Derived Sea Ice Products, Remote Sensing of Environment, 64(2), 132–152, 1998.

[153] Sturm, M., Taras, B., Liston, G. E., Derksen, C., Jonas, T., and Lea, J.: Estimating snow water equivalent using snow depth data and climate classes. Journal of Hydrometeorology, 11(6), 1380-1394, 2010.

[154] Tapley, B. D., Bettadpur, S., Watkins, M., and Reigber, C.: The gravity recovery and climate experiment: Mission overview and early results, Geophysical research letters, 31(9), 2004.

[155] Taschner, S., Ranzi, R., Bacchi, B., and Galeati, G.: Monitoring the snow water equivalent in the Piave headwater applying a remotely sensed based approach, in IGARSS 2004, 2004 IEEE International Geoscience and Remote Sensing Symposium (Vol. 6, pp. 3692-3695), 2004.

[156] Takala, M., Luojus, K., Pulliainen, J., Derksen, C., Lemmetyinen, J., Kärnä, J. P., Koskinen, J., and Bojkov, B.: Estimating northern hemisphere snow water equivalent for climate research through assimilation of space-borne radiometer data and ground-based measurements. Remote Sensing of Environment, 115(12), 3517-3529, 2011.

[157] Tedesco, M. and Wang, J. R.: Atmospheric correction of AMSR-E brightness temperatures for dry snow cover mapping, in IEEE Geoscience and Remote Sensing Letters, vol. 3, no. 3, pp. 320-324, 2006.

[158] Tedesco, M., Abdalati, W. and Zwally, H. J.: Persistent surface snowmelt over Antarctica (1987–2006) from 19.35 GHz brightness temperatures, Geophys. Res. Lett., 34(18), L18504, 2007.

[159] Tedesco, M.: Snowmelt detection over the Greenland ice sheet from SSM/I brightness temperature daily variations, Geophys. Res. Lett., 34(2), L02504, 2007.

[160] Tedesco, M.: Assessment and development of snowmelt retrieval algorithms over Antarctica from K-band spaceborne brightness temperature (1979–2008), Remote Sensing of Environment, 113(5), 979–997, 2009.

[161] Tedesco, M., Brodzik, M., Armstrong, R., Savoie, M. and Ramage, J.: Pan arctic terrestrial snowmelt trends (1979–2008) from spaceborne passive microwave data and correlation with the Arctic Oscillation, Geophys. Res. Lett., 36(21), L21402, 2009.

[162] Tedesco, M., Fettweis, X., Mote, T., Wahr, J., Alexander, P., Box, J. E., and Wouters, B.: Evidence and analysis of 2012 Greenland records from spaceborne observations, a regional climate model and reanalysis data, The Cryosphere, 7, 615–630, 2013.

[163] Tedesco, M., Remote sensing of the cryosphere, John Wiley and Sons, 2014.

[164] Tedesco, M., Derksen, C., Deems, J. S., and Foster, J. L.: Remote sensing of snow depth and snow water equivalent. Remote Sensing of the Cryosphere, 73-98, 2015.

[165] Tedesco, M., Doherty, S., Fettweis, X., Alexander, P., Jeyaratnam, J., and Stroeve, J.: The darkening of the Greenland ice sheet: trends, drivers, and projections (1981–2100), The Cryosphere, 10(2), 477-496, 2016.

[166] Tedesco, M. and Fettweis, X.: Unprecedented atmospheric conditions (1948-2019) drive the 2019 exceptional melting season over the Greenland ice sheet, The Cryosphere, 14(4), 1209–1223, 2020.

[167] Terzago, S., Cassardo, C., Cremonini, R., and Fratianni, S.: Snow precipitation and snow cover climatic variability for the period 1971–2009 in the southwestern Italian Alps: The 2008–2009 snow season case study, Water, 2(4), 773-787, 2010.

[168] Torinesi, O., Fily, M. and Genthon, C.: Variability and Trends of the Summer Melt Period of Antarctic Ice Margins since 1980 from Microwave Sensors, Journal of Climate, 16(7), 1047–1060, 2003.

[169] Ulaby, F. T., Moore, R. K., and Fung, A. K.: Microwave remote sensing: Active and passive. Volume 3-From theory to applications, 1986.

[170] Valt, M., and Cianfarra, P.: Recent snow cover variability in the Italian Alps. Cold Regions Science and Technology, 64(2), 146-157, 2010.

[171] Van Den Broeke, M.: Strong surface melting preceded collapse of Antarctic Peninsula ice shelf, Geophys. Res. Lett., 32(12), 2005.

[172] Van Den Broeke, M. R., Enderlin, E. M., Howat, I. M., Kuipers Munneke, P., Noël, B. P. Y., Jan Van De Berg, W., Van Meijgaard, E. and Wouters, B.: On the recent contribution of the Greenland ice sheet to sea level change, The Cryosphere, 2016.

[173] Vedyushkin, M. A.: Fractal properties of forest spatial structure, Vegetatio, 113, 65-70, 1994.

[174] Wang, Z., Bovik, A. C., Sheikh, H. R. and Simoncelli, E. P., Image quality assessment: from error visibility to structural similarity, IEEE transactions on image processing, 13(4), 600-612, 2004.

[175] Webster, R., and Oliver, M. A.: Geostatistics for environmental scientists, John Wiley and Sons, 2007.

[176] Wiesmann, A. and Mätzler, C.: Microwave Emission Model of Layered Snowpacks, Remote Sensing of Environment, 70(3), 307–316, 1999.

[177] Ye, H., Yang, D., and Robinson, D.: Winter rain on snow and its association with air temperature in northern Eurasia, Hydrological Processes: An International Journal, 22(15), 2728-2736, 2008.

[178] Zampieri, M., Toreti, A., Schindler, A., Scoccimarro, E., and Gualdi, S.: Atlantic multi-decadal oscillation influence on weather regimes over Europe and the Mediterranean in spring and summer, Global and Planetary Change, 151, 92-100, 2017.

[179] Zwally, H. J. and Fiegles, S.: Extent and duration of Antarctic surface melting, Journal of Glaciology, 40(136), 463–475, 1994.

Appendix A

Chapter 2 supplementary material

		1000-1500	1500-2000	2000-2500	2500-3000	TOT
Oglio Chiese	**HS**	3036	4144	5007	2041	14228
	D	851	860	1710	1109	4530
Sarca Adda	**HS**	-	1633	1953	-	3586
	D	-	591	828	-	1419
Adige	**HS**	256	1869	1112	1297	4534
	D	97	471	90	901	1559
Toce	**HS**	442	2250	4025	-	6717
	D	-	236	708	-	944
Piave Brenta	**HS**	4307	3712	1266	-	9285
	D	1796	1565	842	-	4203
Serio Brembo	**HS**	200	4287	1361	-	5848
	D	-	728	677	-	1405

Table A.1: Number of snow depth and snow density measurements for each macro-basin and elevation classes.

Appendix B

Chapter 4 supplementary material

In this Supplementary material, we report the additional information we do not show in the manuscript for the sake of brevity. Specifically, we report the results of the commission/omission error analysis for all the available stations. We also report here additional figures related to the coarse resolution dataset analysis. For graphical reasons we assign an ID to the stations as follows:

Station	**ID**
Swiss Camp	01
Crowford Pt. 1	02
NASA-U	03
GITS	04
Humboldt	05
Summit	06
TUNU-N	07
DYE-2	08
JAR-1	09
Saddle	10
Southdome	11
NASA-E	12
Crowford Pt. 2	13
NASA-SE	14
KAR	15
JAR-2	16
KULU	17

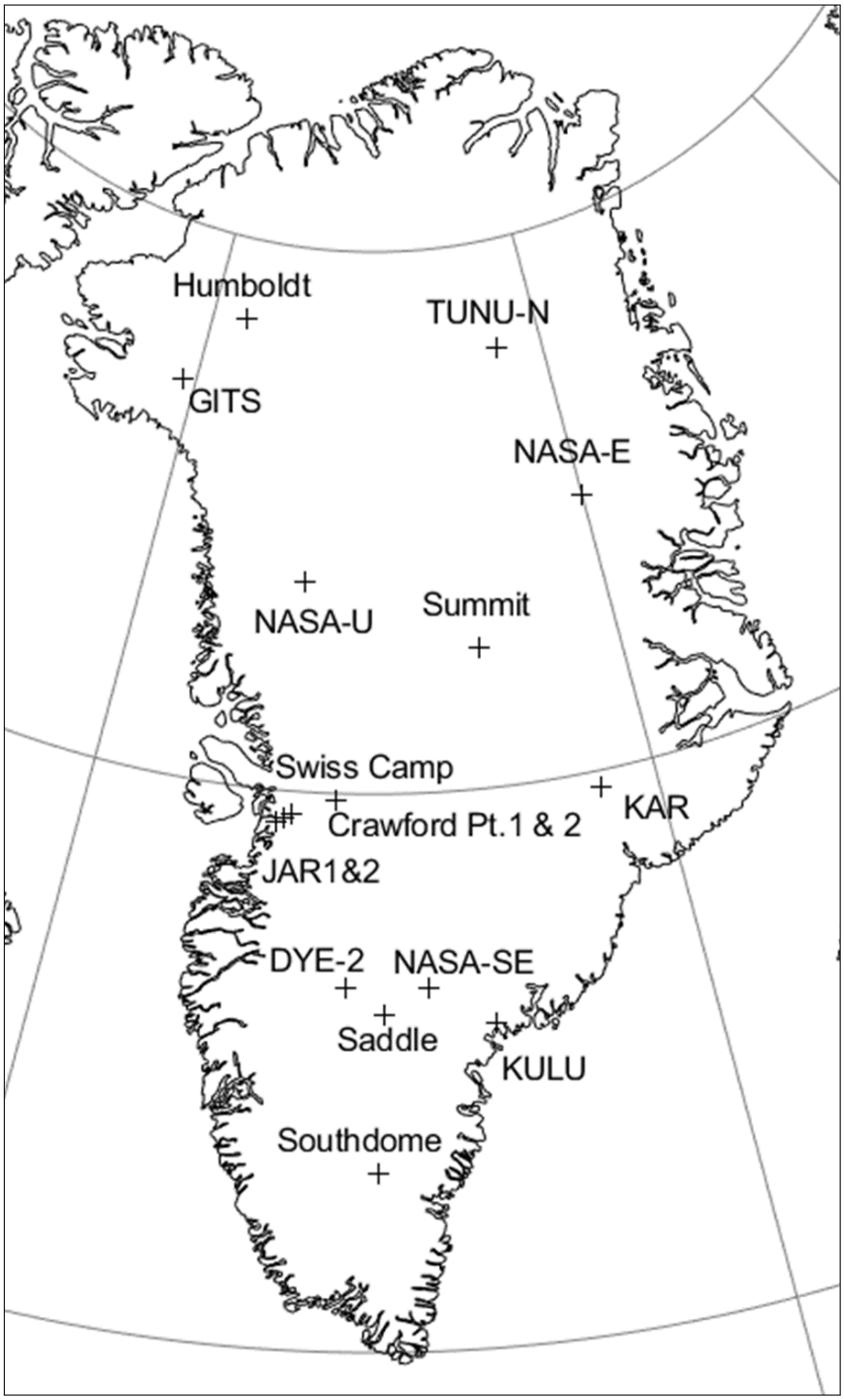

Figure B.1: Map of the automatic weather stations (AWS) of the Greenland Climate Network (GCNet) adopted for this study.

PMW	AWS/MAR	17	16	15	14	13	12	11	10	09	08	07	06	05	04	03	02	01
M+30	0°	0.39	7.03	1.15	2.5	1.36	1.17	2.79	5.57	3.93	8.97	3.81	1.21	5.63	2.94	5.33	6.12	3.2
M+30	-1°	0	6.66	0.76	2.06	0.19	1.14	2.46	4.8	2.8	6.67	3.54	1.21	4.96	2.57	4.91	4.57	2.42
M+30	-2°	0	5.11	0.38	1.42	0.19	1.09	2.11	3.91	2	5.04	3.15	1.19	4.43	2.1	4.4	3.27	1.71
M+30	MAR_{lm}	2.33	34.22	1.53	3.16	4.08	1.3	2.93	6.25	17.8	9.8	4.22	1.21	6.06	3.27	5.7	6.46	10.4
M+30	MAR_{Scm}	2.33	30.84	1.53	2.72	3.69	1.29	2.62	5.68	13.2	9.18	4.2	1.21	6.01	3.14	5.44	6.36	7.58
M+35	0°	0	3.56	0.76	1.88	0.78	0.4	1.82	4.03	2.96	7.74	1.37	0.19	2.71	1.5	2.87	4.48	2.71
M+35	-1°	0	3.28	0.38	1.58	0	0.38	1.64	3.41	2.01	5.54	1.3	0.19	2.32	1.3	2.59	3.2	2
M+35	-2°	0	2.28	0.19	1.06	0	0.35	1.37	2.59	1.32	4.03	1.07	0.19	1.99	1.02	2.3	2.14	1.34
M+35	MAR_{lm}	1.55	28.28	1.15	2.32	3.5	0.5	1.98	4.54	16.3	8.72	1.76	0.19	3.04	1.8	3.06	5.02	9.76
M+35	MAR_{Scm}	1.55	25.18	1.15	2.06	3.3	0.48	1.8	4.17	11.9	8.1	1.76	0.19	2.99	1.72	2.93	4.98	6.99
M+40	0°	0	1.82	0.38	1.58	0.78	0.3	1.38	3.11	2.16	6.85	0.64	0.11	1.44	0.75	1.74	3.9	2.51
M+40	-1°	0	1.73	0.19	1.34	0	0.28	1.24	2.61	1.34	4.78	0.57	0.11	1.18	0.63	1.58	2.75	1.82
M+40	-2°	0	0.91	0.19	0.93	0	0.27	0.98	1.92	0.84	3.38	0.43	0.11	0.98	0.52	1.37	1.77	1.21
M+40	MAR_{lm}	0.78	23.18	0.57	1.88	3.3	0.4	1.51	3.59	13.9	7.86	0.98	0.11	1.75	1	1.96	4.4	9.15
M+40	MAR_{Scm}	0.78	20.71	0.57	1.71	3.11	0.38	1.43	3.32	10.1	7.24	0.98	0.11	1.73	0.92	1.88	4.41	6.59
MEMLS	0°	0.78	10.77	0.95	3.48	1.17	0.25	3.12	3.65	4.48	6.65	0.46	0.11	0.7	0.83	1.42	4.14	3
MEMLS	-1°	0.39	10.13	0.57	2.98	0	0.23	2.83	3.06	3.3	4.71	0.41	0.11	0.53	0.68	1.26	2.87	2.21
MEMLS	-2°	0.39	8.3	0.38	2.09	0	0.22	2.51	2.35	2.48	3.33	0.3	0.11	0.39	0.52	1.06	1.84	1.47
MEMLS	MAR_{lm}	3.1	40.6	1.34	4.2	3.88	0.35	3.29	4.2	19.3	7.65	0.77	0.11	0.93	1.1	1.64	4.7	10.4
MEMLS	MAR_{Scm}	3.1	36.59	1.34	3.74	3.69	0.33	3.03	3.9	14.5	7.01	0.77	0.11	0.91	1.02	1.56	4.62	7.54
245K	0°	0	0.36	0	1.11	0.39	0	0.6	1.08	1.59	2.28	0.09	0.03	0.26	0.15	0.31	1.22	1.29
245K	-1°	0	0.36	0	0.87	0	0	0.53	0.93	1.06	1.58	0.09	0.03	0.19	0.13	0.26	0.85	0.87
245K	-2°	0	0.18	0	0.61	0	0	0.39	0.63	0.69	1.14	0.07	0.03	0.15	0.1	0.19	0.55	0.61
245K	MAR_{lm}	0.78	16.79	0	1.38	1.75	0	0.71	1.09	11.8	2.98	0.12	0.03	0.36	0.18	0.39	1.67	6.22
245K	MAR_{Scm}	0.78	14.51	0	1.24	1.75	0	0.66	1.08	8.39	2.66	0.12	0.03	0.36	0.15	0.35	1.72	4.15

Table B.1: Commission errors computed as percentage of the number of melting days detected by the specific algorithm (first column) with respect to 365 days for the 17 AWS (only days in which data are available from all the datasets have been considered).

PMW	AWS/MAR	17	16	15	14	13	12	11	10	09	08	07	06	05	04	03	02	01
M+30	**0°**	5.43	9.67	0.19	4.43	0.78	0.18	2.51	2.72	5.65	3.31	0.53	0.14	0.51	0.45	0.64	3.25	4.25
M+30	**-1°**	6.2	11.5	0.57	6.62	2.33	0.37	3.7	3.99	7.65	5.46	1.12	0.26	0.93	0.87	1.66	5.1	5.81
M+30	**-2°**	9.69	13.6	2.1	8.82	5.44	0.82	5.56	5.8	9.76	7.53	2.28	0.58	2.16	1.37	2.91	6.94	7.95
M+30	**MAR_{im}**	3.49	2.37	0.19	2.4	0.78	0.05	2.14	1.79	2.37	3.73	0.16	0	0.19	0.02	0.48	3.01	2.5
M+30	**MAR_{sm}**	3.49	4.47	0.38	3.45	2.91	0.12	2.72	2.95	3.06	4.17	0.27	0.08	0.31	0.12	0.71	3.06	2.85
M+35	**0°**	8.53	12.3	0.19	4.88	0.78	0.22	2.69	3.08	6.84	3.57	0.62	0.14	0.63	0.52	0.85	3.61	4.7
M+35	**-1°**	9.69	14.3	0.57	7.2	2.72	0.42	4.03	4.51	9.02	5.82	1.41	0.26	1.32	1.1	2.01	5.73	6.34
M+35	**-2°**	13.1	16.9	2.29	9.53	5.83	0.89	5.96	6.38	11.2	8.01	2.72	0.6	2.76	1.79	3.49	7.81	8.53
M+35	**MAR_{im}**	6.2	2.55	0.19	2.62	0.78	0.05	2.33	1.98	2.93	4.14	0.23	0	0.21	0.05	0.52	3.57	2.75
M+35	**MAR_{sm}**	6.2	4.93	0.38	3.85	3.11	0.12	3.04	3.33	3.93	4.58	0.36	0.08	0.33	0.2	0.87	3.67	3.2
M+40	**0°**	13.5	15.7	0.38	5.1	0.97	0.22	2.85	3.3	9.15	3.99	0.69	0.14	0.67	0.58	0.92	3.85	5.56
M+40	**-1°**	14.7	17.9	0.95	7.49	2.91	0.42	4.22	4.85	11.4	6.38	1.48	0.26	1.49	1.25	2.19	6.1	7.21
M+40	**-2°**	18.2	20.8	2.86	9.94	6.02	0.9	6.17	6.84	13.8	8.67	2.88	0.6	3.05	2.1	3.75	8.26	9.45
M+40	**MAR_{im}**	10.4	2.65	0.19	2.72	0.78	0.05	2.46	2.17	3.69	4.6	0.25	0	0.22	0.07	0.61	3.77	3.19
M+40	**MAR_{sm}**	10.4	5.66	0.38	4.03	3.11	0.12	3.27	3.62	5.19	5.04	0.37	0.08	0.38	0.22	1.01	3.93	3.85
MEMLS	**0°**	3.49	6.66	0.19	4.03	0.78	0.22	2.53	3.03	4.54	4.04	0.73	0.14	0.77	0.57	0.93	3.62	4.12
MEMLS	**-1°**	4.26	8.3	0.57	6.15	2.33	0.42	3.75	4.48	6.49	6.55	1.53	0.26	1.68	1.2	2.21	5.75	5.68
MEMLS	**-2°**	7.75	10.1	2.29	8.12	5.44	0.9	5.64	6.46	8.58	8.87	2.97	0.6	3.31	2	3.78	7.86	7.79
MEMLS	**MAR_{im}**	1.94	2.01	0.19	2.06	0.78	0.05	2.17	1.96	2.13	4.63	0.25	0	0.24	0.07	0.63	3.61	2.54
MEMLS	**MAR_{sm}**	1.94	3.47	0.38	3.08	3.11	0.12	2.8	3.38	2.71	5.05	0.37	0.08	0.39	0.22	1.03	3.67	2.88
245K	**0°**	13.5	21.7	0.57	5.28	2.14	0.32	3.04	4.4	12.2	7.57	1.01	0.14	0.98	0.85	1.08	5.72	10.7
245K	**-1°**	14.7	24	1.34	7.67	4.47	0.53	4.49	6.3	14.8	11.3	1.87	0.26	1.99	1.62	2.46	8.74	12.6
245K	**-2°**	18.2	27.4	3.24	10.2	7.57	1.04	6.55	8.68	17.4	14.5	3.4	0.6	3.72	2.55	4.17	11.5	15.2
245K	**MAR_{im}**	10.4	3.65	0.19	2.87	0.78	0.05	2.64	2.8	5.23	7.86	0.27	0	0.33	0.12	0.63	5.59	6.68
245K	**MAR_{sm}**	10.4	6.84	0.38	4.2	3.3	0.13	3.48	4.51	7.15	8.59	0.39	0.08	0.5	0.32	1.08	5.78	7.84

Table B.2: Omission errors computed as percentage of the number of melting days detected by the specific algorithm (first column) with respect to 365 days for the 17 AWS (only days in which data are available from all the datasets have been).

	Commission					Omission				
	0°	**-1°**	**-2°**	**MAR1m**	**MAR5cm**	**0°**	**-1°**	**-2°**	**MAR1m**	**MAR5cm**
01	2.21	1.54	0.95	8.53	6.28	6.76	8.53	10.53	3.83	4.25
02	2.19	1.39	0.84	3.07	2.95	5.64	8.51	11.33	5.94	5.96
03	0.97	0.86	0.72	1.2	1.12	0.99	2.34	3.85	0.65	0.97
04	0.53	0.42	0.32	0.72	0.63	0.44	0.91	1.56	0.02	0.13
05	0.53	0.42	0.25	0.65	0.65	0.82	1.64	3.24	0.19	0.32
06	0.08	0.08	0.08	0.08	0.08	0.17	0.29	0.67	0	0.11
07	0.4	0.36	0.27	0.69	0.69	0.88	1.66	3.12	0.29	0.44
08	4.25	2.8	1.73	5.16	4.74	5.66	8.68	11.35	6.42	7.1
09	6.06	4.86	4	20.05	15.98	6.63	8.65	10.68	2.7	3.28
10	2.08	1.66	1.18	2.38	2.27	3.24	4.95	6.89	2.82	4.36
11	0.74	0.63	0.46	0.8	0.8	3.07	4.25	6.23	2.76	3.6
12	0.23	0.23	0.21	0.34	0.34	0.27	0.48	1.01	0.06	0.17
13	0.58	0	0	2.72	2.52	1.36	3.5	6.6	0.78	3.11
14	0.91	0.72	0.46	1.07	0.97	0.91	0.72	0.46	1.07	0.97
15	0.57	0.38	0.19	0.76	0.76	0.38	0.95	2.67	0.19	0.38
16	7.3	6.93	5.75	31.93	28.65	13.23	15.15	17.61	3.38	5.57
17	0	0	0	0.39	0.39	18.6	19.77	23.26	15.12	15.12

Table B.3: Omission errors computed as percentage of the number of melting days of the Mote dataset (25 km) with respect to 365 days for the 17 AWS (first column, only days in which data are available from all the datasets have been).

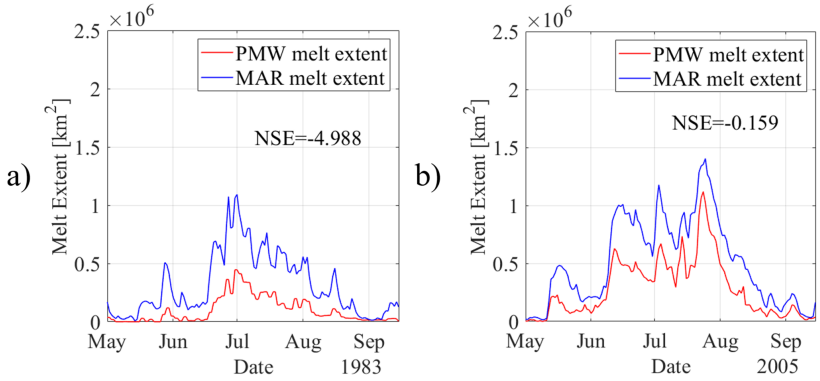

Figure B.2: Melt extent estimation from Mote (2014) dataset and the regional climate model MAR. Timeseries were obtained using LWC average in the first 5 cm of snowpack for the years (a) 1983 and (b) 2005.

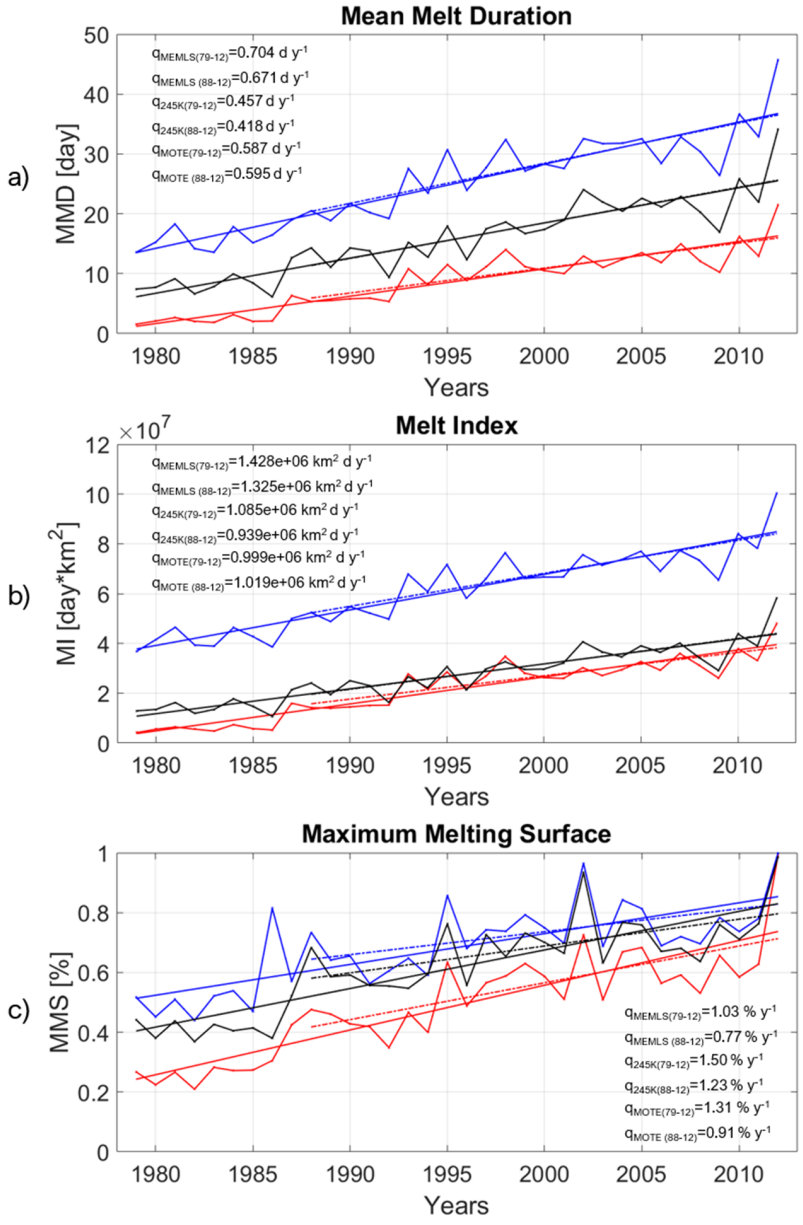

Figure B.3: Time series of annual a) mean melt duration (MMD), b) melt index (MI) and c) maximum melting surface (MMS) fraction. Regression lines computed for the periods 1979-2012 (solid line) and 1988-2012 (dashed-dot line). MMD is averaged over all the ice sheet pixels. Red lines refer to 245K, blue lines to MEMLS and black lines to the coarse resolution dataset.

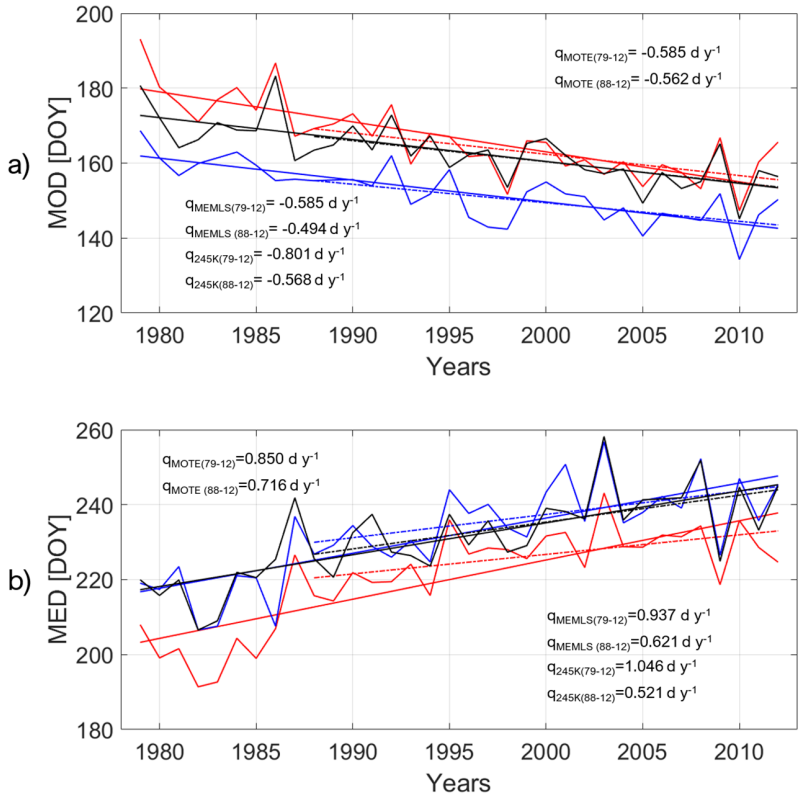

Figure B.4: Time series of annual a) mean melt onset date (MOD) and b) mean melt end date (MED). Regression lines computed for the periods 1979-2012 (solid line) and 1988-2012 (dashed-dot line). Red lines refer to 245K, blue lines to MEMLS and black lines to the coarse resolution dataset.

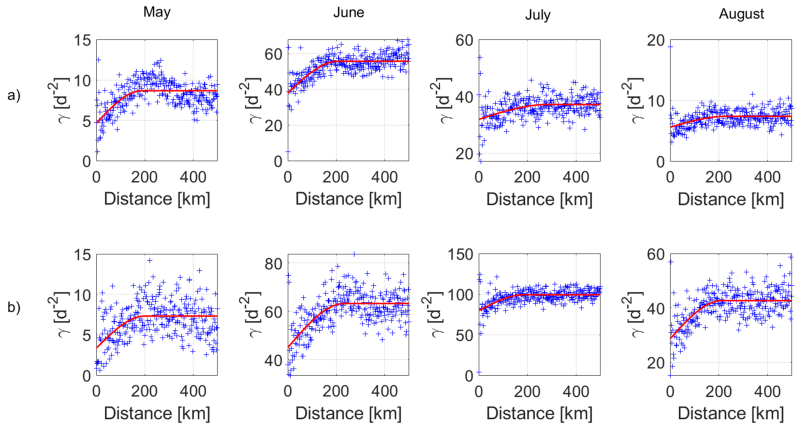

Figure B.5: Empirical (blue crosses) and modelled (red line) semi-variograms for Greenland melt duration (MD) computed from MAR_{5cm} (a) and MAR_{1m} (b). Table 7 reports range, sill, nugget and R^2 values of these semi variograms.